



UNIONE EUROPEA
Fondo Sociale Europeo



UNIVERSITÀ DEGLI STUDI DELL'AQUILA
DIPARTIMENTO DI SCIENZE FISICHE E CHIMICHE
Dottorato di ricerca in Scienze fisiche e chimiche
XXXIII ciclo

Sintesi, Funzionalizzazione e Caratterizzazione di Materiali Bidimensionali Avanzati

SSD FIS/01

Dottorando
Gianluca D'Olimpio

Coordinatore del corso

Antonio Mecozzi

Tutore

Luca Ottaviano

A.A. 2019/2020

Abstract

The discovery of graphene, with its unique properties, has inspired the quest for other two-dimensional (2D) materials. After considerable research efforts by the scientific community in the last 15 years, an extended atlas of 2D materials has been synthesized and investigated. Remarkably, materials beyond graphene could possess properties complementary to those of graphene, such as the presence of a direct band gap, more suitable for several applications, not limited to nano- and opto-electronics. Moreover, these materials have high potential for applications in biosensing technologies, catalysis, photocatalysis and energy storage. However, considering that most 2D materials have been newly discovered, the majority of the research efforts is focused on material synthesis and on the investigation of its electronic properties. Therefore, technological applications of 2D materials are still at the embryonic stage, also considering the difficulties in achieving large-scale and low-cost production for industrial use.

Among the various 2D materials, graphene-based derivatives and metal chalcogenides represent the most promising materials for technological applications.

Graphene oxide (GO) has attracted particular attention from the industrial world, since it represents a low-cost precursor of graphene for large-scale production. GO offers tremendous opportunities for the access to functionalized graphene-based materials. More specifically, both GO and reduced GO (rGO) can be processed into a wide variety of novel materials with distinctly different morphological features, where the carbonaceous nanosheets can serve as either the sole component, as in papers and thin films, or as fillers in polymer and/or inorganic nanocomposites. In addition, GO and rGO enable efficient electro-optical, filtering and nano-biotechnological applications, as well as gas sensing devices, polymeric nanocomposites and gas barriers.

On the other hand, transition-metal dichalcogenides (TMDs) belonging to the class of MTe_2 ($M = Ni, Pd$) are particularly relevant for both fundamental and technological interest, owing to the presence of a tilted Dirac cone formed by bulk states, which implies high-mobility charge carriers. Being the Dirac cone located in the bulk, it naturally exhibits superior robustness to surface modifications compared to other Dirac materials, i.e. graphene, topological insulators and silicene. Consequently, MTe_2 displays intriguing application capabilities in

optoelectronics and catalysis, in consideration of its nature as type-II Dirac semimetal.

In addition, among the broad class of layered metal chalcogenides, van der Waals semiconductors are particularly suitable for optoelectronic and sensing devices. Especially, recent experiments on exfoliated GaSe nanosheets reported an enhancement of performance in electrochemistry and photocatalysis opening a new way for its applications in the fields of energy and catalysis. In addition, SnSe₂ represent another interesting van der Waals semiconductor with ultralow thermal conductivity.

In this thesis, issues related to technology transfer of 2D materials beyond graphene were addressed. More specifically, a solution for the reduction of costs in the state-of-the-art production of GO was identified. Moreover, a sustainable eco-friendly solvent was demonstrated to be able to replace toxic solvents in the large-scale production of functional inks based on 2D materials, solving one of the most relevant problems for the 2D materials-based industry. In particular, the use of Polarclean as eco-friendly solvent for liquid-phase exfoliation of 2D materials also enables the introduction of 2D materials in unexplored fields, such as agri-food and desalination industries, which are expected to take advantage of the unusual properties of 2D materials in terms of both efficiency and selectivity.

Furthermore, newly discovered 2D materials belonging to the class of metal chalcogenides (PdTe₂, NiTe₂, GaSe, SnSe₂) were introduced in the industrial world, by engineering prototypes of catalytic devices, gas sensors and IR/THz imaging systems based on these innovative materials, with competitive performances with the state-of-the-art systems since their first implementation.

Preface

In this thesis the main results of my research activity performed during the PhD are reported. The main subjects of my studies during these three years have been graphene oxide (GO), transition-metal dichalcogenides (TMDs) NiTe₂ and PdTe₂, and the layered semiconductors GaSe and SnSe₂.

The study of physicochemical properties of these materials and the fabrication of different devices have resulted in the publication of several papers and the participation to different conferences.

This PhD work has developed through scientific collaboration with various research groups worldwide. Especially, this research program has led to a formal collaboration with Hygraner s.r.l., an Italian start-up devoted to the large-scale production of graphene and graphene oxide, and prof. Tomasz Klimczuk from Gdansk University of Technology (Poland), with signed agreements with University of L'Aquila. Other collaborators were the staff of APE, BACH and Nanospectroscopy beamlines at Elettra Sincrotrone Trieste; prof. Danil Boukhvalov from Ural Federal University (Russia); prof. Chin Shan Lue from National Cheng Kung University (Taiwan) and prof. Carlo Cantalini from Department of Chemical Engineering of the University of L'Aquila.

Considering the involvement of different coauthors in scientific publications, here I briefly indicate my contribution in the papers discussed in the following sections of this thesis.

In Chapter I, studies on morphological and chemical characterizations on different graphene oxide (GO) and reduced graphene oxide (rGO) produced by Hygraner srl. are reported. Moreover, an eco-friendly solvent for liquid-phase exfoliation of 2D materials is reported. This last part was published in 'Sustainable liquid-phase exfoliation of layered materials with non-toxic Polarclean solvent' (V. Paolucci, G. D'Olimpio, et al., **ACS Sustainable Chemistry & Engineering**, 2020).

Chapter II has been published in: 'Transition-metal dichalcogenides with type-II Dirac fermions: Surface properties and application capabilities' (G. D'Olimpio, **Riv. del Nuovo Cim. C**, 2020, Vol. 43, Issue 4-5, 113); 'PdTe₂ Transition-Metal Dichalcogenide: Chemical Reactivity, Thermal Stability, and

Device Implementation' (G. D'Olimpio et al, **Adv. Funct. Mater.** 2020, 30, 1906556); 'Transition-Metal Dichalcogenide NiTe₂: An Ambient-Stable Material for Catalysis and Nanoelectronics' (S. Nappini, D. W. Boukhvalov, G. D'Olimpio, et al., **Adv. Funct. Mater.** 2020, 2000915). In these works, I have prepared and characterized the samples by XPS, Raman and AFM techniques, to study the surface chemical properties and the ambient stability of the materials for a successively device implementation.

Chapter III has been published in: 'Charge Redistribution Mechanisms in SnSe₂ Surfaces Exposed to Oxidative and Humid Environments and Their Related Influence on Chemical Sensing' (G. D'Olimpio, et al., **J. Phys. Chem. Lett.** 2020, 11, 9003-11); 'Enhanced Electrocatalytic Activity in GaSe and InSe Nanosheets: The Role of Surface Oxides' (G. D'Olimpio, et al., **Adv. Funct. Mater.** 2020, 2005466). In these works, I have prepared and characterized the samples by XPS, LEEM and EELS spectroscopies. For the SnSe₂ I have studied the charge redistribution at the SnO₂-SnSe₂ heterojunction in both oxidative and humid environments. In the case of GaSe I have studied the enhancement of the performance in electrochemistry after exfoliation.

During the PhD Program several papers were published as follows:

1. **G. D'Olimpio**, et al. *Charge Redistribution Mechanisms in SnSe₂ Surfaces Exposed to Oxidative and Humid Environments and Their Related Influence on Chemical Sensing*, *J. Phys. Chem. Lett.* **2020**, 11, 9003-11.
2. **G. D'Olimpio**, *Transition-metal dichalcogenides with type-II Dirac fermions: Surface properties and application capabilities*, *Riv. del Nuovo Cim. C*, **2020**, Vol. 43, Issue 4-5, 113.
3. **G. D'Olimpio**, et al., *Enhanced Electrocatalytic Activity in GaSe and InSe Nanosheets: The Role of Surface Oxides*, *Adv. Funct. Mater.* **2020**, 2005466.
4. **G. D'Olimpio**, et al., *PdTe₂ Transition-Metal Dichalcogenide: Chemical Reactivity, Thermal Stability, and Device Implementation*, *Adv. Funct. Mater.* **2020**, 30, 1906556.

5. **G. D'Olimpio** et al., *Catalytic activity of PtSn₄: Insights from surface-science spectroscopies*, *Appl. Surf. Sci.* **2020**, 145925.
6. **G. D'Olimpio**, *La Fabbrica dei Materiali di Dirac*, SIF Prima Pagina **2020** January, N.73, url: <https://www.primapagina.sif.it/article/1064/la-fabbrica-dei-materiali-di-dirac#.X2tm8oupWDQ>.
7. V. Paolucci, **G. D'Olimpio**, et al. *Sustainable Liquid-Phase Exfoliation of Layered Materials with Nontoxic Polarclean Solvent*. *ACS Sustainable Chemistry & Engineering*. **2020**, <https://doi.org/10.1021/acssuschemeng.0c04191>.
8. S. Nappini, D. W. Boukhvalov, **G. D'Olimpio**, L. Zhang, B. Ghosh, C. N. Kuo, H. Zhu, J. Cheng, M. Nardone, L. Ottaviano, *Transition-Metal Dichalcogenide NiTe₂: An Ambient-Stable Material for Catalysis and Nanoelectronics*, *Adv. Funct. Mater.* **2020**, 2000915.
9. D. W. Boukhvalov, V. Paolucci, **G. D'Olimpio**, C. Cantalini, A. Politano, *Chemical reactions on surfaces for applications in catalysis, gas sensing, adsorption-assisted desalination and Li-ion batteries: opportunities and challenges for surface science*, *Physical Chemistry Chemical Physics* **2020**.
10. V. Paolucci, **G. D'Olimpio**, C.-N. Kuo, C. S. Lue, D. W. Boukhvalov, C. Cantalini, A. Politano, *Self-Assembled SnO₂/SnSe₂ Heterostructures: A Suitable Platform for Ultrasensitive NO₂ and H₂ Sensing*, *ACS Appl. Mater. Interfaces* **2020**, 12, 34362.
11. D. W. Boukhvalov, A. Marchionni, J. Filippi, C.-N. Kuo, J. Fujii, R. Edla, S. Nappini, **G. D'Olimpio**, L. Ottaviano, C. S. Lue, *Efficient hydrogen evolution reaction with platinum stannide PtSn₄ via surface oxidation*, *J. Mater. Chem. A* **2020**, 8, 2349.
12. S. Palleschi, **G. D'Olimpio**, P. Benassi, M. Nardone, R. Alfonsetti, G. Moccia, M. Renzelli, O. Cacioppo, A. Hichri, S. Jaziri, *On the role of nano-confined water at the 2D/SiO₂ interface in layer number engineering of exfoliated MoS₂ via thermal annealing*, *2D Materials* **2020**, 7, 025001.

13. D. Mastrippolito, S. Palleschi, **G. D'Olimpio**, A. Politano, M. Nardone, P. Benassi, L. Ottaviano, *Exciton–phonon coupling and power dependent room temperature photoluminescence of sulphur vacancy doped MoS₂ via controlled thermal annealing*, *Nanoscale* **2020**.
14. C. Guo, W. long Guo, H. Xu, L. Zhang, C. Gang, **G. D'Olimpio**, C. Kuo, C. Lue, A. Politano, L. Wang, *Ultrasensitive Ambient-Stable SnSe₂-based Broadband Photodetectors for Room-Temperature IR/THz Energy conversion and Imaging*, *2D Materials* **2020**.
15. S. Kazim, M. Ali, S. Palleschi, **G. D'Olimpio**, D. Mastrippolito, A. Politano, R. Gunnella, A. Di Cicco, M. Renzelli, G. Moccia, *Mechanical exfoliation and layer number identification of single crystal monoclinic CrCl₃*, *Nanotechnology* **2020**.
16. L. Ottaviano, S. Palleschi, F. Perrozzi, **G. D'Olimpio**, F. Priante, M. Donarelli, P. Benassi, M. Nardone, M. Gonchigsuren, M. Gombosuren, *Mechanical exfoliation and layer number identification of MoS₂ revisited*, *2D Materials* **2017**, 4, 045013.

Attendance at conferences:

- 105° Congresso Nazionale della Società Italiana di Fisica 23 al 27 september 2019, L'Aquila: **G. D'Olimpio**, L. Ottaviano, D. Boukhvalov, M. Nardone, S. Nappini, F. Bondino, A. Agarwal, and A. Politano “*Transition-metal dichalcogenide NiTe₂: an ambient-stable material for catalysis and nanoelectronics*” - ORAL CONTRIBUTION
- 106° Congresso Nazionale della Società Italiana di Fisica 14 al 18 september 2020, Milano: **G. D'Olimpio**, S. Nappini, L. Lozzi, F. Genuzio, T. O. Menteş, V. Paolucci, A. Locatelli, F. Bondino, D. W. Boukhvalov, L. Ottaviano, and A. Politano “*The beneficial impact of surface oxidation on electrochemical reactions with GaSe nanosheets*” - ORAL CONTRIBUTION

Attendance at PhD Schools:

- *XV School on Synchrotron Radiation: Fundamentals, Methods and Applications*,

The School give a general overview of the characteristics and potentiality of synchrotron radiation. Muggia (TS) 16-27 september 2019

Others activity:

- Principal Investigator of proposal n.20190107 at Elettra Sincrotrone Trieste, title: *Oxidation mechanism, stability and chemical reactivity of InSe, GaSe and GaTe van der Waals semiconductors*
- Principal Investigator of proposal n.20195050 at Elettra Sincrotrone Trieste, title: *Surface chemical reactivity of niobium arsenides NbAs and NbAs₂*
- Principal Investigator of proposal n.20200219 Elettra Sincrotrone Trieste, title: *Selective methanol to syngas decomposition catalyzed by Ni-Sn compounds: reaction mechanism investigation by means of operando NEXAFS spectroscopy*
- Participant at the beamtime n.20190079 at Elettra Sincrotrone Trieste, title: *Surface catalysis with NiTe₂ transition-metal dichalcogenide*
- Participant at the beamtime n.20190080 at Elettra Sincrotrone Trieste, title: *Surface chemical reactions at PtSn₄ surface*
- Participant at the proposal n.20192010 submitted to CERIC-ERIC, title: *Near-ambient pressure XPS on water intercalation in graphene/Ni(111)*
- Participant at beamtime n.20195108 at Elettra Sincrotrone Trieste, title: *Surface chemical reactivity of SnSe₂: chemisorption, air stability and gas sensing*
- Participant at the proposal n.20197085 submitted to CERIC-ERIC, title: *Oxidation of tin diselenide: a combined NAP-XPS and LEEM/XPEEM investigation*

Awards:

- Best presentation at 105° Congresso Nazionale della Società Italiana di

Fisica 23-27 september 2019.

- “Best communication” at 106° Congresso Nazionale della Società Italiana di Fisica 14-18 september 2020

Contents

Abstract.....	i
Preface.....	iii
Contents	ix
1 Graphene Oxide.....	1
Introduction.....	1
Methods.....	2
Results and discussion	3
Morphological analysis	3
Spectroscopic analysis as a function of GO reduction degree.....	6
Polarclean: an eco-friendly solvent for liquid-phase exfoliation	9
Conclusions	13
2 Transition metal dichalcogenides: NiTe ₂ and PdTe ₂	17
Introduction.....	17
Methods.....	19
Results and discussion	21
Conclusions	37
3 GaSe and SnSe ₂ : layered semiconductors	43
GaSe a layered semiconductor for catalysis	44
Introduction	44
Methods.....	46
Results and discussion	47
Conclusions.....	62
SnSe ₂ a layered semiconductor for sensing.....	63
Introduction	63
Methods.....	64

Results and discussion	65
Conclusions.....	73
4 Conclusion.....	82
Appendix.....	84
A. Calculation of the density of defects	84
B. X-Ray Diffraction (XRD)	85
C. Calculation of phonon modes	85
D. Survey XPS spectrum of the as-cleaved samples of NiTe ₂ and PdTe ₂ 87	
E. Determination of the thickness of the oxide skin.....	87
F. Survey XPS spectrum of the as-cleaved samples of GaSe and InSe ..	89
G. Survey XPS spectrum of the as-cleaved sample of SnSe ₂	90

Graphene Oxide

Introduction

Nowadays, graphene oxide (GO) and graphene have moved towards large-scale industrial production. Formerly, GO was thought as a precursor of industrial produced graphene ^[1], while now GO itself represents the final production. As a matter of fact, GO displays peculiarities with high technological potential, such as tuneable optoelectronic properties ^[2], mechanical strength ^[3], high solubility ^[4] and photocatalytic properties ^[5, 6]. Moreover, both GO and reduced GO (rGO) find applications in electro-optical ^[7-9], gas sensing devices ^[10, 11] and gas barriers ^[12], drug delivery ^[13], photocatalysis ^[14], supercapacitors ^[15] and as composite material for anti-corrosion application ^[16].

Basically, GO is a two-dimensional graphene-based system showing functional groups with carboxyl (OH), carboxylic (O=C-OH) and carbonyl (O=C) groups and with high abundancy (~5% of surface area) of defects sites. Clearly, the concentration of defects, as well as the ratio of functionalized groups, are strongly related to the production method of GO and the related post-exfoliation process.

In this chapter, the characterization of industrially produced GO and rGO is reported. Moreover, the identification of an eco-friendly and non-toxic solvent (e.g., Polarclean) for liquid-phase exfoliation of layered materials is described. Experimental tools were SEM, AFM, Raman, UV-VIS and XPS techniques.

Methods

Synthesis of graphene oxide. Graphene oxide was prepared by a modified Hummers method^[17]. The lateral size of the graphene oxide sheets was tuned by jet mill fragmentation process.

SEM. Scanning electron microscopy (SEM) was performed using a Zeiss Gemini500SEM system. The flake area has been determined with the best possible accuracy with a pixel counting procedure. The corresponding flakes size has been determined as:

$$size = \sqrt{\frac{4 \cdot flake\ area}{\pi}}$$

XPS. XPS was carried out with a PHI 1257 spectrometer equipped with a monochromatic Al K α source (h ν =1486.6 eV). The different GO solutions were spin coated on 100 nm Au(100)/Si(111) substrate in order to perform XPS analysis. The acquired XPS spectra were fitted with Voigt line shapes and Shirley backgrounds.

AFM. AFM images were acquired in air in tapping mode using a Veeco Digital D5000 system. The microscope was equipped with silicon tips with spring constant of 3 N/m and resonance frequencies between 51 and 94 kHz.

STEM. STEM investigation was performed with a JEOL ARM200F Cs-corrected microscope, equipped with a cold-field emission gun with an energy spread of 0.3 eV and operating at 60 keV. The probe size was 1.1 Å at 60 kV. Micrographs were acquired in BF and in Z-contrast mode by HAADF.

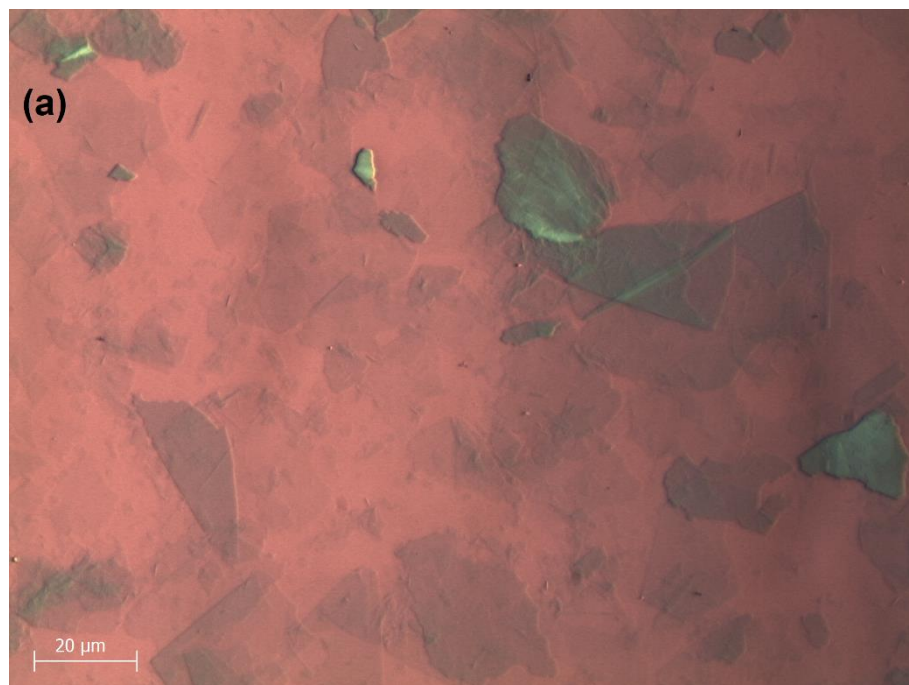
UV-Vis. Optical absorption spectra of graphene were measured by using a UV-Vis spectrometer (Perkin Elmer, Lambda 750) with a 1 cm quartz cuvette.

Results and discussion

Morphological analysis

In this section it is showed a morphological analysis of the different industrial produced GO flakes.

In order to tune the flake size, the GO solution has been processed at different time intervals. Atomic force microscopy and X-ray spectroscopy analysis were performed to have a complete picture on the effect of the jet mill on the GO.



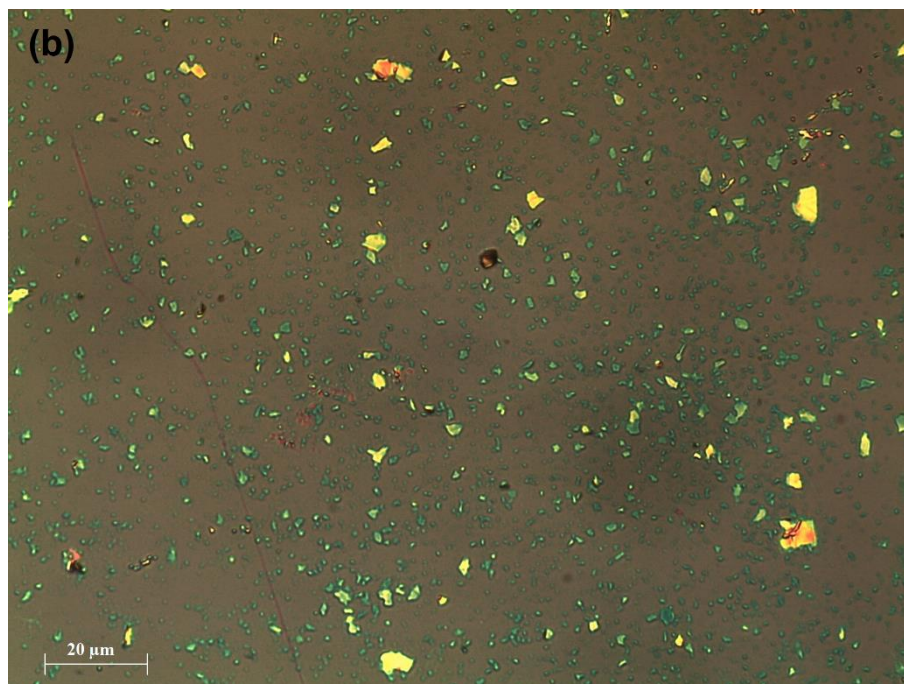


Figure 1.1: Optical microscope, (a) GO with a lateral size distribution of $10\ \mu\text{m}$, after 10 minutes of exfoliation process. (b) GO with a lateral size distribution of $0.4\ \mu\text{m}$, after 30 minutes of exfoliation process.

Optical analysis revealed that the fragmentation of the starting material for different times clearly reduce the dimension of the graphitic planes (Figure 1.1). The lateral size distribution was then obtained by performing a statistical analysis of several optical images. The flake size distributions of the two GO samples were fitted by a log-normal model, which typically occurs in random fragmentation phenomena. The solution of 10mins-GO contained large flakes with an average lateral size of about $6\ \mu\text{m}$, while the sample 30mins-GO

contained GO planes with dimensions around $0.3 \mu\text{m}$.

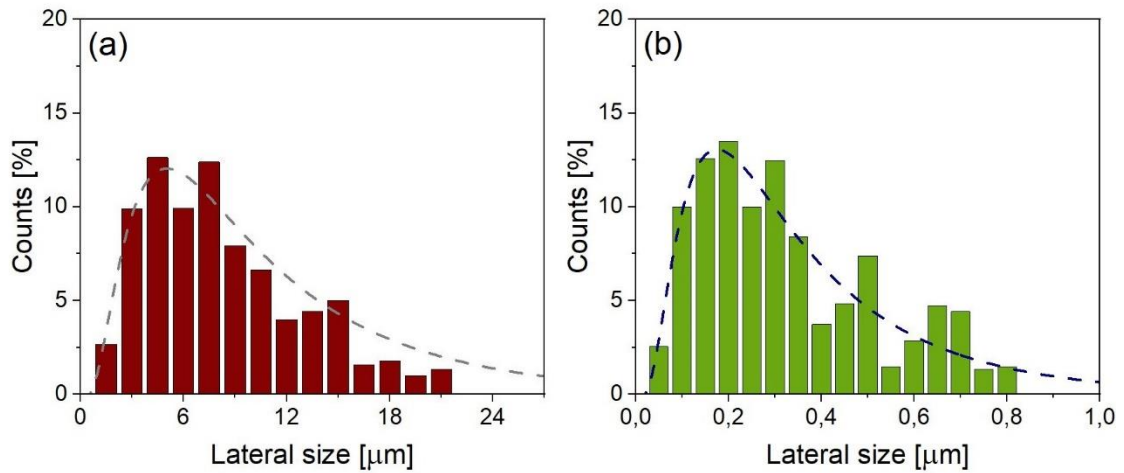


Figure 1.2: (a) and (b) analysis of lateral size distribution of GO flakes exfoliated for 10 and 30 minutes, respectively.

AFM images are reported in Figure 1.3 showing a homogenous dispersion of GO sheets.

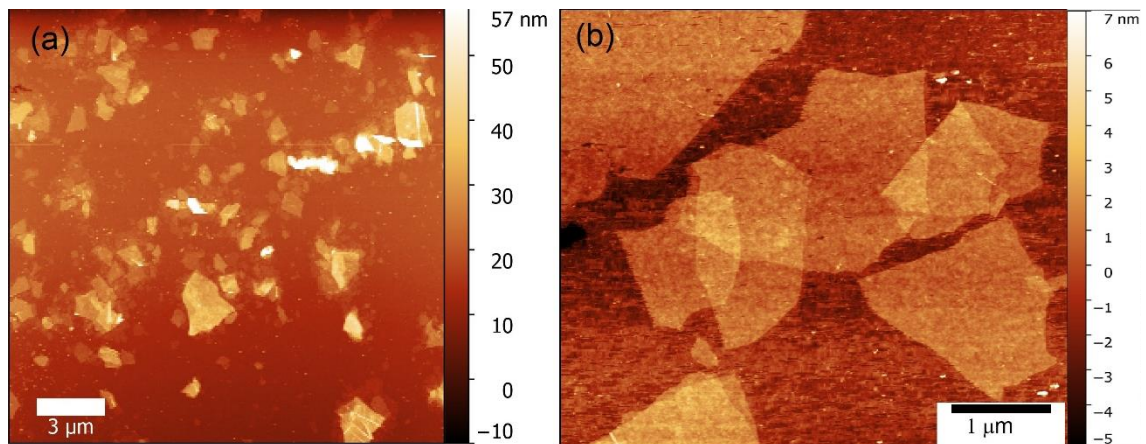


Figure 1.3: AFM images of exfoliated GO. (a) 10 minutes (b) 30 minutes of exfoliation process.

In Figure 1.3 it is shown the different thickness of GO flakes in function of the exfoliation time process. After 10 minutes of exfoliation the average height distribution is 4 nm, while for the 30mins-GO is 1.5 nm.

The type and the level of oxygenated species on the two different GO samples were assessed by XPS analysis. In this section the XPS analysis is briefly reported to see if the sonication induces chemical changing on GO. The XPS C 1s core level

spectra are displayed in Figure 1.4.

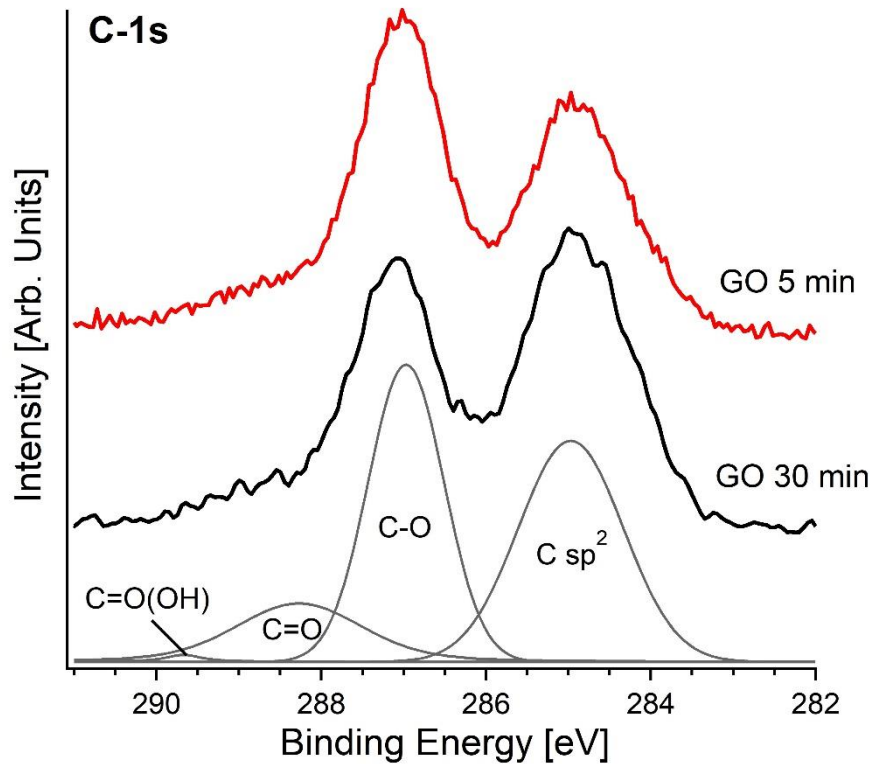


Figure 1.4: C 1s XPS core level spectra of different GO solutions. The fitting analysis reports the various components in the spectra assigned to different typical functional groups of GO.

The spectra were deconvoluted in four components. At the BE of 284.7 eV we have the aromatic rings and hydrogenated carbon (C=C/C-C, C-H), at 286.9 eV the epoxy groups (C-O-C), at 288.2 eV carbonyl groups (C=O) and at 289.3 eV carboxyl groups (C=O(OH)) [18]. After a quantitative analysis of the above-mentioned components for the different spectra, no substantial variations were found. The spectral weight of the different components was: C=C/C-C 47%, C-O-C 37%, C=O 15%, and C=O(OH) 1%.

Spectroscopic analysis as a function of GO reduction degree

In this section it is reported a systematic XPS investigation of GO as a function of its reduction degree. GO is reduced by thermal annealing in furnace. This reduction method is advantageous since it does not introduce extrinsic chemical

modification in the system under analysis.

Figure 1.5 reports the C 1s X-ray photoemission core level spectra measured on GO/Au(100) as a function of the annealing temperature. The resulting quantitative estimate of the C/O ratio is reported in the inset of Figure 1.6 (full circles). This value monotonically rises from 2.0 (pristine GO) to 8.0 (GO annealed at 670 °C). This is a clear indication of GO reduction under thermal treatment [19, 20].

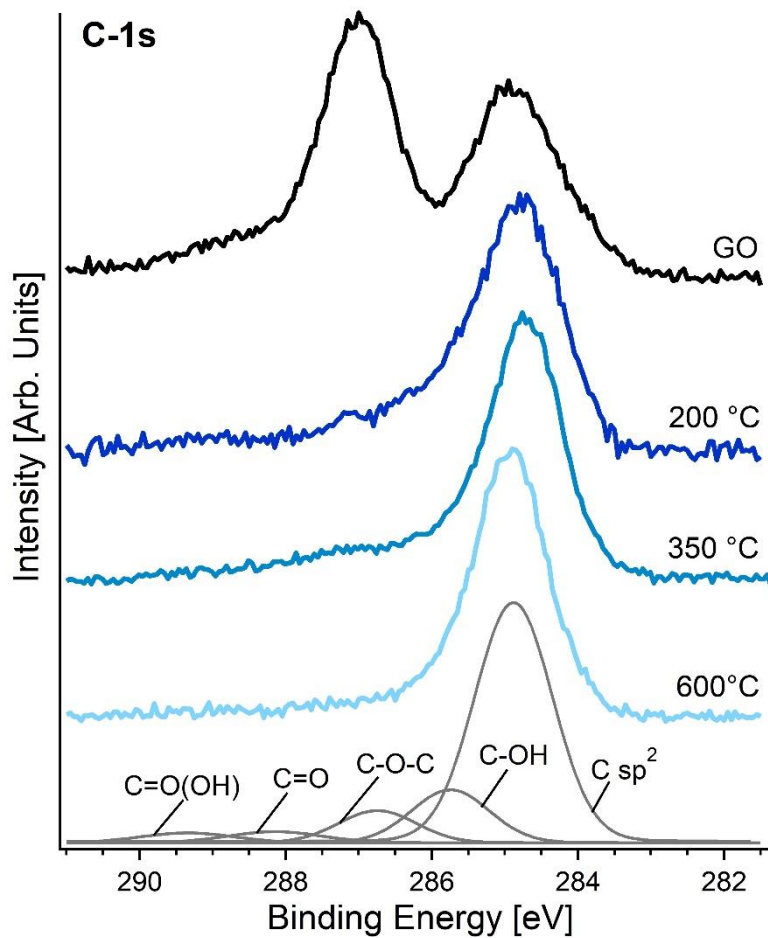


Figure 1.5: Core level C-1s XPS spectra of GO/Au(100) as a function of the annealing temperature. C-1s spectra are fitted by the sum of five components: C=C/C-C (C-H) (284.6-284.9 eV), C-OH (285.9 eV), C-O-C (286.9 eV), C=O (288.2 eV), C=O(OH) (289.3 eV), and the π - π^* shake-up component (290.6 eV).

A lot of information can be reached from a detailed analysis of the C 1s core level spectra. The C 1s spectra are all fitted by five components assigned to: aromatic rings and hydrogenated carbon (C=C/C-C, C-H) at the BE = 284.6-284.9

eV, hydroxyl groups (C-OH) at BE = 285.9 eV, epoxy groups (C-O-C) at BE = 286.9 eV, carbonyl groups (C=O) at BE = 288.2 eV, and carboxyl groups (C=O(OH)) at BE = 289.3 eV [1, 18, 21].

The relative abundances of each component of the C 1s spectra are summarized in the graph of Figure 1.6 as a function of the annealing temperature.

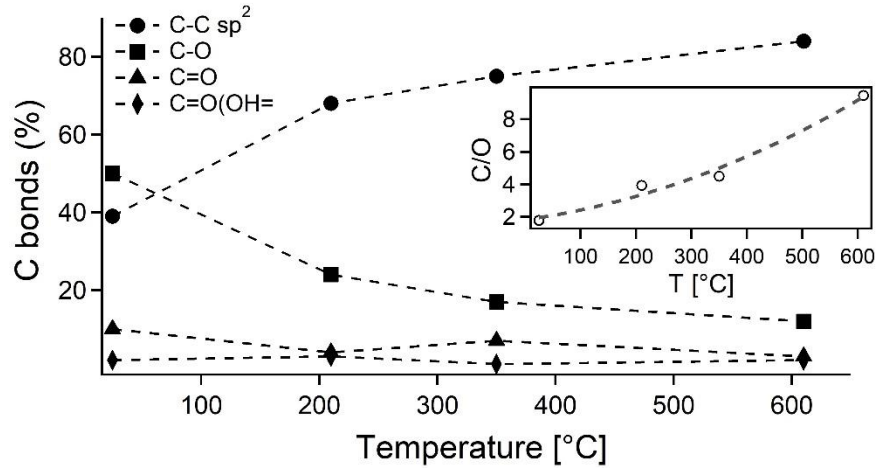


Figure 1.6: Relative weights of the C 1s spectral components as a function of the annealing temperature.

The abundance curves show that, as a consequence of thermal annealing, all the groups containing oxygen tend to disappear, unlike those containing carbon only, indicating a loss of oxygen in favor of sp^2 carbon domains formation (the sp^2 carbon content of 39% in pristine GO increases up to 84% at 600 °C annealing temperature). The data are in agreement with those reported in Ref. [19]. In particular, the sp^2 carbon content approaches 80% at about 350 °C.

All these evidences point to the same conclusion that a thermal annealing above 350 °C is not effective in improving the crystalline quality of the graphene patches in GO. Above the temperature of 350 °C the oxygen desorption is clearly accompanied by the introduction of topological defects. Note that all the C atoms in such defects exhibit local sp^2 hybridization and, accordingly, the XPS analysis exhibits a monotonic increase of the sp^2 content as a function of the thermal annealing (see Figure 1.6). In summary the GO thermal reduction is efficient up to moderate temperatures (350 °C) but beyond these temperatures the process starts to backfire.

Polarclean: an eco-friendly solvent for liquid-phase exfoliation

Liquid-phase exfoliation (LPE) ^[22-26] offers high-quality dispersions of 2D materials exfoliated from their bulk counterparts and dispersed in solvents enabling further processing ^[22-26]. Definitely, a suitable solvent for LPE should minimize the energy input required to overcome the van der Waals forces for effective sheets separation ^[23-26]. For the specific cases of graphene and transition-metal dichalcogenides, NMP and, N,N-Dimethylformamide (DMF) are the most diffusely used solvents ^[22]. Nevertheless, recently, both NMP and DMF have been placed on the list of Substances of Very High Concern (SVHC) ^[27], which is the first step for introducing restrictions over the use of substances or their import to Europe, according to the European REACH regulation ^[28]. In particular, NMP has been already classified as a reproductive toxin ^[29], mainly owing to its amide functionalities.

Therefore, it is becoming mandatory to search for a *green* alternative to these traditional aprotic solvents.

We assess the performance of methyl-5-(dimethylamino)-2-methyl-5-oxopentanoate (Rhodiasolv® Polarclean, CAS: 1174627-68-9) as a polar solvent ^[30] for sonication-assisted LPE of layered materials. Polarclean (C₉H₁₇NO₃) has no detectable toxicity for doses as high as 1000 mg/kg/day; its water solubility is higher than 490 g/l at T=24°C; and it is biodegradable and not mutagenic ^[31]. Only CO₂ is released upon combustion or thermal decomposition ^[31].

Currently, Polarclean is mostly used for solubilization of agrochemicals, as well as for crop protection and animal nutrition ^[32]. Recently, the use of Polarclean has been extended to the production of polymeric membranes for ultrafiltration ^[33], the synthesis of bio-based aliphatic polyurethanes ^[34], dimerization of abietic acid ^[35], and for copper-catalyzed azide–alkyne cycloaddition ^[36]. Its dynamical viscosity (9.78 cP at T=23°C ^[31]) makes Polarclean an ideal candidate for ink-jet printing of 2D materials-based devices, for which the low dynamical viscosity of state-of-the-art solvents DMF and NMP (<2 cPa) jeopardizes the jetting performance ^[37].

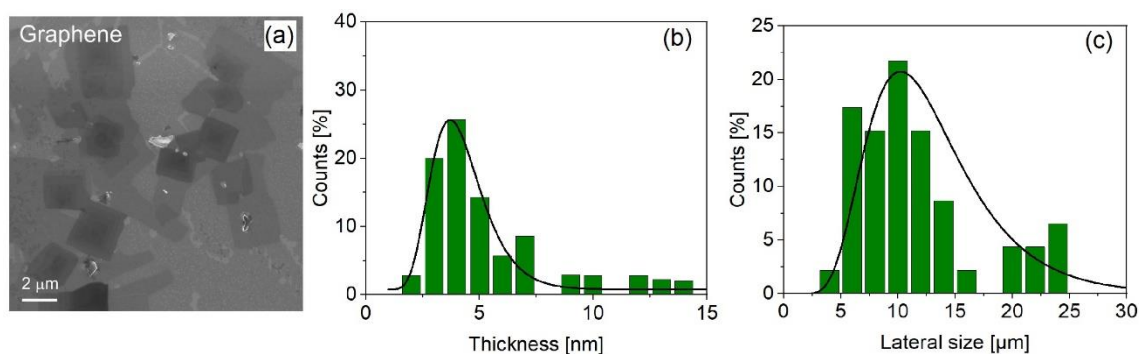


Figure 1.7: (a) Representative SEM image of isolated exfoliated flakes of graphene. (b) and (c) statistical analysis of lateral size and thickness of graphene flakes.

Concerning the exfoliation of graphene nanosheets with Polarclean, the distribution of lateral size reaches an average value of 10 μm (Figure 1.7), which is one of the largest reported so far for LPE of graphite [12,19]. The corresponding Raman spectrum (Figure 1.8) displays D and G bands at 1331 and 1581 cm⁻¹. We remind that, while the G peak arises from E_{2g} optical phonon of graphene [38], the D band is originated by breathing modes of six-atom rings and requires a defect for its activation [39]. Therefore, the I(D)/I(G) ratio is a widely recognized probe of structural defects in the graphene sheet [40]. Notably, the ratio of the intensity of D and G Raman-active bands in few-layers graphene exfoliated through Polarclean is I(D)/I(G) = 0.07 ± 0.01.

Definitely, we estimate a density of defects as low as $(8 \pm 2) \cdot 10^9$ cm⁻² (see Appendix A for detailed calculation), which is consistent with the high crystalline order of exfoliated graphene flakes (without evidence of defects) imaged by HR-TEM in Figure 1.9. For the sake of comparison, from the I(D)/I(G) analysis in Raman spectra (Figure 1.8), we also estimated the density of defects for graphene exfoliated with NMP [41, 42] and Cyrene [42], solvents, finding values of $(6 \pm 2) \cdot 10^{10}$ and $(5 \pm 2) \cdot 10^{10}$ defects·cm⁻², respectively. Evidently, graphene flakes exfoliated with Polarclean exhibit a density of defects inferior by approximately one order of magnitude with respect to LPE assisted by other solvents.

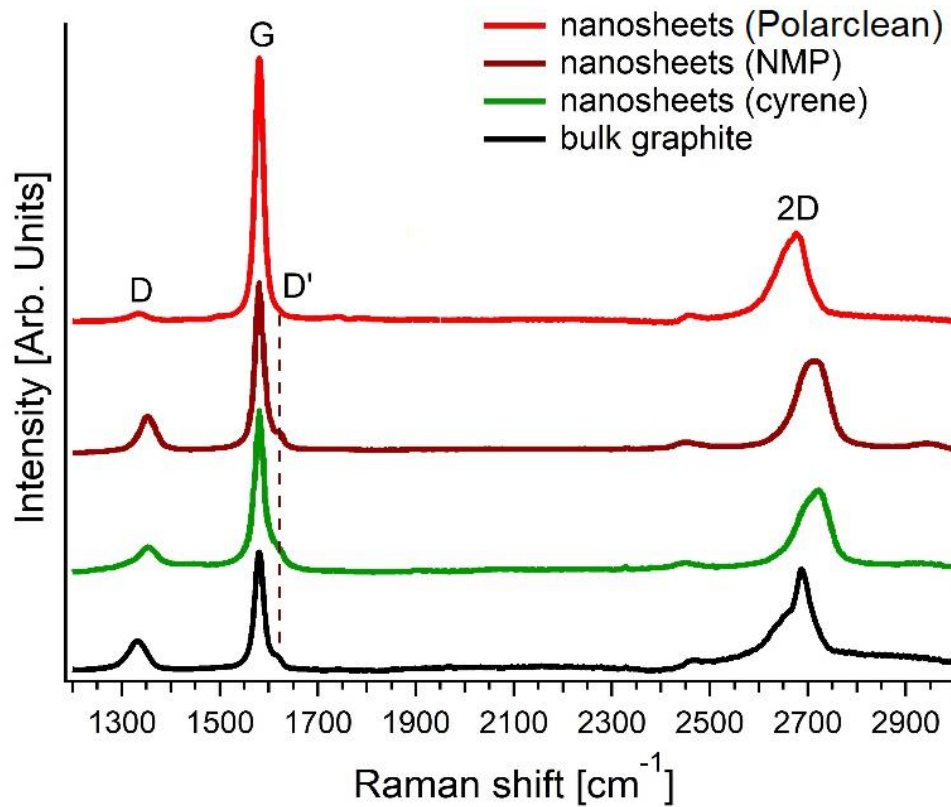


Figure 1.8: Raman spectrum for graphene exfoliated with Polarclean solvent (red curve). For the sake of comparison, we also report Raman spectra for NMP- (brown curve) and Cyrene-assisted (green curve) LPE exfoliated of graphene and, moreover, bulk graphite (black curve).

The analysis of the intensity of the D' band can provide further indication on the density of defects. Similarly to the D band, the D' mode is a double resonance originated by the transverse optical (TO) phonons around the K or K' points in the first Brillouin zone and it is activated by defects, although it involves an intravalley rather than intervalley process ^[40]. Remarkably, the intensity of D' band at 1615 cm^{-1} is suppressed for the case of Polarclean-assisted LPE of graphene, in contrast with the case of other solution processing methods (Figure 1.8).

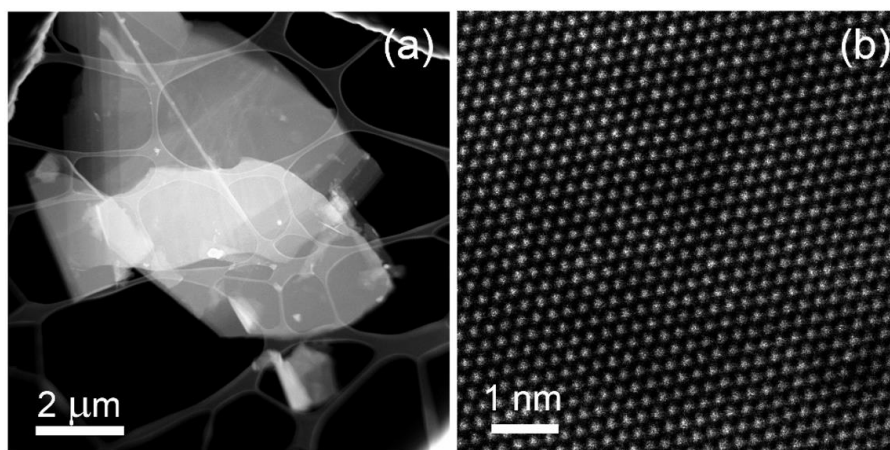


Figure 1.9: (a) Low-magnification HAADF-STEM image of a graphene flake exfoliated with Polarclean; (b) high magnification HAADF-STEM image of one edge of exfoliated graphene flake.

In Figure 1.9 HAADF-STEM images are reported, confirming the presence of large-area graphene flakes, with a lateral size exceeding $10\ \mu\text{m}$, with outstanding crystalline quality and minimized number of defects. Typically, defects in graphene structure can be imaged by using HR-TEM^[43], but we were unable to detect defects in HR-TEM images of our liquid-phase exfoliated graphene nanosheets, consistently with the particularly low value (0.07 ± 0.01) of the $I(\text{D})/I(\text{G})$ ratio measured by Raman spectroscopy. The inspection of a characteristic AFM image (Figure 1.10a) confirms the occurrence of large-area graphene flakes with a terraced structure, as evidenced by the analysis of the height profile. Finally, we measured the absorption spectrum of Polarclean-exfoliated graphene dispersion (Figure 1.10b). The observation of the $\pi \rightarrow \pi^*$ transition^[44] around 265 nm ensures the absence of modifications in the band structure of exfoliated graphene nanosheets.

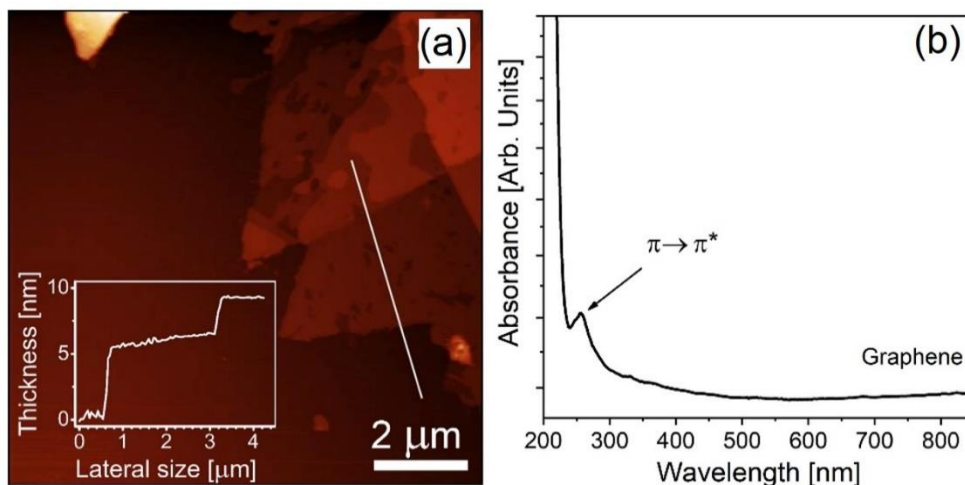


Figure 1.10: (a) AFM image of a graphene flake exfoliated with Polarclean. (b) UV-VIS spectrum of the dispersion of graphene flakes exfoliated with Polarclean.

Conclusions

In conclusion, a systematic fundamental study of GO as a function of its reduction degree tuned via thermal annealing in the temperature range from RT to 670 °C was performed. Samples were investigated with OM, AFM and XPS.

XPS analysis has revealed that the sonication has not changed the chemical composition of the GO and a rationale is given.

In a technical point of view GO could be reduced at temperatures between 300-350 °C and then commercialized. Thus, a decrease of reduction temperature could save money and time that are fundamental for the profits of the company.

The final applications of different type of GO, rGO and graphene are to improve the: (i) adhesion between materials; (ii) electrical, thermal, or photoconductivity of materials; (iii) resistance to certain chemical agents; (iv) mechanical performance; (v) impermeability to certain fluids.

Additionally, we demonstrate that Polarclean represents a unique green candidate solvent for large-scale and scalable production of functional inks based on 2D materials, which naturally enables expanding the use of 2D materials in several application fields.

References

1. Stankovich S, et al. Synthesis of Graphene-Based Nanosheets via Chemical Reduction of Exfoliated Graphite Oxide. *Carbon*. 2007; **45**, 1558 – 65.
2. Eda G, Chhowalla M. Chemically Derived Graphene Oxide: Towards Large-Area Thin-Film Electronics and Optoelectronics. *Adv Mater*. 2010; **22** (22), 2392-415.
3. Dikin DA, Stankovich S, Zimney EJ, Piner RD, Dommett GHB, Evmenenko G, Nguyen ST, Ruoff RS. Preparation and characterization of graphene oxide paper. *Nature*. 2007; **448** (7152), 457-60.
4. Mkhoyan KA, Contryman AW, Silcox J, Stewart DA, Eda G, Mattevi C, Miller S, Chhowalla M. Atomic and electronic structure of graphene-oxide. *Nano Letters*. 2009; **9** (3), 1058-63.
5. Yeh T-F, Syu J-M, Cheng C, Chang T-H, Teng H. Graphite oxide as a photocatalyst for hydrogen production from water. *Adv Funct Mater*. 2010; **20** (14), 2255-62.
6. Krishnamoorthy K, Mohan R, Kim SJ. Graphene oxide as a photocatalytic material. *Appl Phys Lett*. 2011; **98** (24), 244101-.
7. Becerril HA, Mao J, Liu Z, Stoltenberg RM, Bao Z, Chen Y. Evaluation of solution-processed reduced graphene oxide films as transparent conductors. *ACS Nano*. 2008; **2** (3), 463-70.
8. Wang Y, Granados E, Pedaci F, Alessi D, Luther B, Berrill M, Rocca JJ. Phase-Coherent, Injection-Seeded, Table-Top Soft-X-Ray Lasers at 18.9 nm and 13.9 nm. *Nat Photon*. 2008; **2**, 94 - 8.
9. Eda G, Fanchini G, Chhowalla M. Large-area ultrathin films of reduced graphene oxide as a transparent and flexible electronic material. *Nature Nanotechnology*. 2008; **3** (5), 270-4.
10. Robinson JT, Perkins FK, Snow ES, Wei Z, Sheehan PE. Reduced Graphene Oxide Molecular Sensors. *Nano Letters*. 2008; **8** (10), 3137-40.
11. He Q, et al. Centimeter-Long and Large-Scale Micropatterns of Reduced Graphene Oxide Films: Fabrication and Sensing Applications. *ACS Nano*. 2010; **4** (6), 3201-8.
12. Kim H, Miura Y, Macosko CW. Graphene/Polyurethane Nanocomposites for Improved Gas Barrier and Electrical Conductivity. *Chemistry of Materials*. 2010; **22** (11), 3441-50.
13. Liu J, Cui L, Losic D. Graphene and graphene oxide as new nanocarriers for drug delivery applications. *Acta biomaterialia*. 2013; **9** (12), 9243-57.
14. Prasad C, Liu Q, Tang H, Yuvaraja G, Long J, Rammohan A, Zyryanov GV. An overview of graphene oxide supported semiconductors based photocatalysts: Properties, synthesis and photocatalytic applications. *J Mol Liq*. 2020; **297**, 111826.
15. Korkmaz S, Kariper İA. Graphene and graphene oxide based aerogels: Synthesis, characteristics and supercapacitor applications. *Journal of Energy Storage*. 2020; **27**, 101038.
16. Jiang F, Zhao W, Wu Y, Wu Y, Liu G, Dong J, Zhou K. A polyethyleneimine-grafted graphene oxide hybrid nanomaterial: Synthesis and anti-corrosion applications. *Appl Surf Sci*. 2019; **479**, 963-73.
17. Treossi E, Melucci M, Liscio A, Gazzano M, Samori P, Palermo V. High-Contrast Visualization of Graphene Oxide on Dye-Sensitized Glass, Quartz, and Silicon by Fluorescence Quenching. *Journal of the American Chemical Society*. 2009; **131** (43), 15576-.
18. Park S, Lee K-S, Bozoklu G, Cai W, Nguyen ST, Ruoff RS. Graphene Oxide Papers Modified by Divalent Ions-Enhancing Mechanical Properties via Chemical Cross-Linking. *ACS Nano*. 2008; **2**, 572 – 8.
19. Mattevi C, et al. Evolution of Electrical, Chemical, and Structural Properties of Transparent and Conducting Chemically Derived Graphene Thin Films. *Adv Funct Mater*. 2009; **19** (16), 2577-83.
20. Yang D, et al. Chemical analysis of graphene oxide films after heat and chemical treatments by X-ray photoelectron and Micro-Raman spectroscopy. *Carbon*. 2009; **47** (1), 145-52.

21. Ren P-G, Yan D-X, Ji X, Chen T, Li Z-M. Temperature Dependence of Graphene Oxide Reduced by Hydrazine Hydrate. *Nanotechnology*. 2011; **22**, 055705.
22. Xu Y, Cao H, Xue Y, Li B, Cai W. Liquid-Phase exfoliation of graphene: An overview on exfoliation media, techniques, and challenges. *Nanomaterials*. 2018; **8** (11), 942.
23. Nicolosi V, Chhowalla M, Kanatzidis MG, Strano MS, Coleman JN. Liquid Exfoliation of Layered Materials. *Science*. 2013; **340**, 1226419.
24. Hernandez Y, et al. High-yield production of graphene by liquid-phase exfoliation of graphite. *Nature Nanotechnology*. 2008; **3** (9), 563-8.
25. Coleman JN, et al. Two-Dimensional Nanosheets Produced by Liquid Exfoliation of Layered Materials. *Science*. 2011; **331** (6017), 568-71.
26. Coleman JN. Liquid Exfoliation of Defect-Free Graphene. *Acc Chem Res*. 2012; **46** (1), 14-22.
27. Bozso F, Avouris P. Alkali coadsorption and surface coverage effects on electron-stimulated desorption (ESD) - CO and NO on Ni(111). *Chem Phys Lett*. 1986; **125** (5-6), 531-6.
28. Regulation (EC) No . 1907/2006.
29. Sitarek K, Stetkiewicz J. Assessment of reproductive toxicity and gonadotoxic potential of N-methyl-2-pyrrolidone in male rats. *Int J Occup Environ Health*. 2008; **21** (1), 73-80.
30. Randová A, et al. A fundamental study of the physicochemical properties of Rhodiasolv®Polarclean: A promising alternative to common and hazardous solvents. *J Mol Liq*. 2016; **224**, 1163-71.
31. <https://echa.europa.eu/de/registration-dossier/-/registered-dossier/2181/9> [
32. Vidal T, Bramati V, Murthy K, Aribat B. A New Environmentally Friendly Solvent of Low Toxicity for Crop Protection Formulations. *J ASTM Int*. 2011; **8** (6), 1-8.
33. Xie W, Tiraferri A, Liu B, Tang P, Wang F, Chen S, Figoli A, Chu L-Y. First Exploration on a Poly(vinyl chloride) Ultrafiltration Membrane Prepared by Using the Sustainable Green Solvent PolarClean. *ACS Sustainable Chemistry & Engineering*. 2020; **8** (1), 91-101.
34. Lebarbé T, More AS, Sane PS, Grau E, Alfos C, Cramail H. Bio-Based Aliphatic Polyurethanes Through ADMET Polymerization in Bulk and Green Solvent. *Macromol Rapid Commun*. 2014; **35** (4), 479-83.
35. Llevot A, Grau E, Carlotti S, Grelier S, Cramail H. Dimerization of abietic acid for the design of renewable polymers by ADMET. *Eur Polym J*. 2015; **67**, 409-17.
36. Luciani L, Goff E, Lanari D, Santoro S, Vaccaro L. Waste-minimised copper-catalysed azide-alkyne cycloaddition in Polarclean as a reusable and safe reaction medium. *Green Chem*. 2018; **20** (1), 183-7.
37. Li J, Lemme MC, Östling M. Inkjet Printing of 2D Layered Materials. *ChemPhysChem*. 2014; **15** (16), 3427-34.
38. Malard LM, Pimenta MA, Dresselhaus G, Dresselhaus MS. Raman spectroscopy in graphene. *Phys Rep*. 2009; **473** (5-6), 51-87.
39. Ferreira EM, Moutinho MV, Stavale F, Lucchese MM, Capaz RB, Achete CA, Jorio A. Evolution of the Raman spectra from single-, few-, and many-layer graphene with increasing disorder. *Phys Rev B*. 2010; **82** (12), 125429.
40. Cancado LG, et al. Quantifying Defects in Graphene via Raman Spectroscopy at Different Excitation Energies. *Nano Letters*. 2011; **11** (8), 3190-6.
41. Khan U, Porwal H, O'Neill A, Nawaz K, May P, Coleman JN. Solvent-exfoliated graphene at extremely high concentration. *Langmuir*. 2011; **27** (15), 9077-82.
42. Salavagione HJ, Sherwood J, Budarin V, Ellis G, Clark J, Shuttleworth P. Identification of high performance solvents for the sustainable processing of graphene. *Green Chem*. 2017; **19** (11), 2550-60.
43. Robertson AW, Warner JH. Atomic resolution imaging of graphene by transmission electron microscopy. *Nanoscale*. 2013; **5** (10), 4079-93.

44. Grüneis A, Attacalite C, Wirtz L, Shiozawa H, Saito R, Pichler T, Rubio A. Tight-binding description of the quasiparticle dispersion of graphite and few-layer graphene. *Phys Rev B*. 2008; **78** (20), 205425.

Transition metal dichalcogenides: NiTe₂ and PdTe₂

Introduction

Transition-metal dichalcogenides (TMDCs) are attracting a considerable attention^[1], for their intriguing applications capabilities in optoelectronics ^[2-10], catalysis ^[11, 12], gas separation ^[13, 14] and desalination ^[15], arising from their peculiarities, often complementary to those of graphene ^[16-28].

Especially, the interest toward a specific class of TMDCs constituted by NiTe₂, PdTe₂ and PtTe₂ is further motivated by the existence of bulk type-II Dirac fermions, arising from a tilted Dirac cone ^[29]. Recently, type-II Dirac fermions have been experimentally observed in PtTe₂ ^[30, 31], PdTe₂ ^[32, 33] and NiTe₂ ^[34]. To take advantage of their extraordinary technological potential, the assessment of their chemical and thermal stability is crucial ^[35]. Chemical and thermal stability represent crucial bottlenecks in the prospect of technological exploitation of materials “beyond graphene” ^[36-38]. Definitely, chemical instability is usually associated to the chemical reactivity of the surface ^[39] and to presence of intrinsic ^[40] or extrinsic ^[39] defects. These aspects discriminate between materials with rapid surface degradation ^[41, 42] or ambient-stable ^[43-46].

Usually, as-cleaved surfaces of TMDCs have a surface termination constituted by an atomic layer of chalcogens^[45]. The lone pair electrons of chalcogen atoms play a pivotal role in surface stability ^[47]. Correspondingly, the minimized amount of chalcogen vacancies is important for surface protection

from unwanted reactions with environmental species, especially surface oxidation [45, 48-54].

Thermal stability is also crucial for industrial use of TMDCs, considering that TMDC-based electronic devices will be subjected to heating caused by current flow, light absorption, etc. In particular, thermal stability is evidently essential for high-temperature electronic devices, which are present in combustion systems, air stagnation points in supersonic aircraft, vehicle brakes, nuclear reactors, and industrial processes [55]. Furthermore, thermal stability is mandatory for successful use in (i) distillation for seawater desalination [56], (ii) crystallization processes [57] and (iii) thermoelectricity [58]. Nevertheless, in many cases TMDCs are thermally unstable with heating-induced modifications in the electron mobility [59], self-healing of vacancy defects [60] or loss in stoichiometry, due to the desorption of chalcogen atoms at temperature as low as 470 K for MoS₂ [61].

Recently, atomically thin layers of PdTe₂ [62] were proposed as thermoelectric materials with predicted ZT values as high as 1.18 [62], comparable with values for state-of-the-art thermoelectric materials as Bi₂Te₃ [63]. Moreover, PdTe₂ has also attracted great interest in consideration of the presence of type-II Dirac fermions [33, 64] and for the observation of superconductivity [32, 33, 65, 66].

In this chapter the study of the chemical and thermal stability of these materials through experiments by X-ray photoelectron spectroscopy (XPS), atomic force microscopy (AFM) and high-resolution electron energy loss spectroscopy (HREELS) is reported.

It is shown that the Te termination in an oxygen-rich environment (as in ambient atmosphere) evolves in a sub-nanometric passivation layer of TeO₂, which saturates in a few minutes and remains stable in a timescale extended up to one year. The formation of tellurium-oxide phases is favored in the presence of Te vacancies. Ambient-stable PdTe₂ was employed to fabricate millimeter-wave receivers, which show negligible changes in responsivity in a timescale of 1 month, even without encapsulation of the active channel. Correspondingly, NiTe₂-based devices show current-voltage characteristics with negligible changes over a timescale of one month. Moreover, PdTe₂ and NiTe₂ represent good candidates for perfectly CO-tolerant electrodes for electrocatalysis [67, 68].

Methods

Computational method and model. The atomic structure and energetics of various configurations of various gases adsorbed on NiTe₂ and PdTe₂ were studied by DFT using the QUANTUM-ESPRESSO code [69] and the GGA-PBE + van der Waals approximation. Energy cutoffs of 25 and 400 Ry for the plane-wave expansion of the wave functions and the charge density, respectively, and the 4×4×3 Monkhorst-Pack k-point grid for the Brillouin zone sampling were used [70]. For modeling the NiTe₂ and PdTe₂ surface, a slab of three layers was used, respectively. The presence of the Te vacancies in the top layer of PdTe₂ was also considered. The formation of the single vacancy corresponds to PdTe_{1.88} for the outermost surface layer.

Physisorption enthalpies were calculated by the standard formula:

$$\Delta H_{\text{phys}} = [E_{\text{host+mol}} - (E_{\text{host}} + E_{\text{mol}})]$$

where E_{host} is the total energy of the pristine surface, and E_{mol} is the energy of a single molecule of the selected species in an empty box. For the case of physisorption, we also evaluated the differential Gibbs free energy by the formula:

$$\Delta G = \Delta H - T\Delta S$$

where T is the temperature and ΔS is the change of entropy of the adsorbed molecule. The entropy was estimated considering the gas to liquid transition by the standard formula:

$$\Delta S = \Delta H_{\text{vaporisation}}/T$$

where ΔH vaporization is the measured enthalpy of vaporization.

Single-crystal growth. Single crystals of NiTe₂ and PdTe₂ were grown using the Te flux method. The starting mixtures were made by Ni powder (99.99%) and Te ingots (99.9999%) in ratio 1:8 for NiTe₂, Pd sheet (99.9%) and Te powder (99.9999%) ratio 1:2 for PdTe₂; each mixture were sealed under vacuum in a quartz tube. The flat surface of the crystal corresponds to the (001) plane. The

crystal structure and phase purity of the as-grown crystals were identified by X-ray diffraction (XRD) (Bruker D2 PHASER) using Cu K α radiation and Laue diffraction (Photonic Science) at room temperature.

Raman spectroscopy. Micro-Raman spectra were acquired at room temperature by using a LABRAM spectrometer with a 1800 lines/mm diffraction grating equipped with a He–Ne laser source ($\lambda = 632.8$ nm) and an optical microscope with a 100x MPLAN with numerical aperture of 0.9. The laser spot cross diameter is ~ 2 μm . The system operates in a back-scattering configuration.

AFM. AFM images were acquired with a Digital D5000, Veeco system operating in Tapping-mode. The resonance frequency of the tip is 75 kHz.

HREELS. Vibrational experiments were carried out at room temperature with a Delta 0.5 spectrometer (Specs GmbH, Germany). The experimental resolution is 3-4 meV.

Synchrotron radiation spectroscopies. XPS measurements were carried out on the CNR BACH beamline at Elettra Sincrotrone in Trieste (Italy) for NiTe₂ and at the High-Energy branch of the Advanced Photoelectric Experiments beamline (APE-HE) of the Elettra Synchrotron, Trieste, Italy for PdTe₂. The sputtering of PdTe₂ was performed at room temperature, using Ar⁺ ions with an impinging energy of 1 keV. The Ar⁺ flux was 10^{13} ions cm⁻² s⁻¹. Under our experimental conditions, we had any evidence of beam-induced damage even after long-time exposure to synchrotron light.

Device Fabrication. Thin NiTe₂ flakes (with thickness around 70 nm) were obtained by mechanical exfoliation from bulk crystals and quickly transferred onto a 300 nm SiO₂/Si substrate. Electrodes were then patterned by ultraviolet lithography with a AZ5214 developer. Finally, 5 nm Cr/70 nm Au contacts were prepared using electron-beam evaporation. The current–voltage characteristics of the fabricated devices were recorded at room temperature using an Agilent B2912A Semiconductor Analyzer.

The PdTe₂-based millimeter-wave detector was fabricated by electron beam lithography and electron beam evaporation. Photocurrent experiments were performed by using a lock-in amplifier (LIA) after a low-noise voltage preamplifier. The current–voltage characteristics were measured by using B2912A Semiconductor Analyzer.

Results and discussion

PdTe₂ and NiTe₂ crystallize in the CdI₂-type trigonal (1T) structure with P-3m1 space group (No. 164), sketched in Figure 2.1 panels (a) and (b). Each transition metal atom at the basal plane is surrounded by six Te atoms, forming Ni(Pd)Te₆ octahedra. As-cleaved sample of PdTe₂ show a low-energy electron diffraction (LEED) pattern with sharp spots against a low background, indicating high crystalline quality of the as-cleaved surface (Figure 2.1d). Crystalline quality was also assessed by X-ray diffraction (XRD) Figure 2.1c. Also, for NiTe₂ crystalline quality was assessed by XRD and LEED Figure 2.1e-f (details of the XRD in Appendix B). Moreover, the absence of contamination was confirmed by an X-ray photoelectron spectroscopy (XPS) survey scan of the as-cleaved samples (Figure A.2 Figure A.3). Figure 2.1g shows two Raman active bands at around 84 and 140 cm⁻¹. These modes are assigned to E_g and A_{1g} phonons, respectively. (Further information on the identification of Raman peaks in the Appendix C).

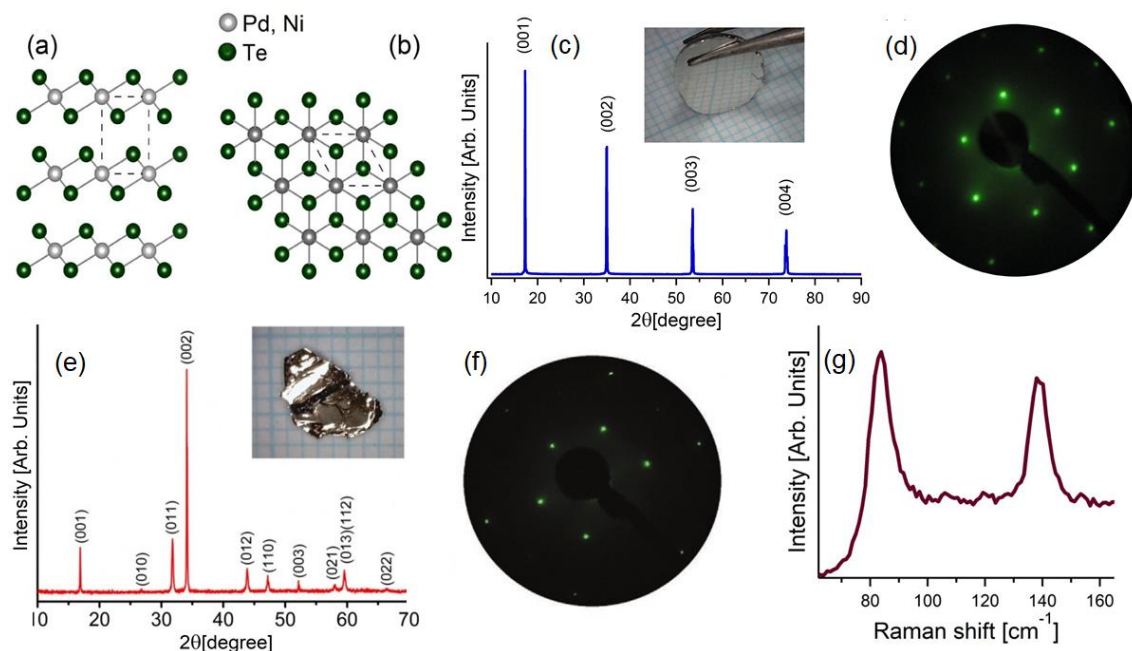


Figure 2.1: (a) Side and (b) top views of the atomic structure of Pt, Pd, NiTe₂. Grey balls denote Pd or Ni atoms, while green balls represent Te atoms. (c) The XRD pattern of single crystals of PdTe₂, taken with Cu K α . The inset shows the photo of grown single-crystal samples. d) The LEED pattern of PdTe₂, measured with a primary electron beam

energy of 68 eV. (e) The XRD pattern of single crystals of NiTe₂, taken with Cu K α . The inset shows the photo of grown single-crystal samples. (f) The LEED pattern of NiTe₂, measured with a primary electron beam energy of 84 eV. (g) The Raman spectrum of NiTe₂ single crystal acquired at room temperature with laser $\lambda = 632.8$ nm.

Surface Chemical Reactivity. To evaluate the stability and the chemical reactivity of NiTe₂ and PdTe₂, we modelled the energetics of the adsorption and decomposition of various gases on their surfaces (see Table I).

For NiTe₂ and PdTe₂ the differential Gibbs free energy ΔG for adsorption of molecular oxygen at room temperature is negative (-43.4 and -55.49 kJ/mol, respectively), thus indicating that its adsorption is energetically favorable. Decomposition of the adsorbed O₂ molecules is favorable for the case of oxygen for both NiTe₂ and PdTe₂ (-112.3 and -94.4 kJ/mol, respectively). Concerning water adsorption, it is energetically unfavorable at room temperature for both surfaces, as indicated by the positive values of ΔG +3.1 and +11.9 kJ/mol, respectively.

It is also particularly relevant to assess the energetics for CO chemisorption. As a matter of fact, Ni-based alloys are usually affected by the problem of CO poisoning at room temperature^[67]. Moreover, the absorption of carbon monoxide is energetically unfavorable for both NiTe₂ and PdTe₂, with ΔG values of +4.9 kJ/mol and +9.45 kJ/mol, respectively.

Table I: Differential enthalpy ΔH and differential Gibbs free energy ΔG of adsorption of CO, H₂O and O₂ at room temperature on pristine NiTe₂, PdTe₂, NiTe_{1.88} and PdTe_{1.88} surfaces, respectively and their related decomposition energy.

Surface	Chemical species	Physisorption		Decomposition
		ΔH [KJ/mol]	ΔG [KJ/mol]	ΔH [KJ/mol]
NiTe ₂	CO	-14.4	+4.9	-
	O ₂	-54.6	-43.3	-112.3
	H ₂ O	-28.8	+3.1	+169.9
NiTe _{1.88}	CO	-85.9	-66.3	-
	O ₂	-117.4	-106.1	+9.7
	H ₂ O	-15.0	+16.3	+151.7

PdTe ₂	CO	-9.9	+9.4	-
	O ₂	-66.7	-55.4	-94.4
	H ₂ O	-19.3	+11.9	+131.4
PdTe _{1.88}	CO	-9.4	+9.9	-
	O ₂	-53.7	-52.4	-92.2
	H ₂ O	-20.2	+11.0	+167.6

Thus, NiTe₂ and PdTe₂ are not affected by CO poisoning, thus suggesting their potential use as electrode materials for electrocatalysis [67, 68]. The impact of Te vacancies on surface chemical reactivity has been also assessed. The presence of the vacancies was considered in the top layer. In particular, the adsorption of molecular oxygen becomes favorable for NiTe_{1.88} ($\Delta G = -212.1$ kJ/mol, $\Delta G = -106.1$ kJ/mol) with respect to the pristine surfaces of NiTe₂, while no substantial changes between PdTe_{1.88} and PdTe₂ exist.

The decomposition of oxygen is favorable for PdTe₂ ($\Delta H = -94.4$ kJ/mol), while for NiTe₂ it is energetically unfeasible ($\Delta H = +9.7$ kJ/mol). Notably, water splitting is energetically unfavorable on all surfaces.

To evaluate the effect of a larger concentration of vacancies, we also considered two Te vacancies in the top layer (PdTe_{1.73}). We considered various locations of the second Te vacancy, finding that the most energetically favorable position is in the nearness of the first vacancy, detail in ref. [71].

To validate the theoretical results, we carried out experiments using several surface-science techniques. Each of these probes a different property of the material, so that the combination of tools provides a comprehensive understanding of the surface physicochemical properties.

To assess the surface chemical reactivity of NiTe₂ and PdTe₂, we performed high-resolution X-ray photoelectron spectroscopy (XPS) experiments (Figure 2.2 and Figure 2.4).

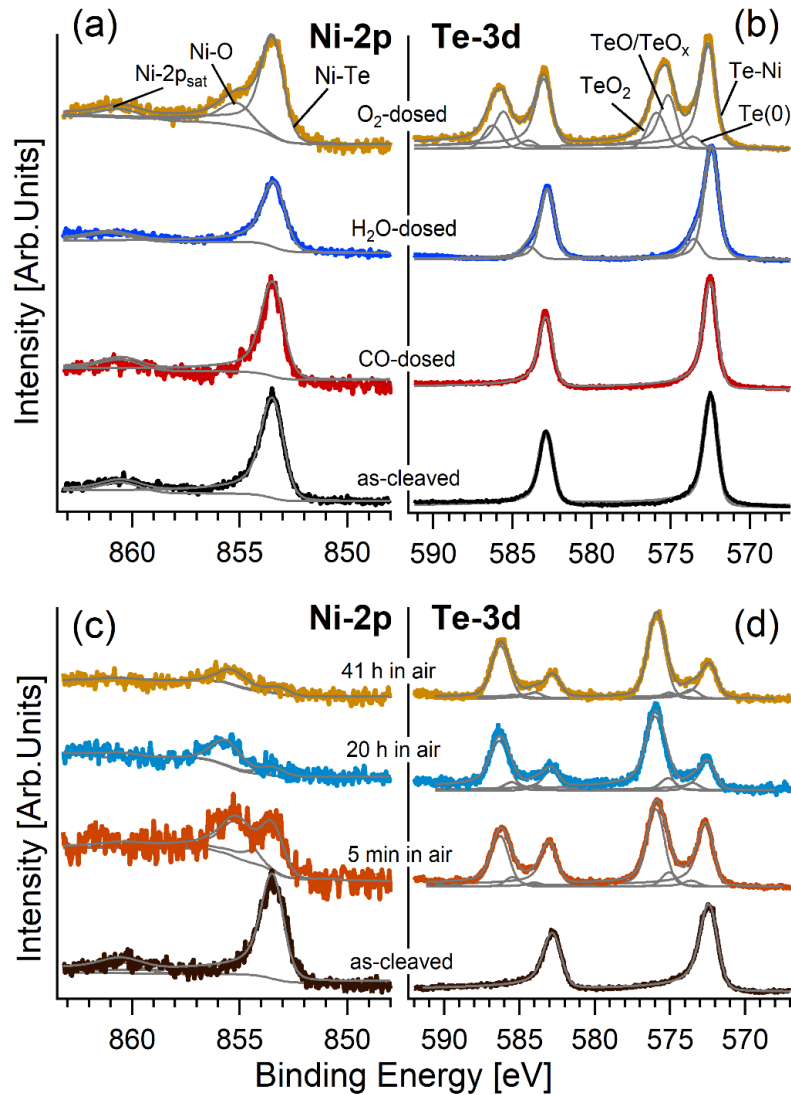


Figure 2.2: Core-level spectra of (a) Ni-2p and (b) Te-3d for as-cleaved NiTe₂ and for the same surface exposed to CO, H₂O and O₂ at $2 \cdot 10^4$ L ($1 \text{ L} = 1.33 \times 10^{-6} \text{ Torr} \cdot \text{s}$), respectively. Core-level spectra of (c) Ni-2p and (d) Te-3d for as-cleaved, 5 min in air, 20 h in air and 41 h in air on NiTe₂, respectively. The photon energy is 1000 eV.

We focused on the evolution of core levels upon various treatments. In Figure 2.2 we show the Ni-2p and Te-3d core level for the as-cleaved and the same surface after the exposure toward different gases. The Ni-2p core levels are practically unchanged upon CO dosage. Similarly, H₂O exposure just attenuates the signal by 60% but without the emergence of novel features, thus excluding any water adsorption at Ni sites. No changes in the Te-3d spectrum after CO exposure. Conversely, a new component at 573.4 eV, ascribed to the formation of the Te(0) species^[72], appears in the Te-3d spectra after H₂O exposure. The analysis

of O-1s spectra (Figure 2.3) indicates the absence of oxygen species in the CO-dosed sample, confirming the inertness of NiTe₂ surface toward CO. Conversely, the O-1s core level of H₂O-dosed sample shows the presence of hydroxyl groups and molecular water [73-76]. For the O₂-dosed surface, the O-1s spectrum confirms the formation of an oxide species.

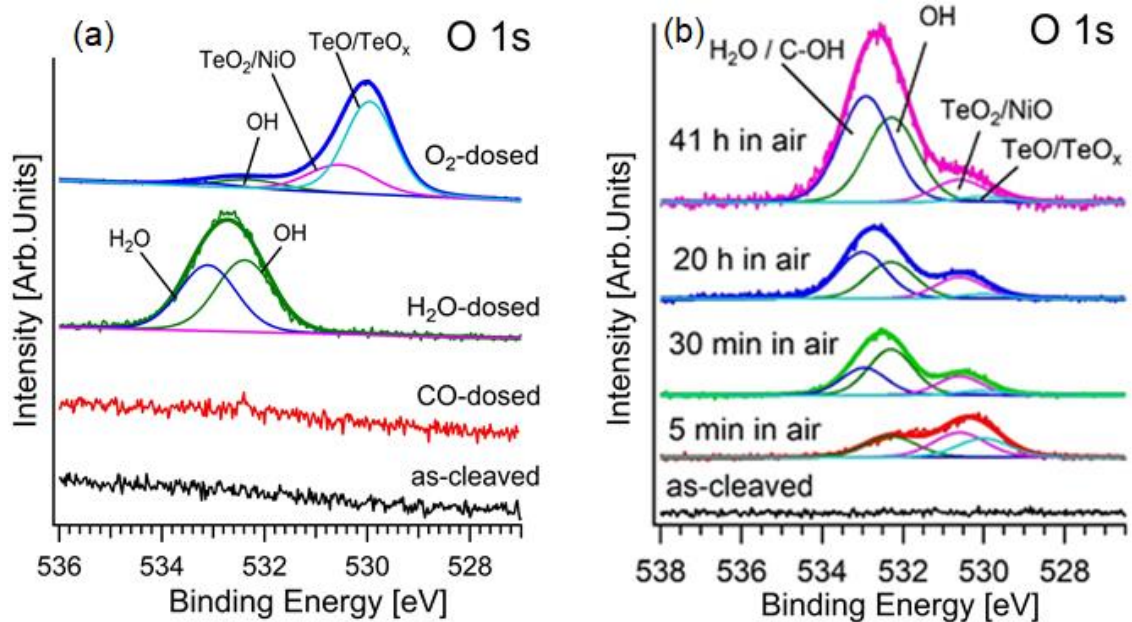


Figure 2.3: (a) Core-level spectra of O-1s for as-cleaved NiTe₂ and for the same surface exposed to CO, H₂O and O₂, respectively. (b) Core-level spectra of O-1s for NiTe₂ surface kept in air for 5 min, 30 min, 20 h and 41 h, respectively. The photon energy is 596 eV.

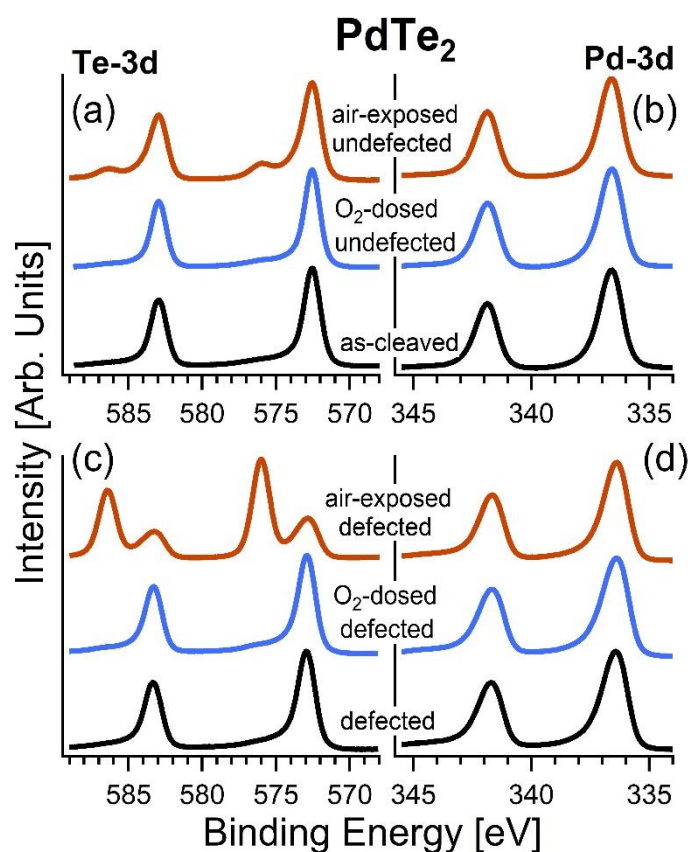


Figure 2.4: (a-b) Te-3d and Pd-3d core levels for pristine, as-cleaved surface of PdTe₂ and for its modification upon O₂ dosage (10⁵) and air exposure. Panels (c-d) report the same for defected (PdTe_{1.7}). The photon energy is 800 eV and the spectra are normalized to the maximum.

From the analysis of PdTe₂ XPS spectra in Figure 2.4, we infer that the as-cleaved undefected surface of PdTe₂ are inert toward oxygen exposure up to 10⁶ L (1 L = 1.33 × 10⁻⁶ Torr·s). In fact, the Te-3d core level is unchanged for PdTe₂ (Figure 2.4 (a,b)) [45].

Different behavior is found in O₂-dosed NiTe₂. The intensity of the Ni-2p level is reduced by 42% with the emergence of a new component at 855.5 eV (BE), which is related to Ni-O bonds [77]. Correspondingly, new components of Te-3d appear at higher BEs. The appearance of novel components located at 576.0 and 575.1 eV can be ascribed to the formation of TeO₂ and TeO_x [72, 78, 79]. The effects of CO, O₂ and H₂O gas exposure on the electronic properties of NiTe₂ were also assessed by measuring valence-band spectra (Figure 2.5a). The consistency of these spectra demonstrates that the electronic properties are negligibly affected

by gas exposure.

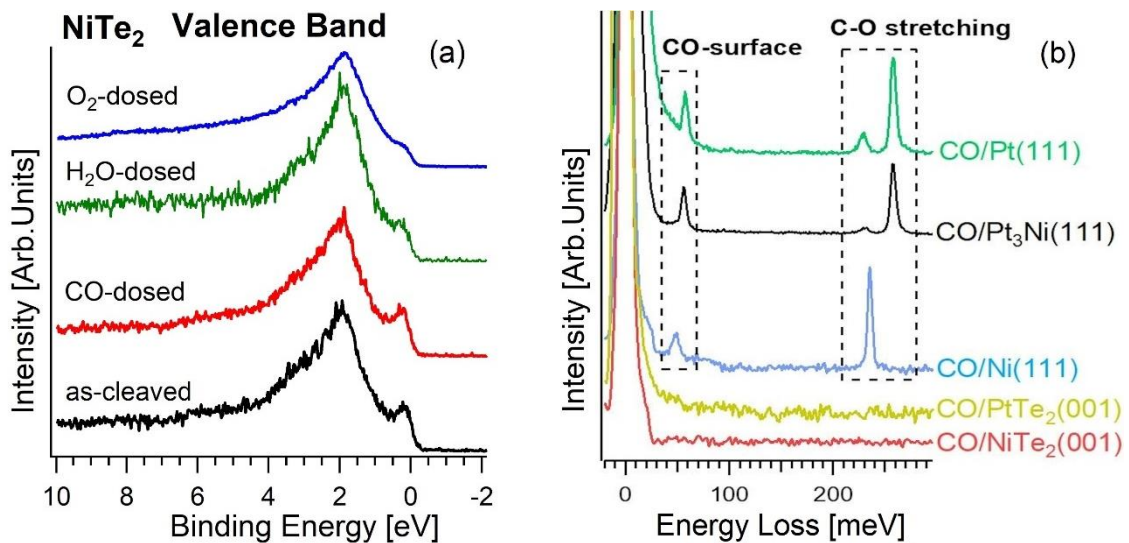


Figure 2.5: (a) Valence band for as-cleaved NiTe₂ and for the same surface exposed to CO, H₂O and O₂, respectively. The photon energy is 596 eV and the spectra are normalized to the maximum. (b) Vibrational spectra after having saturated with CO the surfaces of NiTe₂ (001), PtTe₂ (001), Ni(111), Pt₃Ni(111) and Pt(111). The saturation has been reached at only 5, 10, and 8 L (1 L = 10⁻⁶ Torr-s) for Ni(111), Pt₃Ni(111) and Pt(111). On the other hand, no CO-derived features are achieved even after exposure to 10¹⁰ L on NiTe₂ (001) and PtTe₂ (001). Specifically, the CO-derived features are the vibration of the whole CO molecule against the substrate at 50 meV and the intramolecular C-O stretching, whose energy depends on the adsorption site: 230 meV for three-fold site, selectively occupied on Ni^[80], while it is minority on Pt₃Ni(111)^[67, 81] and Pt(111)^[67], and 250 meV for the on-top adsorption site, majority on both Pt₃Ni(111) and Pt(111).

We directly assessed the problem by CO poisoning by exposing a NiTe₂ sample to CO by using the technique with highest sensitivity to CO adsorption, i.e. high-resolution electron energy loss spectroscopy (HREELS), due to the high oscillating dipole for the C-O intramolecular stretching^[82-84]. Specifically, we dosed CO to (i) NiTe₂ (001); (ii) Ni(111); (iv) Pt₃Ni(111); and (v) Pt(111) surfaces, see Figure 2.5 b. Experiments were carried out in specular conditions to activate the dipole scattering regime. We obtain that, while Ni(111), Pt₃Ni(111) and Pt(111) are poisoned by CO, as evidenced by the observation of C-O stretching and the CO-substrate vibrations, NiTe₂ and PtTe₂ are totally inert toward CO, even after prolonged CO exposure up to 10¹⁰ L.

Ambient stability. The as-cleaved NiTe₂ and PdTe₂ were also directly exposed to the atmosphere with the aim to assess their ambient stability as shown in Figure 2.2c-d and Figure 2.4c-d. For the case study of NiTe₂, a few minutes of exposure in air are sufficient to create a passivation layer of TeO₂, whose thickness is estimated to be $\sim 7 \text{ \AA}$ by quantitative XPS^[85,86] (according to methods described in appendix E p.87). A prolonged exposure time (up to 2 days) does not induce further oxidation of the NiTe₂ surface. Especially, the analysis of Te-3d core levels after 5 minutes in air indicates the formation of only a slight amount of Te(0) species, together with TeO_x and TeO₂ species. The TeO_x is converted in TeO₂ over the time, while Te(0) remains constant. The TeO₂ component reached the maximum after 30 min in air and no further changes emerge over the time. Correspondingly, the Ni-2p core level displays a NiO component that reaches a maximum after 30 minutes, and no further changes were observed for a longer time exposure. Analysis of the O-1s core-level spectra (Figure 2.3b) indicates that the amount of surface oxide remains unchanged for exposure times longer than 30 minutes, while the intensity of the components related to adsorbed H₂O and C-OH contamination^[87, 88] increases with time. To evaluate the environmental stability, we also performed time-evolution atomic force microscopy (AFM) experiments on mechanically exfoliated flakes (Figure 2.6). The evolution was followed on a timescale of up to 10 days. The AFM results demonstrate that exposure to the atmosphere does not change the morphology of the flakes, as confirmed by the height profile along a specific direction remaining constant with exposure (Figure 2.6c).

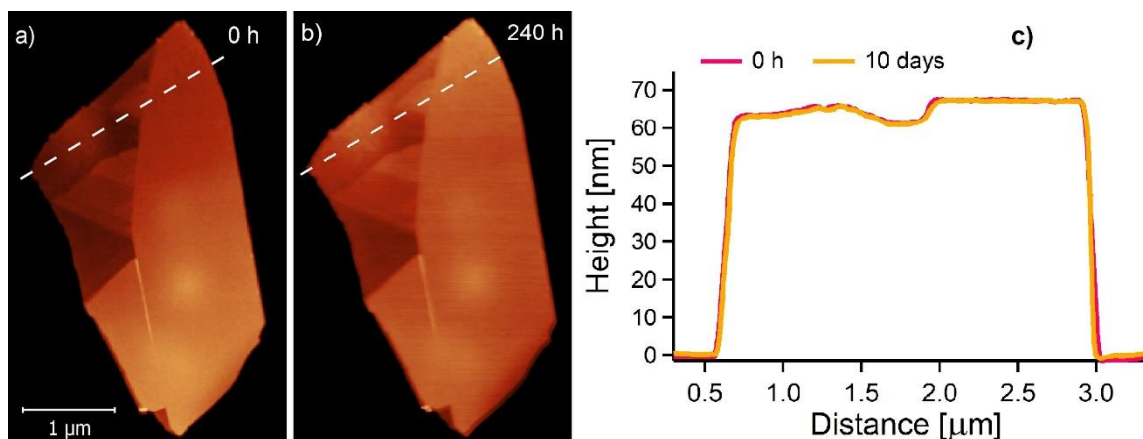


Figure 2.6: Time evolution of AFM images of a $\sim 60 \text{ nm}$ thick flake of NiTe₂. Panel a)

shows the flake immediately after exfoliation, while panels b) shows the same flake after 240 h in air. The dotted white lines indicate the path of the height profile shown in panel (c).

In the case of PdTe₂, we evaluated the thickness of the TeO₂ skin after air exposure to be ~ 3 Å after 10 min and ~ 9 Å after 1 year (see Appendix E for detailed calculation). With the aim to evaluate the impact of Te vacancies, we have repeated experiments for a sample with implanted Te vacancies (PdTe_{1.7}). However, any noticeable difference with the pristine, undefected sample is observed, except a faster oxidation kinetics. Precisely, the TeO₂ skin is already ~ 5.8 Å after 10 minutes in air. We have also checked the influence of the oxidation on electronic structure of PdTe₂ by measuring valence-band spectra (Figure 2.7). Upon oxidation we observe the appearance of a mode at a binding energy of ~ 18 eV, due to O-2s states in TeO₂. Such a feature is observed as a weak component after a short-term exposure (10 min) to air (blue curve in Figure 2.7) and becomes an intense peak only in aged samples (kept in air for 1 year, green curve in Figure 2.7).

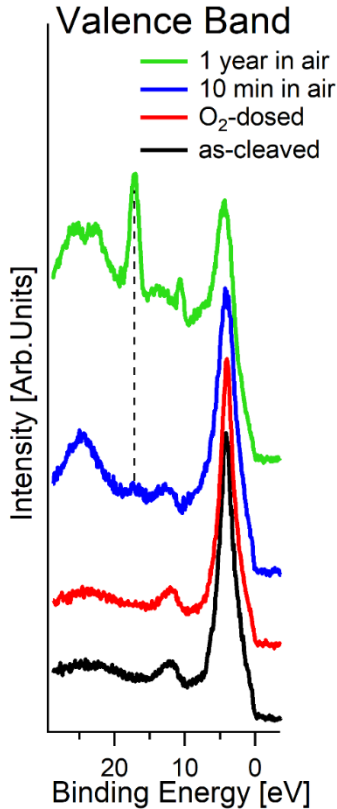


Figure 2.7: Valence-band spectra for the as-cleaved PdTe₂ surface (black curve) and for its modification upon O₂ dosage (10⁵ L at room temperature, red curve), air exposure for 10 minutes (blue curve) and aging of one year in air (green curve), respectively. The photon energy is 400 eV.

Also in this case time evolution of AFM images of mechanically exfoliated flakes (Figure 2.8) was followed on a timescale extended to one month. AFM results demonstrate that exposure to ambient atmosphere does not change the morphology of the flakes, as confirmed by the height profile along a specific direction remaining constant with exposure (Figure 2.8c).

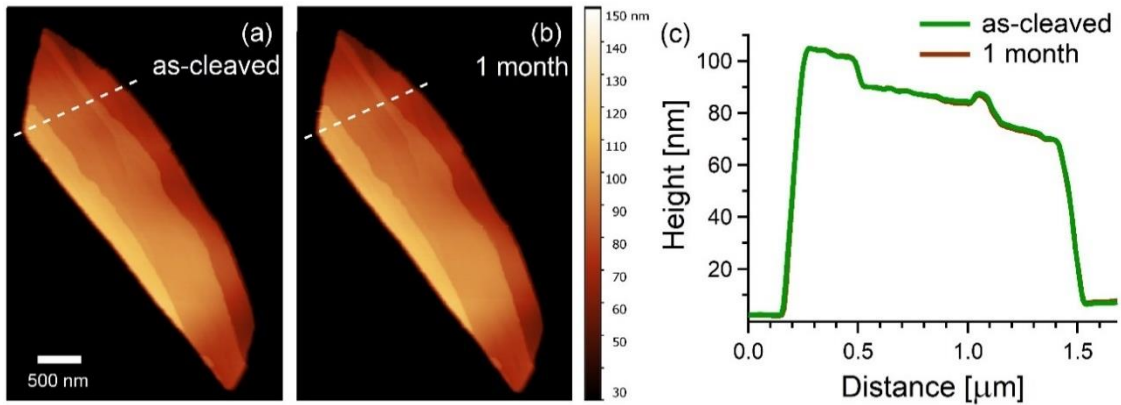


Figure 2.8: Time evolution of AFM images of a ~ 100 nm thick flake of PdTe₂. Panel (a) shows the flake immediately after exfoliation, while panel (b) displays the same flake after one month in air. The dotted white lines indicate the path of the height profile shown in panel (c).

To confirm the air stability of NiTe₂ and PdTe₂ different devices were realized.

For the NiTe₂-based devices we realized a field-effect transistor, with the uncapped active channel of NiTe₂ (Figure 2.9a-b). The output current versus voltage is reported in Figure 2.9c. NiTe₂-based device shows a negligible (albeit noticeable) decay in the output current. Specifically, the current experiences drop from 2.42 to 2.35 mA at 100 mV (Figure 2.9c) within 9 days, which is less than 3% of the original value. Minimal changes should be ascribed to air-induced modifications to the metal-NiTe₂ interface rather than the active channel, on the basis of the AFM (Figure 2.6) and XPS (Figure 2.2) aging experiments. For the sake of comparison, we note that in a similar FET fabricated with black phosphorus, the output current exhibits a decay by an order of magnitude in only two weeks due to surface oxidation in air^[89].

To further verify the air stability of the NiTe₂ and PdTe₂ nanodevices, a high-frequency test was carried out to evaluate the generation-recombination noise associated with material degradation^[90]. We tested the suitability of NiTe₂ and PdTe₂ for high-frequency electronics (Figure 2.9a-b and Figure 2.10a-b) and, specifically, for the buildup of the next wireless communication network at a high data rate. Explicitly, the device was subjected to electromagnetic radiation at a 40 GHz carrier-wave frequency, which has been proposed by Global Mobile Supplier Association^[91] as the hotspot for the next interconnected

communication system.

For the NiTe₂ and PdTe₂ the output of the fabricated devices show a good repetition ability with sharp rise/fall times, closely following the coded digital signal Figure 2.9e and Figure 2.10f. The signal exhibits especially good repeatability without decay even after a one-month exposure to the ambient environment, thus elucidating the superb stability of a NiTe₂ and PdTe₂ devices working at a frequency above the cut-off frequency (12 GHz) of a transistor with a micrometer-long channel ^[92].

As shown in Table II, the NiTe₂-based receiver exhibits higher current responsivity and lower impedance for high-speed data transmission with respect to similar devices based on graphene and black phosphorus.

Table II: Comparison of the performance of receivers based on graphene, black phosphorus and NiTe₂ at 40 GHz carrier frequency.

	graphene	black phosphorus	NiTe ₂
Resistance	2.2 k Ω	1 k Ω	60 k Ω
Responsivity(A/W)	1.50 \pm 0.01	0.74 \pm 0.01	5.18 \pm 0.01

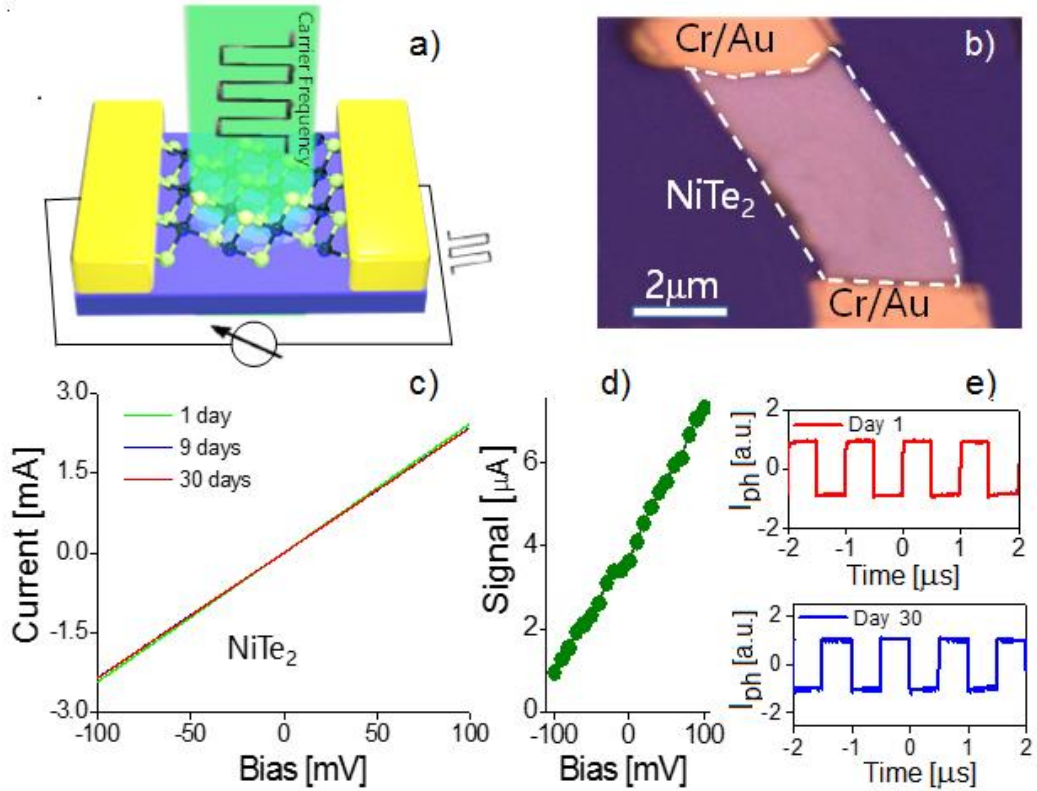


Figure 2.9: (a) Schematic diagram of the nanodevice with a NiTe₂-based active channel and working as a high-frequency receiver; (b) optical microscopy of NiTe₂-based FET obtained from mechanically exfoliated bulk single crystal; (c) current-voltage characteristics measured after the indicated periods of time. Panels (d) and (e) are related to the data rate measurement of a NiTe₂-based nanodevice working as a receiver at a 40 GHz carrier frequency. Specifically, panel (d) shows the signal magnitude as function of bias voltage, while panel (e) reports the comparative evaluation of the data rate for the as-fabricated device (top sub-panel) and after one month (bottom sub-panel).

Moreover, in the case of PdTe₂ we made a direct comparison with similar devices fabricated with black phosphorus and graphene (Figure 2.10c-d). It is also worth noticing that other TMDCs, including MoS₂ and WS₂, effectively work at frequency lower than 10 GHz, because of their low mobility achieved in experimental studies (few tens of cm²V⁻¹s⁻¹ [93]), which represents a serious hurdle for their usage in high-frequency electronics [94]. Notably, PdTe₂-based millimeter-wave detectors are more sensitive than similar devices based on black phosphorus and graphene (Figure 2.10c-d). Specifically, photocurrent values are higher in PdTe₂ by even an order of magnitude compared to black phosphorus and graphene, as it can be inferred from the behavior of the power-dependent

photocurrent (Figure 2.10c). By comparing the behavior of the photocurrent as a function of the bias voltage (Figure 2.10d), it is also evident that the PdTe₂-based device possesses larger dynamic regime than black phosphorus- and graphene-based devices for carrier-frequency conversion. Specifically, the dynamic regime, defined as the ratio between the photocurrent at 100 and 0 mV, i.e. $20\log(I_{ph_100mV}/I_{ph_0mV})$, is 35 dB for PdTe₂, 12 dB for graphene and 6 dB for black phosphorus. Explicitly, under the same operational conditions ($f = 40\text{ GHz}$; $V_{sd} = 100\text{ mV}$, $P = 30\text{ mW}$), the responsivity of the PdTe₂-based millimeter-wave receiver (6.4 A/W) is 23 and 13 times greater than that of similar devices based on graphene and black phosphorus, respectively.

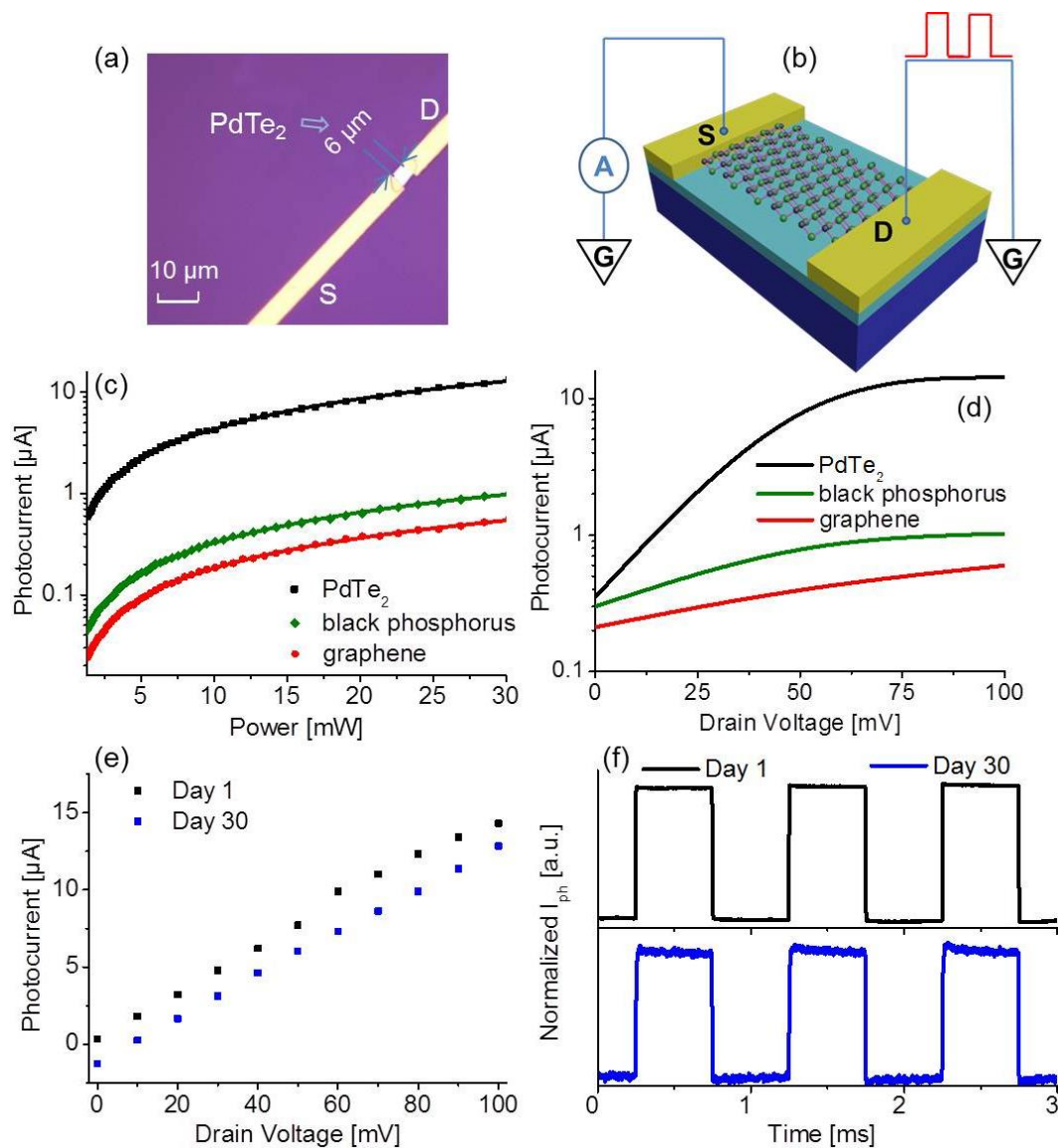


Figure 2.10: (a) Optical micrograph of the PdTe₂-based device; (b) architecture of PdTe₂

millimeter-wave receiver; (c) power dependence of PdTe₂ (black curve), black phosphorus- (green curve) and graphene-based (red curve) devices; (d) bias dependence of PdTe₂ (black curve), black phosphorus (green curve) and graphene-based (red curve) devices; (e) photosignal of the as-fabricated PdTe₂ device (black squares) and after one month in air (blue squares); (f) time-resolved response of the as-prepared PdTe₂ millimeter-wave receiver (black curve) and after one month in air (blue curve).

Thermal Stability. We also assessed the thermal stability in vacuum of the PdTe₂ surface, with a particular care to the possible influence of surface TeO₂ phases. Figure 2.11 shows the evolution upon heating of Pd-3d and Te-3d core levels measured for panels a,b the as-cleaved, undefected PdTe₂ surface and panels c,d in the presence of the surface TeO₂ phase, respectively. We focused on the evolution of Te-3d core levels upon annealing for the case of the oxidized surface, as compared to spectra acquired for pristine PdTe₂. The temperature increase induces notable changes in the intensity of the oxide component of the Te-3d core-level spectra. Specifically, the relative weight of the oxide component in Te-3d core levels decreases with increasing heating temperature. We attribute the modification of the core-level spectra to the thermal reduction of surface TeO₂ phases. The reduction process also continues during the cooling procedure, with a final reduction of the oxide component to 62 % with respect to the initial value, after thermalization at room temperature.

Conversely, no change is found for Pd-3d core levels for both (i) pristine, undefected PdTe₂ and (ii) the oxidized surface after the heating/cooling process.

The analysis of the valence band could provide further insights on the influence of TeO₂ phases and their thermal reduction on the electronic properties. In Figure 2.12, the valence band of the pristine and oxidized PdTe₂ is reported for different heating temperatures with subsequent cooling. Valence band for as-cleaved pristine surface is unmodified by the annealing treatment, confirming that the pristine surface is thermally stable. Contrariwise, the valence band of oxidized PdTe₂ displays a different behaviour. Specifically, the broad peak at 6-7 eV, associated to O-2p states, decreases its intensity when temperature increases from 300 up to 540 K. During the cooling procedure, the intensity of this feature remains constant.

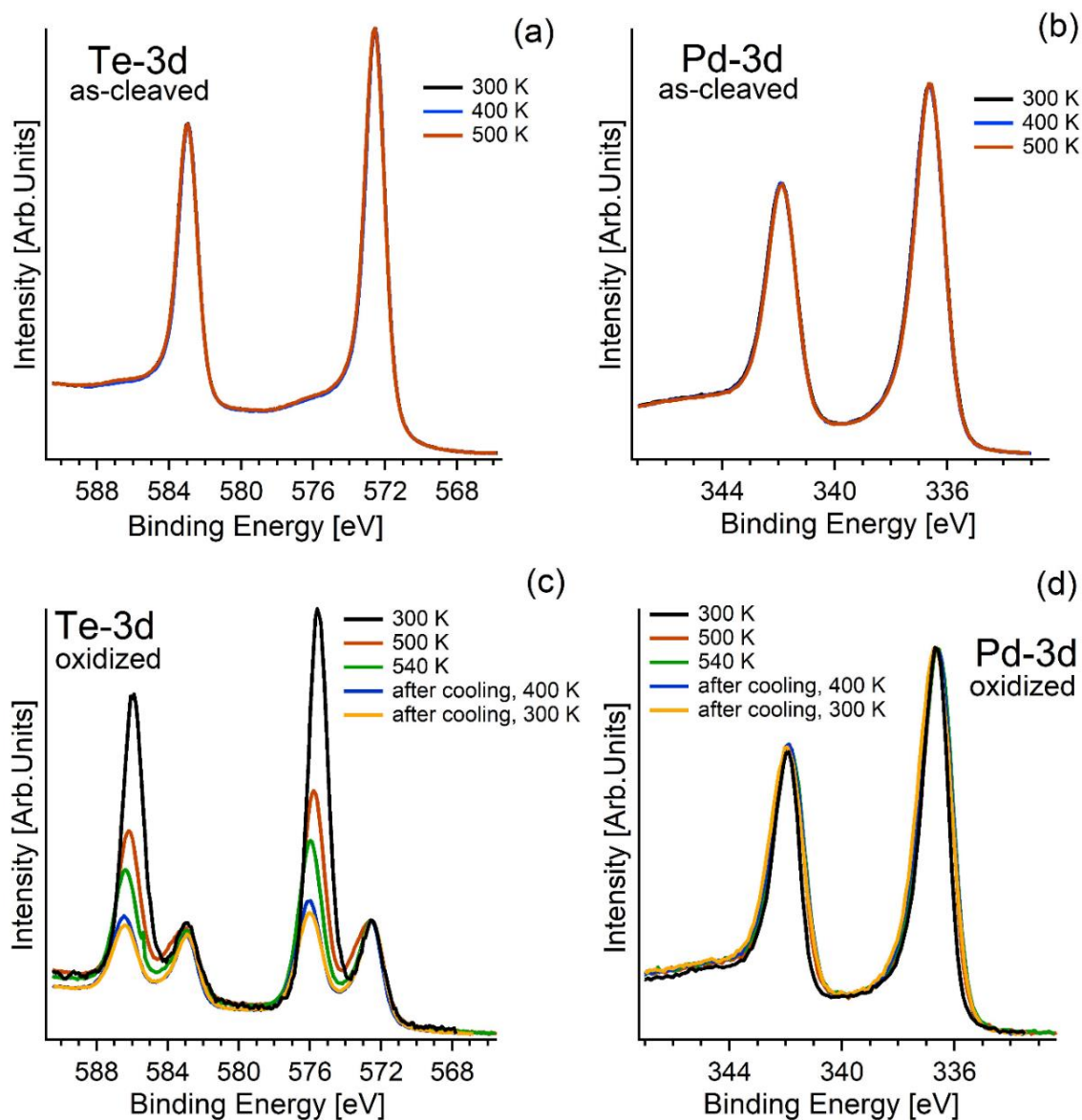


Figure 2.11: Pd-3d and Te-3d core levels taken for (a) the pristine PdTe₂ surface and (b) oxidized PdTe₂. Core-level spectra were acquired at different heating/cooling temperatures. The photon energy is 800 eV.

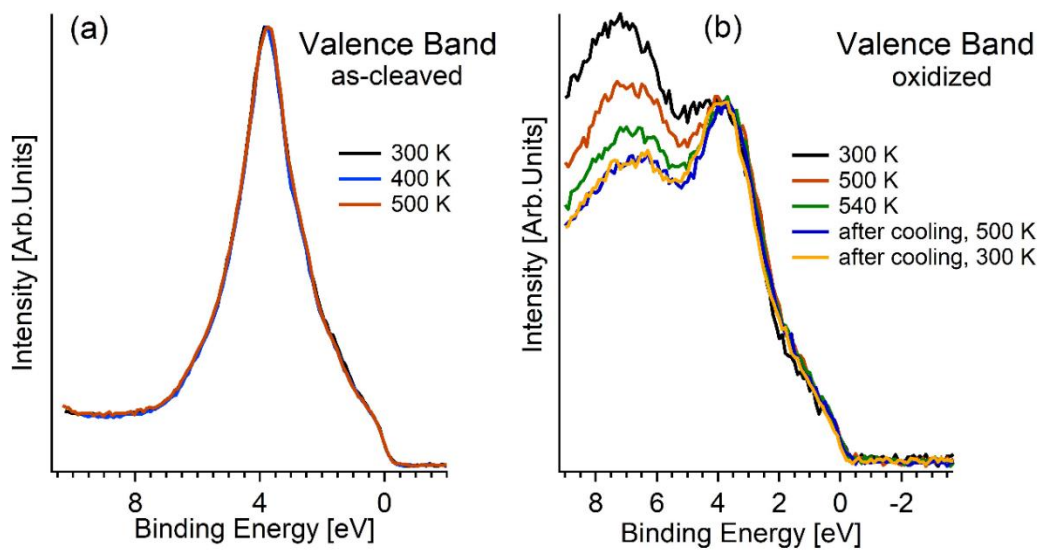


Figure 2.12: Valence-band spectra normalized to the Fermi edge for (a) as-cleaved and (b) oxidized PdTe₂. The photon energy is 400 eV.

The thermal stability of PdTe₂ is further verified by the thermal gravimetric analysis (TGA). The weight change is negligible in the TGA curve up to 680 K (Figure 2.13) and, correspondingly, the differential thermal gravimetry (DTG) curve in inert atmosphere is flat. These evidences point to a nearly zero thermal expansion coefficient for PdTe₂, as previously reported for other layered materials ^[95].

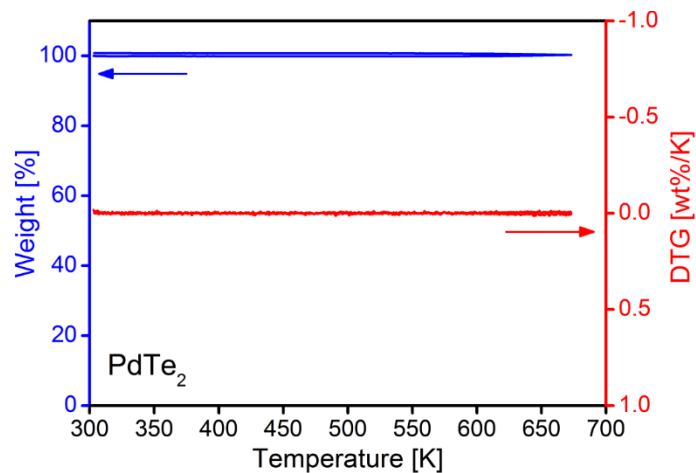


Figure 2.13: TGA (blue) and DTG (red) curves for PdTe₂ in the 300-680 K range, measured in an inert atmosphere (N₂).

Conclusions

In conclusion it is demonstrated that bulk NiTe₂ and PdTe₂ are ambient-stable materials with diverse applications. These materials are stable in air, except the formation of a sub-nanometric TeO₂ skin in surfaces exposed to air. Passivation is reached in less than 30 minutes and no substantial changes are observed even after air exposure in a timescale extended up to one year. Their surfaces are inert toward H₂O and CO, enabling the possibility to fabricate CO-tolerant electrodes for electrocatalysis that would be stable in an aqueous environment. We have also highlighted the impact of Te vacancies on surface oxidation. Therefore, the growth of high-quality single crystals with minimized Te vacancies is crucial to favor the technological exploitation of this novel class of transition-metal dichalcogenide hosting type-II Dirac fermions. It has also been shown that undefected PdTe₂ is thermally stable in the temperature range usually employed for most applications (even above 500 K). Conversely, surface TeO₂ phases are thermally unstable, due to temperature-induced reduction, which also implies changes in the electronic properties.

References

1. Wang QH, Kalantar-Zadeh K, Kis A, Coleman JN, Strano MS. Electronics and optoelectronics of two-dimensional transition metal dichalcogenides. *Nat Nanotech.* 2012; **7** (11), 699-712.
2. Guo Z, et al. Controllable growth of large-area atomically thin ReS₂ films and their thickness-dependent optoelectronic properties. *Appl Phys Lett.* 2019; **114** (15), 153102.
3. Zeng LH, et al. Controlled Synthesis of 2D Palladium Diselenide for Sensitive Photodetector Applications. *Adv Funct Mater.* 2019; **29** (1), 1806878.
4. Witomska S, Leydecker T, Ciesielski A, Samorì P. Production and Patterning of Liquid Phase-Exfoliated 2D Sheets for Applications in Optoelectronics. *Adv Funct Mater.* 2019; **29** (22), 1901126.
5. Long M, Wang P, Fang H, Hu W. Progress, Challenges, and Opportunities for 2D Material Based Photodetectors. *Adv Funct Mater.* 2019; **29** (19), 1803807.
6. Luo LB, Wang D, Xie C, Hu JG, Zhao XY, Liang FX. PdSe₂ Multilayer on Germanium Nanocones Array with Light Trapping Effect for Sensitive Infrared Photodetector and Image Sensing Application. *Adv Funct Mater.* 2019; **29** (22), 1900849.
7. Noubé UN, Gréboval C, Livache C, Brule T, Doudin B, Ouerghi A, Lhuillier E, Dayen JF. Ionic Glass-Gated 2D Material-Based Phototransistor: MoSe₂ over LaF₃ as Case Study. *Adv Funct Mater.* 2019, doi:10.1002/adfm.201902723.

8. Qin JK, et al. Epitaxial Growth of 1D Atomic Chain Based Se Nanoplates on Monolayer ReS₂ for High-Performance Photodetectors. *Adv Funct Mater.* 2018; **28** (48), 1806254.
9. Sun B, Wang Z, Liu Z, Tan X, Liu X, Shi T, Zhou J, Liao G. Tailoring of Silver Nanocubes with Optimized Localized Surface Plasmon in a Gap Mode for a Flexible MoS₂ Photodetector. *Adv Funct Mater.* 2019; **29** (26), 1900541.
10. Zeng LH, et al. Controlled Synthesis of 2D Palladium Diselenide for Sensitive Photodetector Applications. *Adv Funct Mater.* 2019; **29** (1).
11. Chia X, Pumera M. Layered transition metal dichalcogenide electrochemistry: journey across the periodic table. *Chem Soc Rev.* 2018; **47** (15), 5602-13.
12. Zhuang P, et al. Revisiting the Role of Active Sites for Hydrogen Evolution Reaction through Precise Defect Adjusting. *Adv Funct Mater.* 2019, doi:10.1002/adfm.201901290.
13. Kim S, Wang H, Lee YM. 2D Nanosheets and Their Composite Membranes for Water, Gas, and Ion Separation. *Angew Chem.* 2019, doi:10.1002/anie.201814349.
14. Shen J, et al. 2D MXene Nanofilms with Tunable Gas Transport Channels. *Adv Funct Mater.* 2018; **28** (31).
15. Li W, Yang Y, Weber JK, Zhang G, Zhou R. Tunable, Strain-Controlled Nanoporous MoS₂ Filter for Water Desalination. *ACS Nano.* 2016; **10** (2), 1829–35.
16. Zhang H, Cheng HM, Ye P. 2D nanomaterials: Beyond graphene and transition metal dichalcogenides. *Chem Soc Rev.* 2018; **47** (16), 6009-12.
17. Sethulakshmi N, Mishra A, Ajayan PM, Kawazoe Y, Roy AK, Singh AK, Tiwary CS. Magnetism in two-dimensional materials beyond graphene. *Mater Today.* 2019; **27**, 107-22.
18. Deng S, Sumant AV, Berry V. Strain engineering in two-dimensional nanomaterials beyond graphene. *Nano Today.* 2018; **22**, 14-35.
19. Liu Y, Duan X, Huang Y, Duan X. Two-dimensional transistors beyond graphene and TMDCs. *Chem Soc Rev.* 2018; **47** (16), 6388-409.
20. Zeng Z, et al. Controlled Vapor Growth and Nonlinear Optical Applications of Large-Area 3R Phase WS₂ and WSe₂ Atomic Layers. *Adv Funct Mater.* 2019; **29** (11), 1806874.
21. Zang X, et al. Metallo-Hydrogel-Assisted Synthesis and Direct Writing of Transition Metal Dichalcogenides. *Adv Funct Mater.* 2019; **29** (27), 1807612.
22. Zafar A, Zafar Z, Zhao W, Jiang J, Zhang Y, Chen Y, Lu J, Ni Z. Sulfur-Mastery: Precise Synthesis of 2D Transition Metal Dichalcogenides. *Adv Funct Mater.* 2019; **29** (27), 1809261.
23. Sang X, Li X, Puretzky AA, Geohegan DB, Xiao K, Unocic RR. Atomic Insight into Thermolysis-Driven Growth of 2D MoS₂. *Adv Funct Mater.* 2019, doi:10.1002/adfm.201902149.
24. Jing X, Illarionov Y, Yalon E, Zhou P, Grasser T, Shi Y, Lanza M. Engineering Field Effect Transistors with 2D Semiconducting Channels: Status and Prospects. *Adv Funct Mater.* 2019, doi:10.1002/adfm.201901971.
25. Jin H, Hu Z, Li T, Huang L, Wan J, Xue G, Zhou J. Mass Production of High-Quality Transition Metal Dichalcogenides Nanosheets via a Molten Salt Method. *Adv Funct Mater.* 2019, doi:10.1002/adfm.201900649.
26. Higgins TM, et al. Electrolyte-Gated n-Type Transistors Produced from Aqueous Inks of WS₂ Nanosheets. *Adv Funct Mater.* 2019; **29** (4), 1804387.
27. Feng H, et al. Role of Charge Density Wave in Monatomic Assembly in Transition Metal Dichalcogenides. *Adv Funct Mater.* 2019; **29** (15), 1900367.
28. Wang F, et al. 2D library beyond graphene and transition metal dichalcogenides: A focus on photodetection. *Chem Soc Rev.* 2018; **47** (16), 6296-341.
29. Soluyanov AA, Gresch D, Wang Z, Wu Q, Troyer M, Dai X, Bernevig BA. Type-II Weyl semimetals. *Nature.* 2015; **527** (7579), 495-8.
30. Yan M, et al. Lorentz-violating type-II Dirac fermions in transition metal dichalcogenide PtTe₂. *Nature Communications.* 2017; **8** (1), 257.
31. Politano A, Chiarello G, Ghosh B, Sadhukhan K, Kuo C-N, Lue CS, Pellegrini V, Agarwal

- A. 3D Dirac Plasmons in the Type-II Dirac Semimetal PtTe₂. *Phys Rev Lett*. 2018; **121** (8), 086804.
32. Noh H-J, Jeong J, Cho E-J, Kim K, Min B, Park B-G. Experimental Realization of Type-II Dirac Fermions in a PdTe₂ Superconductor. *Phys Rev Lett*. 2017; **119** (1), 016401.
33. Clark OJ, et al. Fermiology and Superconductivity of Topological Surface States in PdTe₂. *Phys Rev Lett*. 2018; **120** (15), 156401.
34. Xu Y, Cao H, Xue Y, Li B, Cai W. Liquid-Phase exfoliation of graphene: An overview on exfoliation media, techniques, and challenges. *Nanomaterials*. 2018; **8** (11), 942.
35. Thakur R, VahidMohammadi A, Moncada J, Adams WR, Chi M, Tatarchuk B, Beidaghi M, Carrero CA. Insights into the thermal and chemical stability of multilayered V₂CT_x MXene. *Nanoscale*. 2019; **11** (22), 10716-26.
36. Thakur R, VahidMohammadi A, Moncada J, Adams WR, Chi M, Tatarchuk B, Beidaghi M, Carrero CA. Insights into the thermal and chemical stability of multilayered V₂CT_x MXene. *Nanoscale*. 2019; **11** (22), 10716-26.
37. Liu X, Wood JD, Chen K-S, Cho E, Hersam MC. In situ thermal decomposition of exfoliated two-dimensional black phosphorus. *J Phys Chem Lett*. 2015; **6** (5), 773-8.
38. Seredych M, et al. High-Temperature Behavior and Surface Chemistry of Carbide MXenes Studied by Thermal Analysis. *Chem Mater*. 2019; **31** (9), 3324-32.
39. Politano A, Vitiello MS, Viti L, Boukhvalov DW, Chiarello G. The role of surface chemical reactivity in the stability of electronic nanodevices based on two-dimensional materials "beyond graphene" and topological insulators. *FlatChem*. 2017; **1**, 60-4.
40. Zhou W, et al. Intrinsic structural defects in monolayer molybdenum disulfide. *Nano Lett*. 2013; **13** (6), 2615-22.
41. Island JO, Steele GA, van der Zant HSJ, Castellanos-Gomez A. Environmental instability of few-layer black phosphorus. *2D Mater*. 2015; **2** (1), 011002.
42. Han X, Han J, Liu C, Sun J. Promise and Challenge of Phosphorus in Science, Technology, and Application. *Adv Funct Mater*. 2018; **28** (45), 1803471.
43. Longo RC, et al. Intrinsic air stability mechanisms of two-dimensional transition metal dichalcogenide surfaces: basal versus edge oxidation. *2D Mater*. 2017; **4** (2), 025050.
44. Gao J, et al. Surface Reconstruction, Oxidation Mechanism, and Stability of Cd₃As₂. *Adv Funct Mater*. 2019; **29**, 1900965.
45. Politano A, Chiarello G, Kuo C-N, Lue CS, Edla R, Torelli P, Pellegrini V, Boukhvalov DW. Tailoring the Surface Chemical Reactivity of Transition-Metal Dichalcogenide PtTe₂ Crystals. *Adv Funct Mater*. 2018; **28** (15), 1706504.
46. Tang W, Politano A, Guo C, Guo W, Liu C, Wang L, Chen X, Lu W. Ultrasensitive Room-Temperature Terahertz Direct Detection Based on a Bismuth Selenide Topological Insulator. *Adv Funct Mater*. 2018; **28** (31), 1801786.
47. Chhowalla M, Shin HS, Eda G, Li L-J, Loh KP, Zhang H. The chemistry of two-dimensional layered transition metal dichalcogenide nanosheets. *Nature Chem*. 2013; **5** (4), 263-75.
48. Yao Q, Zhang L, Bampoulis P, Zandvliet HJ. Nanoscale investigation of defects and oxidation of HfSe₂. *The Journal of Physical Chemistry C*. 2018; **122** (44), 25498-505.
49. Das SR, Wakabayashi K, Yamamoto M, Tsukagoshi K, Dutta S. Layer-by-Layer Oxidation Induced Electronic Properties in Transition-Metal Dichalcogenides. *J Phys Chem C*. 2018; **122** (29), 17001-7.
50. Afanasiev P, Lorentz C. Oxidation of nanodispersed MoS₂ in ambient air: the products and the mechanistic steps. *The Journal of Physical Chemistry C*. 2019; **123** (12), 7486-94.
51. Zhou P, et al. Fabrication of Two-Dimensional Lateral Heterostructures of WS₂/WO₃·H₂O Through Selective Oxidation of Monolayer WS₂. *Angew Chem*. 2015; **54** (50), 15226-30.
52. Liu H, Han N, Zhao J. Atomistic insight into the oxidation of monolayer transition metal dichalcogenides: from structures to electronic properties. *RSC Adv*. 2015; **5** (23), 17572-81.
53. Li Z, Yang S, Dhall R, Kosmowska E, Shi H, Chatzakis I, Cronin SB. Layer control of WSe₂

- via selective surface layer oxidation. *ACS Nano*. 2016; **10** (7), 6836-42.
54. Yamamoto M, Dutta S, Aikawa S, Nakaharai S, Wakabayashi K, Fuhrer MS, Ueno K, Tsukagoshi K. Self-limiting layer-by-layer oxidation of atomically thin WSe₂. *Nano Lett*. 2015; **15** (3), 2067-73.
 55. Dreike P, Fleetwood D, King D, Sprauer D, Zipperian T. An overview of high-temperature electronic device technologies and potential applications. *IEEE Transactions on Components, Packaging, and Manufacturing Technology: Part A*. 1994; **17** (4), 594-609.
 56. Drioli E, Ali A, Macedonio F. Membrane distillation: Recent developments and perspectives. *Desalination*. 2015; **356**, 56-84.
 57. Macedonio F, Politano A, Drioli E, Gugliuzza A. Bi₂Se₃-assisted membrane crystallization. *Mater Horiz*. 2018; **5** (5), 912-9.
 58. Gayner C, Kar KK. Recent advances in thermoelectric materials. *Prog Mater Sci*. 2016; **83**, 330-82.
 59. Han P, Adler ER, Liu Y, St Marie L, El Fatimy A, Melis S, Van Keuren E, Barbara P. Ambient effects on photogating in MoS₂ photodetectors. *Nanotechnology*. 2019; **30** (28), 284004.
 60. Özçelik VO, Gurel HH, Ciraci S. Self-healing of vacancy defects in single-layer graphene and silicene. *Phys Rev B*. 2013; **88** (4), 045440.
 61. Donarelli M, Bisti F, Perrozzi F, Ottaviano L. Tunable sulfur desorption in exfoliated MoS₂ by means of thermal annealing in ultra-high vacuum. *Chem Phys Lett*. 2013; **588**, 198-202.
 62. Lan Y-S, Chen X-R, Hu C-E, Cheng Y, Chen Q-F. Penta-PdX₂ (X= S, Se, Te) monolayer: a promising anisotropic thermoelectric material. *J Mater Chem A*. 2019; **7**, 11134-42.
 63. Goldsmid H. Bismuth telluride and its alloys as materials for thermoelectric generation. *Materials*. 2014; **7** (4), 2577-92.
 64. Bahramy MS, et al. Ubiquitous formation of bulk Dirac cones and topological surface states from a single orbital manifold in transition-metal dichalcogenides. *Nat Mater*. 2018; **17** (1), 21-8.
 65. Voerman JA, de Boer JC, Hashimoto T, Huang Y, Li C, Brinkman A. Dominant s-wave superconducting gap in PdTe₂ observed by tunneling spectroscopy on side junctions. *Phys Rev B*. 2019; **99** (1), 014510.
 66. Kjekshus A, Pearson W. Constitution and magnetic and electrical properties of palladium tellurides (PdTe-PdTe₂). *Can J Phys*. 1965; **43** (3), 438-49.
 67. Politano A, Chiarello G. Vibrational investigation of catalyst surfaces: change of the adsorption site of CO molecules upon coadsorption. *The Journal of Physical Chemistry C*. 2011; **115** (28), 13541-53.
 68. Li Q, He R, Gao J-A, Jensen JO, Bjerrum NJ. The CO poisoning effect in PEMFCs operational at temperatures up to 200 C. *Journal of the Electrochemical Society*. 2003; **150** (12), A1599-A605.
 69. Giannozzi P, et al. QUANTUM ESPRESSO: a modular and open-source software project for quantum simulations of materials. *Journal of Physics: Condensed Matter*. 2009; **21** (39), 395502.
 70. Monkhorst HJ, Pack JD. Special points for Brillouin-zone integrations. *Phys Rev B*. 1976; **13** (12), 5188-92.
 71. D'Olimpio G, et al. PdTe₂ Transition-Metal Dichalcogenide: Chemical Reactivity, Thermal Stability, and Device Implementation. *Adv Funct Mater*. 2020; **30** (5), 1906556.
 72. Bahl M, Watson R, Irgolic K. X-ray photoemission studies of tellurium and some of its compounds. *The Journal of Chemical Physics*. 1977; **66** (12), 5526-35.
 73. Kidambi PR, et al. Observing graphene grow: catalyst-graphene interactions during scalable graphene growth on polycrystalline copper. *Nano Lett*. 2013; **13** (10), 4769-78.
 74. Schiros T, et al. Structure and bonding of the water-hydroxyl mixed phase on Pt (111). *J Phys Chem C*. 2007; **111** (41), 15003-12.
 75. Fingerle M, Tengeler S, Calvet W, Mayer T, Jaegermann W. Water Interaction with

- Sputter-Deposited Nickel Oxide on n-Si Photoanode: Cryo Photoelectron Spectroscopy on Adsorbed Water in the Frozen Electrolyte Approach. *J Electrochem Soc.* 2018; **165** (4), H3148-H53.
76. Grosvenor A, Kobe B, McIntyre N. Studies of the oxidation of iron by water vapour using X-ray photoelectron spectroscopy and QUASES™. *Surf Sci.* 2004; **572** (2-3), 217-27.
 77. Meeporn K, Chanlek N, Thongbai P. Effects of DC bias on non-ohmic sample-electrode contact and grain boundary responses in giant-permittivity La 1.7 Sr 0.3 Ni 1- x Mg x O 4 ceramics. *RSC Adv.* 2016; **6** (94), 91377-85.
 78. Berchenko N, Vitchev R, Trzyna M, Wojnarowska-Nowak R, Szczerbakow A, Badyła A, Cebulski J, Story T. Surface oxidation of SnTe topological crystalline insulator. *Appl Surf Sci.* 2018; **452**, 134-40.
 79. Galca AC, Sava F, Simandan ID, Bucur C, Dumitru V, Porosnicu C, Mihai C, Velea A. Structural and optical properties of optimized amorphous GeTe films for memory applications. *Journal of Non-Crystalline Solids.* 2018; **499**, 1-7.
 80. Politano A, Formoso V, Chiarello G. Temperature effects on alkali-promoted CO dissociation on Ni (1 1 1). *Surface science.* 2008; **602** (12), 2096-100.
 81. Politano A, Chiarello G. The formation of HOCO in the coadsorption of water and carbon monoxide on Pt 3 Ni (111). *RSC Adv.* 2014; **4** (86), 45641-6.
 82. Baro A, Ibach H. New study of CO adsorption at low temperature (90 K) on Pt (111) by EELS. *The Journal of chemical physics.* 1979; **71** (12), 4812-6.
 83. Bartos B, Freund H-J, Kuhlbeck H, Neumann M, Lindner H, Müller K. Adsorption and reaction of CO₂ and CO₂/O CO-adsorption on Ni (110): Angle resolved photoemission (ARUPS) and electron energy loss (HREELS) studies. *Surface Science.* 1987; **179** (1), 59-89.
 84. Jacobi K, Bertolo M, Hansen W. HREELS investigation of physisorbed molecules on single- crystalline surfaces through dipole and resonant electron-scattering mechanism. *Journal of Electron Spectroscopy and Related Phenomena.* 1990; **54-55**, 529-40.
 85. Alexander MR, Thompson GE, Zhou X, Beamson G, Fairley N. Quantification of oxide film thickness at the surface of aluminium using XPS. *Surface and Interface Analysis.* 2002; **34** (1), 485-9.
 86. Sciortino L, Cicero UL, Magnano E, Piš I, Barbera M, editors. Surface investigation and aluminum oxide estimation on test filters for the ATHENA X-IFU and WFI detectors. *Space Telescopes and Instrumentation 2016: Ultraviolet to Gamma Ray; 2016: International Society for Optics and Photonics.*
 87. Ganguly A, Sharma S, Papakonstantinou P, Hamilton J. Probing the Thermal Deoxygenation of Graphene Oxide Using High-Resolution In Situ X-ray-Based Spectroscopies. *J Phys Chem C.* 2011; **115** (34), 17009-19.
 88. Kerber S, Bruckner J, Wozniak K, Seal S, Hardcastle S, Barr T. The nature of hydrogen in x-ray photoelectron spectroscopy: General patterns from hydroxides to hydrogen bonding. *J Vac Sci Technol A.* 1996; **14** (3), 1314-20.
 89. Ziletti A, Carvalho A, Trevisanutto PE, Campbell DK, Coker DF, Castro Neto AH. Phosphorene oxides: Bandgap engineering of phosphorene by oxidation. *Phys Rev B.* 2015; **91** (8), 085407.
 90. Fang Y, Armin A, Meredith P, Huang J. Accurate characterization of next-generation thin-film photodetectors. *Nat Photonics.* 2019; **13**, 1-4.
 91. Spectrum for Terrestrial 5G Networks: Licensing Developments: Global Mobile Supplier Association; 2018.
 92. Wang H, et al. Black Phosphorus Radio-Frequency Transistors. *Nano Lett.* 2014; **14** (11), 6424-9.
 93. Fiori G, Bonaccorso F, Iannaccone G, Palacios T, Neumaier D, Seabaugh A, Banerjee SK, Colombo L. Electronics based on two-dimensional materials. *Nat Nanotechnol.* 2014; **9** (10), 768-79.

94. Krasnozhon D, Lembke D, Nyffeler C, Leblebici Y, Kis A. MoS₂ transistors operating at gigahertz frequencies. *Nano Lett.* 2014; **14** (10), 5905-11.
95. Anemone G, Al Taleb A, Castellanos-Gomez A, Fariás D. Experimental determination of thermal expansion of natural MoS₂. *2D Mater.* 2018; **5** (3), 035015.

GaSe and SnSe₂: layered semiconductors

Layered semiconductors offer application capabilities often complementary to those of graphene^[1-6]. Specifically, the presence of a bulk band gap, absent in graphene^[7], makes them suitable candidate for optoelectronic devices^[8-11], gas sensing^[12-15] and photocatalysis^[16, 17]. Among semiconductors with weak interlayer van der Waals interactions^[18], several materials show serious drawbacks, limiting their technological potential. Specifically, MoS₂ and WS₂ display intrinsic electron mobility as low as some tens of cm² V⁻¹ s⁻¹ at T=300 K^[19]; black phosphorus rapidly degrades in air due to surface oxidation^[20, 21]; and PdSe₂^[22] has a limited commercial potential, due to the constantly growing price of Pd (2000-2400 \$/oz), nearly doubled in 2019-2020.

Tin diselenide (SnSe₂)^[23-25] and III-VI semiconductors, such as GaSe^[26-33] and InSe^[34-40], have attracted significant attention. SnSe₂ shows its high intrinsic electron mobility (462.6 cm² V⁻¹ s⁻¹ at T=300 K^[41]) and ultralow thermal conductivity (3.82 W m⁻¹ K⁻¹^[41]). It displays pressure-induced periodic lattice distortion and, moreover, it enables novel device functionalities being a phase change memory material, i.e. its atomic structure can reversibly switch from amorphous to crystalline upon laser heating, with consequent remarkable variations in the optical reflectivity. Owing to these peculiarities, SnSe₂ has high application capabilities in numerous fields, including photocatalysis^[42, 43], superconductivity^[44, 45], Li-^[24, 46, 47] and Na-^[24, 47, 48] ion batteries, photodetection^[49], saturable absorbers for eye-safe lasers^[50], and thermoelectricity^[51-53]. Furthermore, SnSe₂ was used as co-catalyst for hydrogen evolution reaction^[54].

GaSe and InSe have the band-gap energy matching the visible range of the electromagnetic spectrum^[18] and the possibility of room-temperature single-photon emission^[55].

However, all Sn-based chalcogenides and the GaSe undergoes oxidation in ambient air leading to the formation of tin-oxide phases^[56, 57] and Ga₂O₃^[58-66].

Recently, exfoliation of GaSe in nanosheets has been shown to be beneficial for improving the performance of HER^[67] and photoelectrochemical water splitting^[26].

In this chapter, by means of surface sensitive experimental technique and DFT, studies on surface properties of SnSe₂ and GaSe single crystals are reported. For the SnSe₂ the surface properties and its modification in oxidative and humid environments are studied. In the case of GaSe it has been demonstrated that the surface transformation of GaSe in Ga₂O₃ in ambient conditions is the main factor for the enhancement of performances in electrochemistry and photocatalysis.

GaSe a layered semiconductor for catalysis

Introduction

GaSe and InSe exist in nature in four polytypes, with dissimilar stacking sequence of layers^[68, 69]. The most diffuse are hexagonal ϵ -GaSe (space group $P\bar{6}m2$)^[70] and β -InSe (space group $P6_3/mmc$)^[71], exhibiting a Se–Ga(In)–Ga(In)–Se sequence.

Recently, exfoliation of GaSe in nanosheets has been shown to be beneficial for improving the performance of HER^[67] and photoelectrochemical water splitting^[26]. However, GaSe undergoes oxidation in ambient air leading to the formation of Ga₂O₃^[58-66]. Consequently, encapsulation strategies to protect GaSe from environment have been recently devised in order to reduce the impact of oxidation^[27]. Precisely, most researchers reported complete degradation of GaSe flakes with a thickness of 10-50 nm, although time required for oxidation is quite controversial, ranging from 30 minutes^[60] up to some days (4 in Ref.^[72], 5 in Ref.^[73], 8 in Ref.^[27], >14 in Ref.^[74]). On the other hand, Rahaman et al.^[64] reported that

the penetration of the oxidation has a self-limited depth of only three layers after five hours in air. Similarly, for InSe results on oxidation are debated, going from complete oxidation in Ref. [75] up to negligible traces of oxidation even in air-exposed nanosheets in Ref. [76].

Actually, the incomplete picture on physicochemical mechanisms ruling GaSe and InSe oxidation should be attributed to the insufficient surface sensitivity of spectroscopic tools used so far. Indeed, the control of the oxidation status is usually performed by Raman spectroscopy [58, 60], regardless its scarce surface sensitivity, in consideration of its probing depth in the 300-650 nm range [77, 78]. Moreover, the probing depth of X-ray photoelectron spectroscopy (XPS) experiments with conventional X-ray source at 1486.6 eV reaches even ~ 9 nm for Ga-3d and Se-3d core levels. Accordingly, the early steps of oxidation of GaSe- and InSe-based systems, as well as their corresponding impact on surface chemical reactions in electrochemical, photocatalytic and gas-sensing processes, are generally undetected, owing to insufficient surface sensitivity. On the other hand, the use of low-energy photons, available in synchrotron radiation sources, could significantly improve the surface sensitivity [79].

Another important issue is related to the impact of chemical reactivity of Se vacancies [80]. Most single crystals of GaSe and InSe are far from being stoichiometric. Typically, the [Ga]:[Se] ratio ranges from 50.4:49.6 [81] up to 59.1:40.9 [26] even for nominal GaSe samples. Subsequently, the abundant amount of Se-vacancy sites could – at least in principle – play an important role in electrocatalytic and photocatalytic performances reported in Ref. [26] and attributed to the exfoliation in nanosheets.

Precisely, in this section I show that as-exfoliated stoichiometric GaSe single crystal assumes a Ga_2O_3 skin once it is exposed to air. The presence of Se vacancies, as well as exfoliation in nanosheets naturally exhibiting Ga-edge sites, accelerates the oxidation process by $\sim 10^2$ times. The energy barrier for HER and OER is reduced upon surface oxidation, with further decrease around O-vacancy sites. Therefore, contrary to the common view, exfoliation in nanosheets does not improve HER kinetics in consideration of higher surface-to-volume ratio, but rather for the enhancement of oxidation rate, which plays an unexpectedly beneficial role. Accordingly, the self-assembled $\text{Ga}_2\text{O}_3/\text{GaSe}$ heterostructure represents an ideal platform for electrocatalysis.

Methods

Computational methods. See section 2 p. 19. Except for the modelling of the surfaces of GaSe and SnSe₂. For GaSe we used slab of three layers with ABA stacking, while three layers in ABC stacking was adopted for InSe. For reproduce effect of deeper layers of the bulk materials, we performed calculations with fixed lattice parameters. Optimization of the only atomic positions were performed. For the modeling of monolayers of both compounds we performed optimization of lattice parameters and atomic positions. To model Ga₂O₃-skin, we used a slab with thickness of about 1 nm. For the modelling of the surface of SnSe₂, we used a slab of three layers. For make calculations more realistic, we also considered the presence of the Se vacancies in the top layer. The formation of the single vacancy corresponds to SnSe_{1.88} for the outermost surface layer.

Single-crystal growth. Centimeter-scale GaSe single crystals (Figure 3.1c) were grown by modified Bridgman-Stockbarger method using quartz ampoules. Stoichiometric ratios of Ga and Se were put to the ampoule to grow 50 g of GaSe and sealed under a vacuum of 10⁻⁶ mbar. Then, the crucible was placed into a two-zone horizontal furnace. The structural characterization of GaSe was performed using X-ray diffraction using Cu-K α radiation (Bruker D2 Phaser).

InSe crystals were grown by using the Bridgman-Stockbarger method. The grown InSe samples are 10 mm in diameter and about 60 mm in length.

Liquid-phase exfoliation. GaSe and InSe single crystals were exfoliated in liquid phase following the same experimental procedures in Refs. ^[26] and ^[76], respectively.

XPS. Near-ambient pressure XPS experiments were carried out at the Charles University (Prague), while aging experiments were performed with synchrotron-based XPS at the CNR-BACH beamline ^[82] at Elettra Synchtron in Trieste (Italy) to follow air-induced modification of core levels with higher energy resolution. XPS spectra for oxidized GaSe and InSe nanosheets were acquired using Al K α with a VG-Scienta R3000 hemispherical analyzer.

Sn-3d, Ga-3d and In-4d core levels were decomposed into spectral components using Voigt doublet, while In-3d and O-1s core levels were decomposed using single Voigt line shape, including Shirley type background subtraction.

LEEM. LEEM images and EELS measurements were carried out at the soft X-ray beamline Nanospectroscopy at Elettra Synchrotron, Trieste, Italy, using an energy filtered LEEM-PEEM microscopy. The SPELEEM III microscope (Elmitec GmbH) combines laterally resolved XPS with LEEM. In LEEM mode, the microscope probes the specimen with low-energy electrons, using the elastically backscattered electron beam for imaging. Such a LEEM operation allows surface sensitive real-space imaging with a best spatial resolution of about 10 nm. EELS measurements were acquired at normal incidence, by varying the bias voltage of the electron energy filter, so that it is possible to span the kinetic energy of the inelastically reflected beam reaching the detector, obtaining the EELS spectrum.

Results and discussion

Surface chemical reactivity and ambient stability. GaSe single crystals were grown by modified Bridgman–Stockbarger technique (see Experimental). Their atomic structure and X-ray diffraction (XRD) pattern are shown in Figure 3.1a,b and c, respectively. To evaluate the chemical stability of GaSe, we modelled the energetics of the adsorption and decomposition of most relevant ambient gases (O_2 and H_2O) on its surface (see Table III).

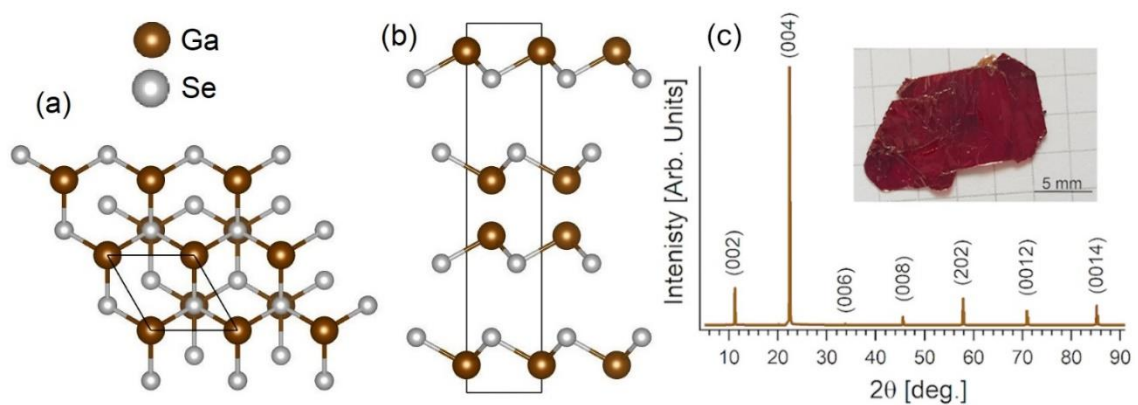


Figure 3.1: (a) Top and (b) side views of the atomic structure of GaSe. Brown and white balls denote Ga and Se atoms, respectively. Panel (c) shows the X-ray diffraction (XRD) pattern of grown single crystals of GaSe, whose photograph is reported in the inset.

The differential Gibbs free energy (ΔG) for adsorption of molecular oxygen

and water on the GaSe surface at room temperature is positive in both cases (+33.7 and +17.9 kJ/mol, respectively), thus indicating that their adsorption is energetically unfavorable. However, the presence of Se vacancies has a strong impact on surface chemical reactivity. Specifically, stable adsorption of both O₂ and H₂O is energetically favorable at Se-vacancy sites at room temperature ($\Delta G = -156.7$ and -109.0 kJ/mol, respectively). Oxygen decomposition on defective GaSe is also energetically favorable, as indicated by the decomposition energy ΔH_{dec} for O₂ on GaSe_{0.94} (-182.6 kJ/mol). Instead, the decomposition energy for water on GaSe_{0.94} at Se-vacancy sites is rather small ($\Delta H_{\text{dec}} = -2.1$ kJ/mol). Concerning InSe-based systems, physisorption and further decomposition of molecular oxygen is an exothermic process, with ΔG values of -23.5 and -197.8 kJ/mol for adsorption on InSe and InSe_{0.94} surfaces, whereas water adsorption is unfavorable at room temperature (Table III).

Adsorption of water molecules on monolayer GaSe and InSe is less favorable with respect to the case of their bulk counterparts. Definitely, only adsorption of water at Se-vacancy sites in InSe is energetically favorable ($\Delta G = -60.0$ kJ/mol).

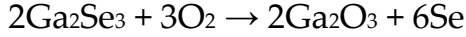
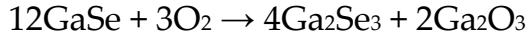
Table III: Differential enthalpy (ΔH_{ads}), differential Gibbs free energy (ΔG) of physisorption and differential enthalpy of decomposition (ΔH_{dec}) calculated for selected species on defect-free (001) surfaces of GaSe, InSe and in the vicinity of Se vacancies on the same surfaces.

thickness	adsorbed species	substrate	physisorption		decomposition
			ΔH_{ads} [kJ/mol]	ΔG [kJ/mol]	ΔH_{dec} [kJ/mol]
bulk	O ₂	GaSe	+21.4	+33.7	-41.9
		GaSe _{0.94}	-168.0	-156.7	-182.6
		InSe	-34.6	-23.5	-320.2
		InSe _{0.94}	-209.1	-197.8	-170.5
	H ₂ O	GaSe	-13.4	+17.9	+258.6
		GaSe _{0.94}	-140.3	-109.0	-2.1
		InSe	-16.5	+14.8	+204.0
		InSe _{0.94}	-20.5	+10.8	+96.8
monolayer	O ₂	GaSe	+226.4	+237.7	+154.6

	GaSe _{0.94}	-105.6	-94.2	-124.7
	InSe	+68.0	+78.3	-56.9
	InSe _{0.94}	-154.5	-143.2	-123.2
	GaSe	+24.6	+55.9	+130.6
H ₂ O	GaSe _{0.94}	-30.2	+0.9	+41.4
	InSe	-13.4	+17.7	+301.5
	InSe _{0.94}	-91.3	-60.0	+171.5

To model surface oxidation, we considered one-side oxidation of whole surface of GaSe with further formation of the oxide layer on the surface through two reaction paths, involving as intermediate phases (i) Ga₂Se₃ (consistently with Refs. [60, 64]) and (ii) GaSe_xO.

Specifically, the reaction path involving Ga₂Se₃ intermediate is modelled as a two-step process, starting from stoichiometric GaSe:



Both steps are exothermic with energy -6.9 kJ/GaSe and -98.8 kJ/Ga₂Se₃, respectively.

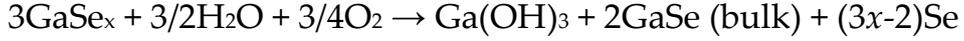
On the other hand, the GaSe_xO phase is formed following the reaction path:



Both reactions are energetically favorable for both GaSe (-53.7 and -169.9 kJ/mol, respectively) and defective GaSe (-102.1 and -145.2 kJ/mol for the case of GaSe_{0.94}, respectively) see Table IV. The same model can be applied for InSe (Table IV). Excess Se atoms could form a bulk Se phase or, alternatively, they can migrate in the subsurface area, with subsequent healing of defects. However, the second scenario is the most energetically favorable (-313.94 and -257.26 kJ/Se for GaSe and InSe respectively).

Notably, we find that the adsorption and decomposition of water on Se-vacancy sites in defective gallium selenide (GaSe_x) also provides oxidation,

although the process has an intermediate step:



This reaction path involves decomposition of water with formation of $-\text{H}$ and $-\text{OH}$ on GaSe_x with further formation of gallium trihydroxide with a small energy barrier (+14.5 kJ/mol for $\text{GaSe}_{0.94}$). However, the energy gain related to further decomposition to trioxide and water is very high (-544 kJ/mol):



Table IV: Differential enthalpy (kJ/formula unit) of the two-step process of $\text{Ga}(\text{In})_2\text{O}_3$ skin formation.

Substrate	Process	
	$\text{Ga}(\text{In})\text{Se}_x + 1/2\text{O}_2 \rightarrow \text{Ga}(\text{In})\text{Se}_x\text{O}$	$\text{Ga}(\text{In})\text{Se}_x\text{O} \rightarrow \text{Ga}(\text{In})_2\text{O}_3 \text{ (skin)} + \text{Ga}(\text{In})\text{Se (bulk)}$
GaSe	-53.7	-169.9
$\text{GaSe}_{0.94}$	-102.1	-145.2
InSe	-19.2	-133.2
$\text{InSe}_{0.94}$	-16.9	-134.3

Moreover, we assessed the possibility of water intercalation by vibrational experiments and theory. Vibrational experiments by HREELS indicate that the GaSe surface is inert toward both oxygen and water molecules at room temperature, in excellent agreement with theoretical predictions in Table III. As a matter of fact, the vibrational spectrum remains featureless even after doses as high as 10^{10} L (1 L= 10^{-6} Torr·s), for both the cases of O_2 and H_2O (Figure 3.2). Considering the high surface sensitivity of HREELS (practically coinciding with the outermost surface layer only ^[83]), one can affirm that absence of vibrational bands ensures that any chemisorbed species would have a coverage less than 10^{-3} ML. Especially, Ga_2O_3 -derived Fuchs-Kliewer phonons would appear at loss energies around 455 and 785 cm^{-1} , as in a previous HREELS study on β - Ga_2O_3 ^[84].

Different results are achieved for the parental compound InSe. Definitely, the

vibrational spectrum acquired after having dosed 10^5 L ($1 \text{ L}=10^{-6}$ Torr-s) of H_2O at room temperature on the pristine InSe surface displays OH-In and O-H stretching vibrations at 550 ^[85] and 3654 ^[86] cm^{-1} .

The emergence of H_2O -derived vibrational features on InSe is apparently incompatible with the positive differential Gibbs free energy for water adsorption on both pristine and defective InSe-based systems. However, vibrational features can also be related to intercalated water molecules in the subsurface region.

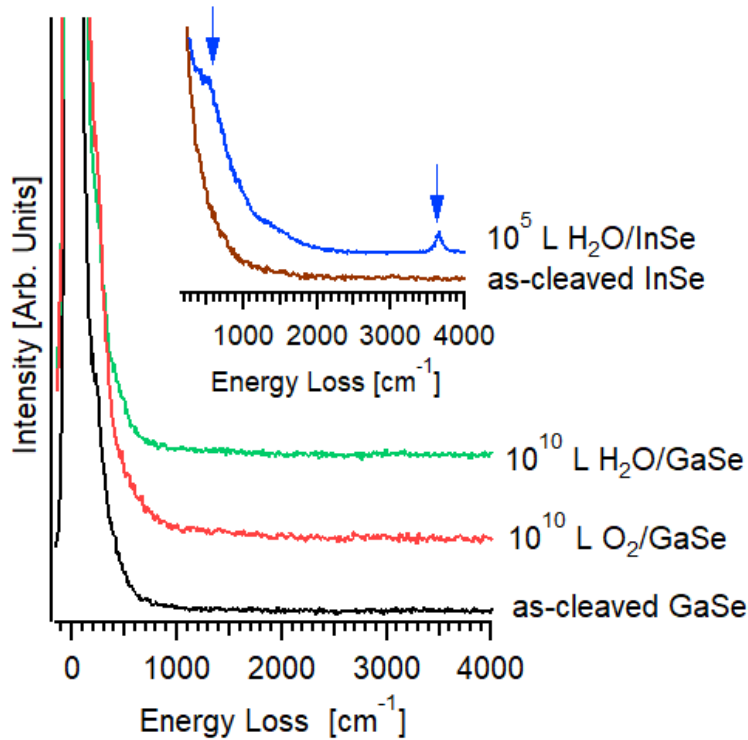


Figure 3.2: Vibrational spectra of as-cleaved GaSe and of the same surface modified by the exposure to 10^{10} L of O_2 and H_2O at room temperature. The inset reports vibrational spectra for pristine and H_2O -dosed (10^5 L) InSe.

To explore the possibility of water intercalation, we calculated the binding energies (BEs) per formula unit for trilayers of both GaSe and InSe. Theoretical results in Table V demonstrate that interlayer BE of InSe is weaker with respect to the case of GaSe. The presence of Se vacancies induces a weakening of interlayer bonding, especially relevant for the case of InSe for all allotropes, with a reduction by 64% for just 6% of Se vacancies ($\text{InSe}_{0.94}$). The free energy of water intercalation at room temperature is -138.9 kJ/mol for $\text{GaSe}_{0.94}$ and -80.5 kJ/mol for $\text{InSe}_{0.94}$. Interlayer bonds can be broken by the intercalation of a single water

molecule in an area of about 3 and 7 nm² for GaSe_{0.94} and InSe_{0.94}, respectively. Hence, reversible intercalation of water underneath sub-surface layers of InSe_{0.94} is rather likely.

Table V: Binding energies (in kJ/formula unit) between the layers in trilayers of GaSe, GaSe_{0.94}, InSe and InSe_{0.94}.

Substrate/Structure	ϵ	γ	β
GaSe	13.97	14.04	13.28
GaSe _{0.94}	9.96	10.74	9.43
InSe	9.81	10.71	9.01
InSe _{0.94}	3.37	3.39	3.29

Congruently with positive values of ΔG for adsorption of ambient gases on defect-free GaSe predicted by our model (Table III), XPS measurements performed in near-ambient pressure conditions (NAP-XPS) did not evidence any modification of Ga-3d and Se-3d core levels after dosing 10¹⁰ L (1 L=10⁻⁶ Torr·s) of O₂ and H₂O at room temperature on GaSe (Figure 3.3a,b). The binding energy (BE) of Ga-3d_{5/2} and Se-3d_{5/2} is 19.2 and 54.1 eV, respectively, consistently with previous reports [62, 87-91].

To assess the role of Se vacancies, we modified the pristine GaSe surface by Ar-ion sputtering introducing a density of Se vacancies of $\sim 10^{16}$ cm⁻² (as estimated by quantitative XPS [92, 93]). The sputtering was performed at room temperature, using Ar-ions with an impinging energy of 2.5 keV and P_{Ar} = 10⁻⁵ mbar. In the defective sample, we observe two new components in Ga-3d, assigned to Ga(0) (BE = 18.6 eV [62], 37% of the total area of Ga-3d) and Ga₂Se₃ species (BE = 19.8 eV [89], 27% of the total area), respectively. Correspondingly, the implantation of Se vacancies introduces a new component in Se-3d_{5/2} at BE 54.6 eV, which corresponds to both Ga₂Se₃ and GaSe_xO species [94].

Upon exposure of 10¹⁰ L of O₂, the relative intensity of Ga(0) and Ga₂Se₃ components decreased their spectral area, while a novel feature assigned to species on early stage of oxidation (GaSe_xO) and Ga₂O₃ [95] emerged (5% of the total spectra area), with J=5/2 component at BE = 20.4 eV in Ga-3d. Congruently, the O-1s core level, reported in Figure 3.4, shows a component at BE = 530.8 eV

arising from Ga_2O_3 and GaSe_xO [91, 95-98].

In the H_2O -dosed defective sample, the Ga_2O_3 component increased (8% of the total spectra area), due to the partial conversion of Ga_2Se_3 into Ga_2O_3 in humid environment. Correspondingly, the Ga_2O_3 [91, 95-98] component at 530.8 eV in O-1s core level (28% of the total area) appeared together with minor spectral components related to OH groups and H_2O molecules [91, 99, 100] adsorbed on Ga_2O_3 patches (Figure 3.4).

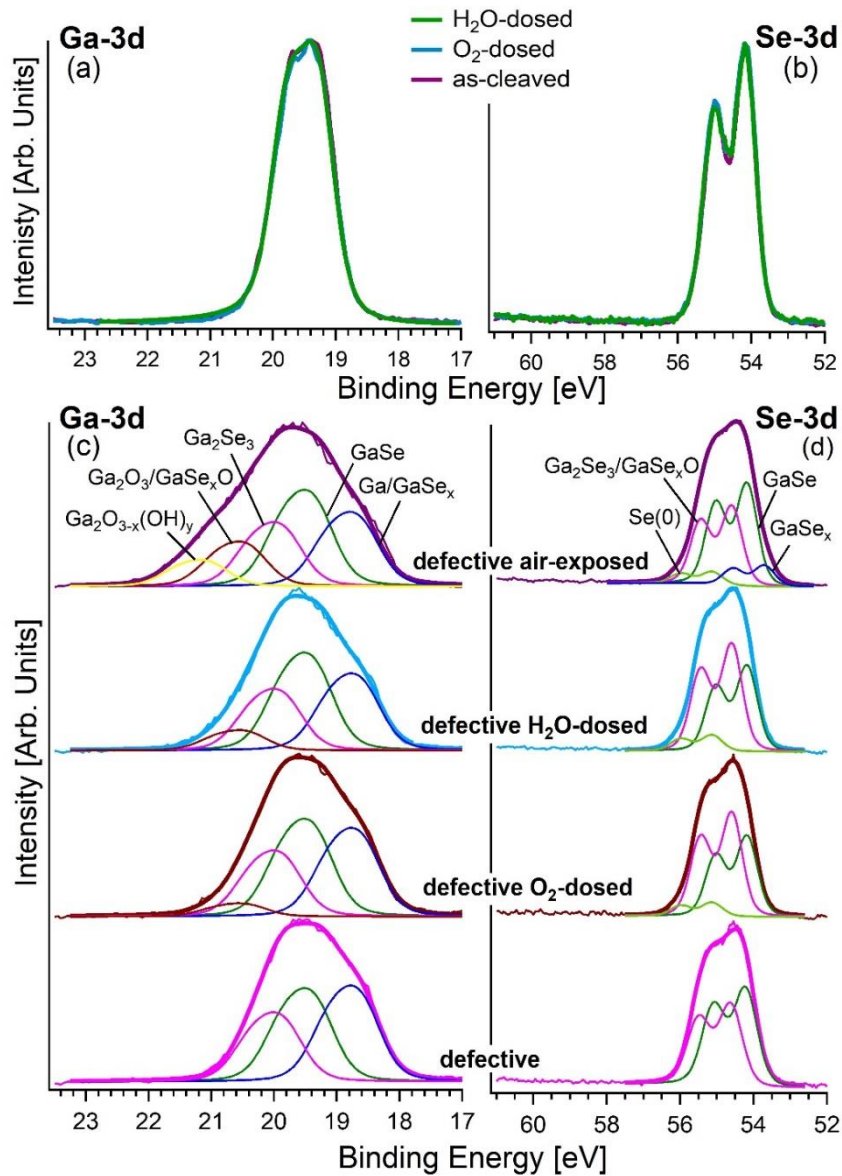


Figure 3.3: (a, c) Ga-3d and (b, d) Se-3d core levels for the (a, b) as-cleaved surface of GaSe and its modification after dosing 10^{10} L O_2 and H_2O at room temperature. Panels (c-d) report the same for GaSe modified by ion sputtering, with a surface density of Se vacancies of 10^{16} cm^{-2} . The defective sample was also exposed to air for one hour. The

photon energy is 1486.6 eV (Al $K\alpha$).

The pristine GaSe surface was also directly exposed to air with the aim to monitor its aging by XPS (Figure 3.5a-b) and to determine the thickness of the gallium-oxide skin formed in the air-exposed sample from the evolution of Ga-3d and Se-3d as a function of exposure time to ambient air.

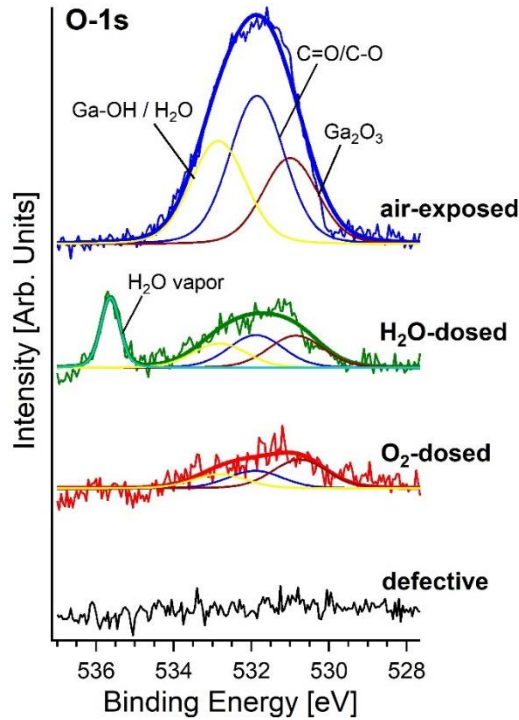


Figure 3.4: O-1s core level for the defective surface of GaSe and for its modification after dosing 10^{10} L of O_2 and H_2O and, moreover, after air exposure. Experiments and exposures were carried out at room temperature. The photon energy is 1486.6 eV (Al $K\alpha$).

Definitely, 10 minutes of air exposure did not induce any change in neither Ga-3d nor Se-3d core levels, while keeping the sample in ambient conditions for longer periods (2 hours) resulted in a new spectral feature with BE 0.5 eV lower than the GaSe component in Ga-3d. This spectral contribution, denoted as $GaSe_x$ in

XPS spectra in Figure 3.5, is associated to the possible creation of surface defects or, alternatively, to intercalation of ambient gases in the subsurface region. Moreover, two new features appeared at BE of 19.8 and 20.4 eV for the $J=5/2$ component, which were ascribed to the formation of Ga_2Se_3 (2% of the total spectral area) and Ga_2O_3 (10.5% of the total spectral area), respectively [60, 64, 101]. The Se 3-d core level was almost unchanged, except for the presence of the Ga_2Se_3 and $GaSe_xO$ component at 54.5 eV (2.5% of the total area), and a new feature, associated to $GaSe_x$, down-shifted by 0.4 eV with respect to the bulk GaSe component. After one day of air exposure, the intensity of Ga_2Se_3 and Ga_2O_3 components increased to 7% and 15%, respectively, owing to the progressive surface oxidation. The thickness of gallium-oxide skin, formed after 1 day in air, is estimated to be ~ 0.2 QL, where QL stands for Ga_2O_3 quintuple layer (O-Ga-O-

Ga-O), with $c = 0.58 \text{ nm}$ [102]. Notably, sharp spots in LEED pattern of the GaSe surface (Figure 3.5c) survived even after 1 day in air, except for their inevitable broadening, due to the onset of GaSe oxidation. After one year in air, the area of the spectral contribution of Ga_2O_3 in Ga-3d core levels increased up to 53% of the total area and a new component associated to mixed oxide-hydroxide $\text{Ga}_2\text{O}_{3-x}(\text{OH})_y$ species (10%) appeared at $\text{BE}=21.0 \text{ eV}$ [103-105]. The corresponding analysis of Se-3d core levels indicates a notable increase of the intensity of the spectral component at $\text{BE } 54.6 \text{ eV}$ and the emergence of a new feature at $\text{BE } 55.2 \text{ eV}$, consistent with the formation of (i) GaSe_xO phases, having the same BE of Ga_2Se_3 , and (ii) atomic Se (0) (24%) [106-108] as byproducts of GaSe and Ga_2Se_3 oxidation via $3\text{GaSe}_x + 3/2\text{O}_2 \rightarrow 3\text{GaSe}_x\text{O} \rightarrow \text{Ga}_2\text{O}_3 + \text{GaSe} + (3x-1)\text{Se}$ and $2\text{Ga}_2\text{Se}_3 + 3\text{O}_2 \rightarrow 2\text{Ga}_2\text{O}_3 + 6\text{Se}$ reactions [91]. Correspondingly, the gallium-oxide skin reaches the thickness of $0.8 \pm 0.1 \text{ nm}$, i.e., $\sim 1.4 \text{ QL}$. Congruently, the analysis of O-1s confirm the oxidation of GaSe and the hydroxylation of Ga_2O_3 surface upon air exposure (Figure 3.6).

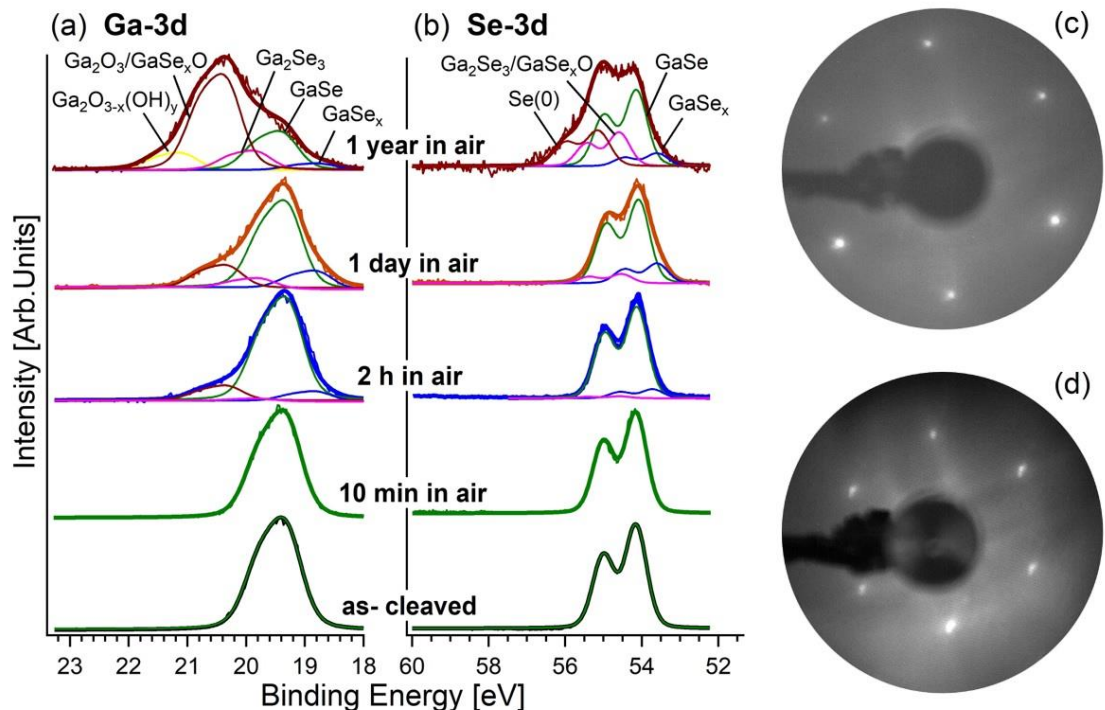


Figure 3.5: (a) Ga-3d and (b) Se-3d core-level spectra collected from GaSe exposed to air for 10 min, 2 hours, 1 day and 1 year. The photon energy is 830 eV. The black curve related to the as-cleaved sample is provided as a reference. Panels (c) and (d) show the LEED pattern for as-cleaved GaSe and for the same surface kept one day in ambient atmosphere, respectively. The LEED pattern was acquired at an impinging energy of 120

eV for the as-cleaved sample and 160 eV for the air-exposed GaSe.

In the air-exposed defective GaSe surface (Figure 3.3c-d), the storage of the GaSe sample for one hour in air leads to the conversion of Ga(0), GaSe_x and Ga₂Se₃ species into Ga₂O₃ and GaSe_xO, whose spectral component increased up to 15% of the total spectral area of the Ga-3d core levels. Notably, the Ga₂O₃ thickness is estimated to be (1.0 ± 0.1) nm (~ 1.7 QL), so that so that the oxidation is inferred to be about 30 times more effective on the defective sample compared to the pristine one.

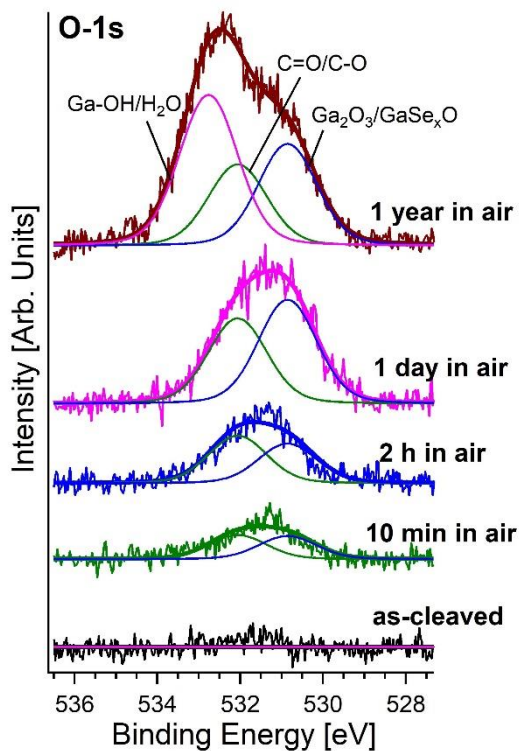
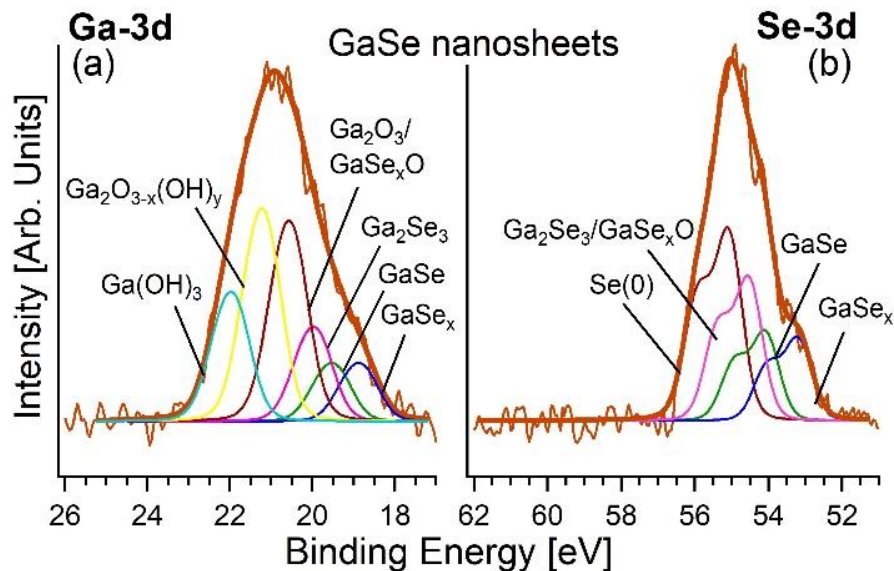


Figure 3.6: O-1s core level spectra collected from GaSe exposed to air for 10 min, 2 hours, 1 day and 1 year. The photon energy is 830 eV. The black curve collected from the as-cleaved sample is provided as a reference.

Surface oxidation is expected to be even more relevant for the case of exfoliated nanosheets, which provide edge sites particularly active toward reactions with ambient gases. To prove the inevitable oxidation of GaSe nanosheets, we measured Ga-3d (Figure 3.7a) and Se-3d (Figure 3.7b) core levels in exfoliated flakes obtained by liquid-phase exfoliation, while O-1s core level is reported in Figure 3.8a. In Ga-3d of GaSe nanosheets (Figure 3.7a), the hydroxylated components are predominant together with Ga₂O₃ (45% and 27% of the total spectral area, respectively). Remarkably, we did not observe any trace of SeO₂ in Se-3d (Figure 3.7b) even in air-exposed GaSe nanosheets, as demonstrated by the absence of the related spectral component at BE of 59-60 eV [109, 110]. However, the formation of atomic Se (38%) and GaSe_xO/Ga₂Se₃ phases (28%) was detected in Se-3d core level of exfoliated GaSe flakes. The estimated thickness of the gallium-oxide phase in GaSe nanosheets is (1.8 ± 0.2) nm, corresponding to ~3 QL.

Conversely, in exfoliated InSe (Figure 3.7c-d), the SeO₂ component in Se-3d core levels was observed at BE = 59.9 eV [111, 112], with a contribution of 9% of the total spectral area. The Se-3d spectrum also indicated the presence of atomic Se(0) with BE = 55.5 eV (12% of the total spectral area), InSe_xO with BE = 54.8 eV (30%), and In₂Se₃ at BE = 54.65 eV (33%), the O-1s spectra is reported in Figure 3.8b. To understand the dissimilar behavior regarding the formation of SeO₂ phases in GaSe and InSe nanosheets, one should consider that healing of Se-vacancy sites in GaSe is more energetically favorable by even 56.7 kJ with respect to the case of InSe. Therefore, in InSe nanosheets part of Se atoms participate to the formation of the SeO₂ phase. Correspondingly, the In-3d core levels of InSe nanosheets (Figure 3.7c) exhibited components due to In₂Se₃ (33%) at BE = 445.3 eV, InSe_xO/In₂O₃ (36%) at BE = 445.46 eV and In₂O_{3-x}(OH)_y (19.7%) at BE = 446 eV for J = 5/2 components [113], respectively. We estimate the thickness of In₂O₃ skin to be (1.3 ± 0.1) nm, which corresponds to ~1.5 QL, considering c = 0.89 nm for O-In-O-In-O stacking.



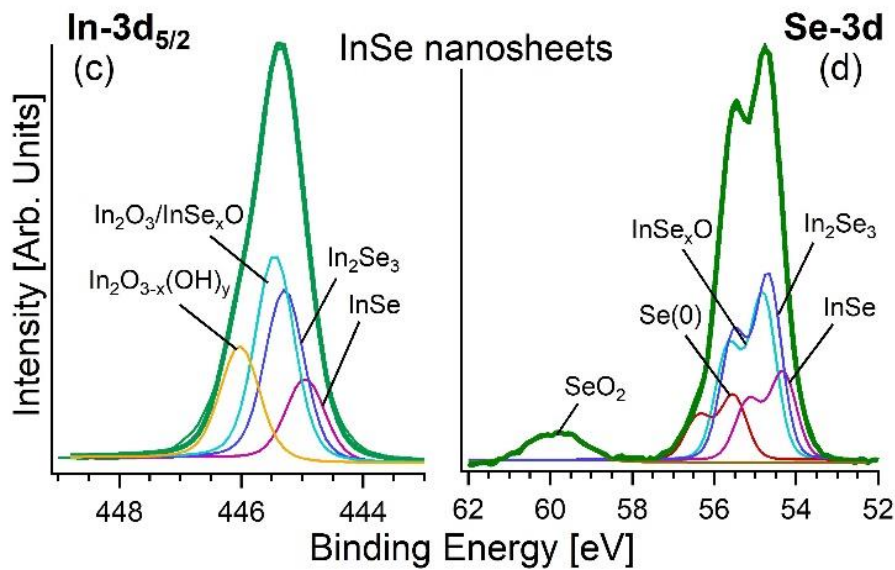


Figure 3.7: (a-b) Ga-3d and Se-3d core levels for exfoliated GaSe sample. (c-d) In-3d_{5/2} and Se-3d for exfoliated InSe. The photon energy is 1486.6 eV (Al K α) and the spectra are normalized to the maximum.

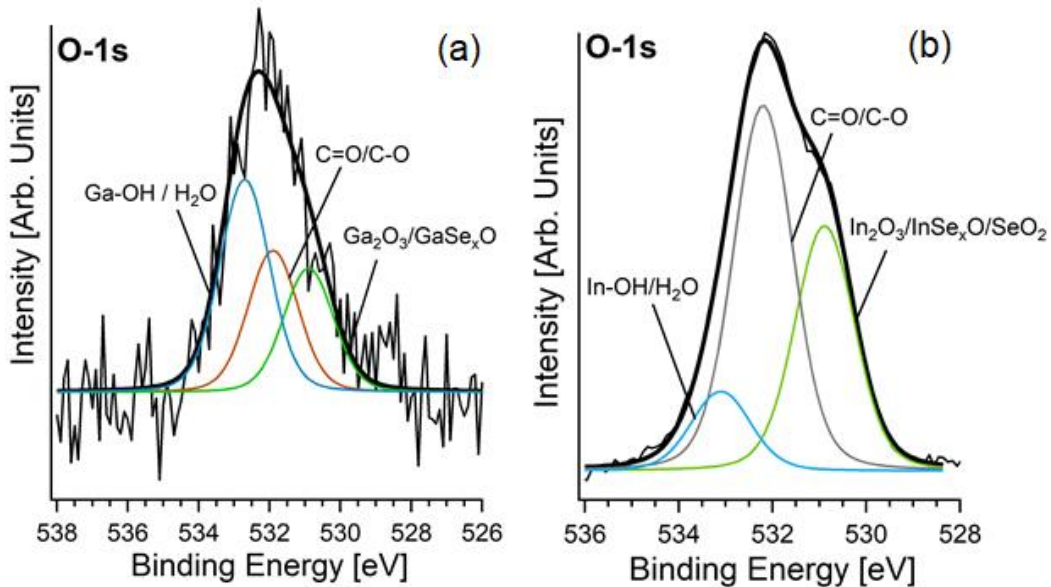


Figure 3.8: (a) and (b) O-1s core levels of exfoliated GaSe and InSe nanosheets, respectively. The photon energy is 1486.6 eV (Al K α).

To evaluate the crystalline order in the formed oxide skin, we carried out low-energy electron microscopy (LEEM) experiments. The LEEM image of the GaSe surface kept 40 days in air (Figure 3.9b) did not exhibit features in the I-V curve (Figure 3.10a), which is typical for amorphous layers. Similarly, the absence of

spots in the corresponding microprobe low-energy electron diffraction (μ -LEED) image (Figure 3.10b-c) confirmed that the formed Ga_2O_3 skin is amorphous. In the LEEM image of the sample aged in air (Figure 3.9b), it is possible to identify the presence of nanometric heterogeneities, possibly corresponding to the initial stages of surface oxidation. Specifically, their lateral size ranged between 50 and 100 nm and they appear as three-dimensional structures in laterally resolved X-ray photoemission electron microscopy data.

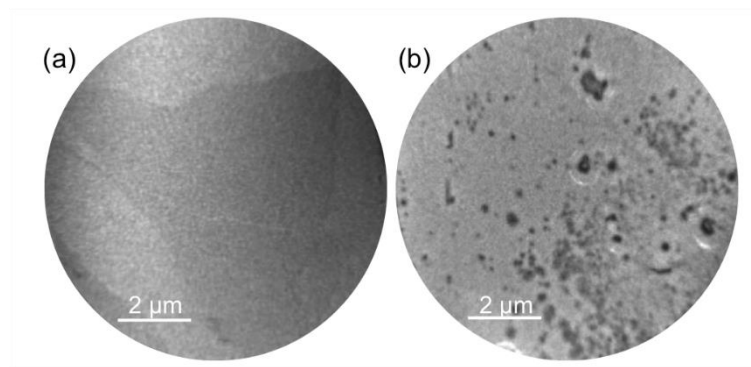


Figure 3.9: LEEM images of: (a) as-cleaved GaSe and (b) the same surface after 40 days in air (at kinetic energies of 5.0 and 0.6 eV, respectively). Observed nanometric heterogeneities in panel (b) may correspond to the nucleation sites at which the oxidation starts.

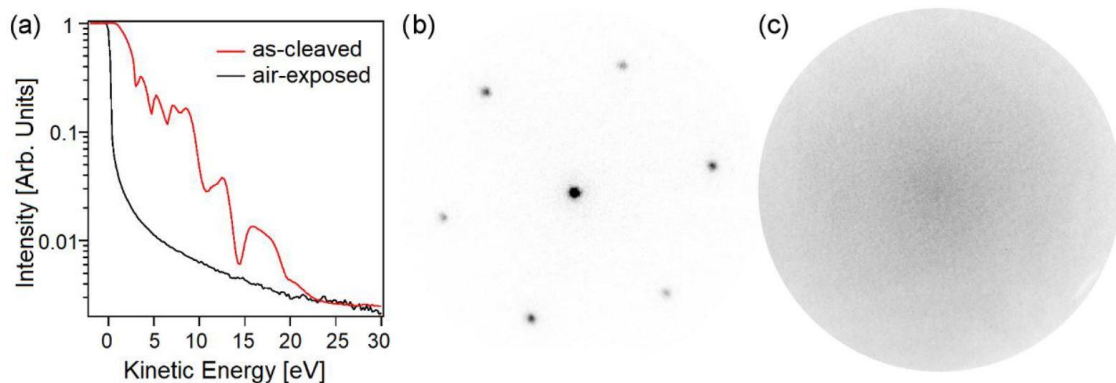


Figure 3.10: (a) LEEM I(V) curves corresponding to the surface before and after air exposure. The other panels report μ -LEED images of (b) the GaSe surface as cleaved (kinetic energy = 37 eV) and (c) after 40 days of air exposure (kinetic energy = 45 eV). The absence of diffraction spots after air exposure indicates the formation of an amorphous oxide layer.

Electrocatalysis and photocatalysis. To assess the impact of oxidation of

GaSe in electrocatalysis, we modelled HER and OER for pristine, defective and oxidized bulk and monolayer GaSe using DFT methods. For the sake of comparison, we also considered InSe.

Remarkably, calculated values of free energies for HER (Figure 3.11a) evidence unsuitability of both bulk GaSe and InSe for this reaction, with energy barriers as high as 1.9 and 1.5 eV/H⁺, respectively. The presence of Se vacancies in both GaSe and InSe significantly decreases the energy cost of the process (1.5 and 0.7 eV/H⁺, respectively), but the magnitude is still significantly larger than that of the Pt(111) surface (0.1 eV/H⁺), usually taken as standard reference (Figure 3.11a) ^[114]. In the case of free-standing monolayers (dashed lines in Figure 3.11a), the values of the energy cost of HER are even larger, i.e., 2.2 and 1.8 eV for GaSe and InSe, respectively. Therefore, the common picture that liquid-phase exfoliation of GaSe and InSe favors the improvement of HER performance on the basis of the prominence of edges behaving as active sites, recently proposed in Refs. ^[26, 76], should be revised. On the contrary, calculated values for Ga₂O₃ and the sub-stoichiometric oxide Ga₂O_{2.97} are 1.1 and -0.3 eV/H⁺. Therefore, for Ga₂O_{2.97} the Heyrovsky step (H_{ads} + H⁺ + e⁻ → H₂) of HER is exothermic.

In the case of OER, in both acidic and alkali media, we find large negative values of free energy (-7.4 and -5.7 eV in acidic and alkali media, respectively) for pristine GaSe, making third step energetically unfavorable (Figure 3.11b,c), owing to the favorability of GaSe oxidation. Thus, the surface of bulk GaSe will be irreversibly oxidized during OER in both acidic and alkali environments.

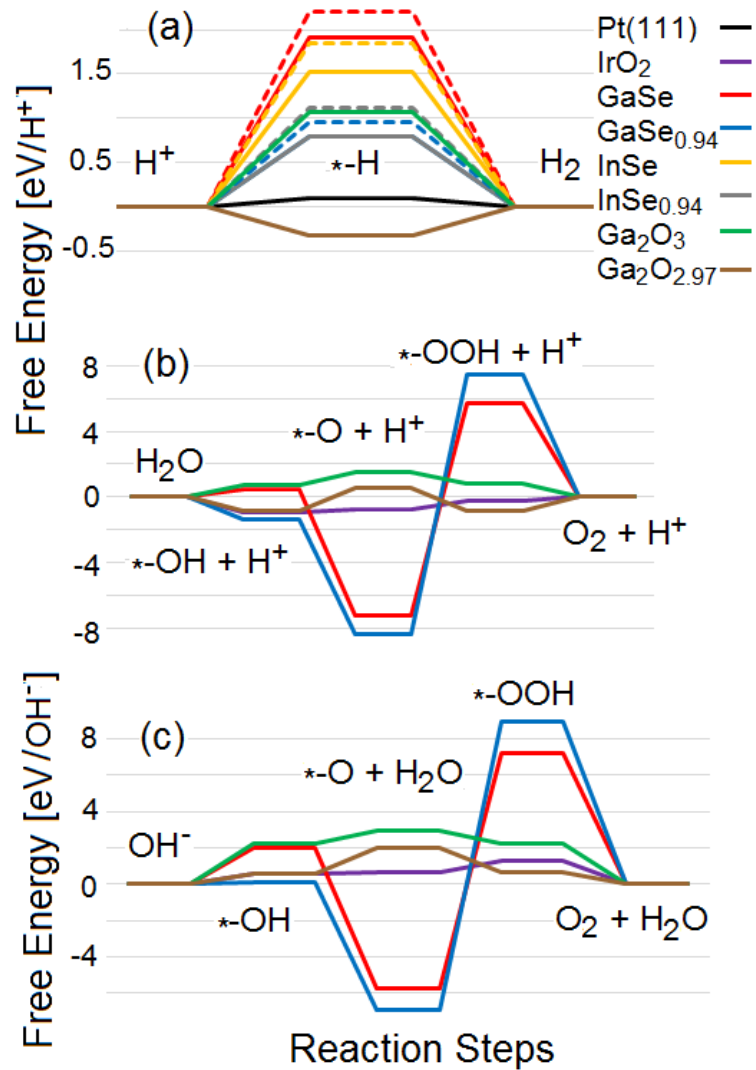


Figure 3.11: (a) Free energy diagram for HER in acidic environment over the surface of bulk and monolayers of GaSe, GaSe_{0.94}, InSe and InSe_{0.94} and over the surface of Ga₂O₃ and Ga₂O_{2.97}. Results for monolayers are shown by dashed lines. Note that the line related to the free energy for GaSe_{0.94} is overlapped with that associated to InSe_{0.94}. (b, c) Free energy diagrams for OER in (b) acidic and (c) alkali media over the surface of bulk GaSe, GaSe_{0.94}, Ga₂O₃ and Ga₂O_{2.97}. For the sake of comparison, data for HER over Pt(111) substrate and OER over IrO₂ are also reported.

Considering the inevitable formation of Ga₂O₃-skin over GaSe substrate exposed to oxidative environments, we modelled OER over the (001) surface of Ga₂O₃ (Figure 3.11b-c). We find that the Ga₂O₃ skin has reduced energy barriers for OER in both acidic and alkali environments, i.e., 1.5 and 2.9 eV, respectively. The presence of oxygen vacancies additionally decreases energy cost of OER in both environments to 0.5 and 2.0 eV, respectively. Our results are consistent with

previous theoretical ^[115] and experimental ^[116] results for water-gas shift reactions catalyzed by defective Ga₂O₃.

Actually, our findings enable re-interpreting literature data on electrocatalysis and photocatalysis based on GaSe. The lowest Tafel slope (150 mV dec⁻¹) in HER was found in nominally reduced GaSe, for which authors claimed the removal of the passivation layer of Ga₂O₃, supposed to poison active sites of GaSe surface. However, surface treatments as those in Ref. ^[117] are expected to promote the formation of sub-stoichiometric Ga₂O_{3-x} phases, which indeed we demonstrate to represent a suitable platform for HER, according to our model depicted in Figure 3.11a.

Recently, liquid-phase exfoliated GaSe nanosheets have been used ^[26] to produce photoelectrodes exhibiting catalytic activity toward water splitting reactions, i.e., HER and OER. Based on our model, it is evident that the role of GaSe in photochemical water splitting is just to generate electron-hole pairs via light harvesting, while Ga₂O₃ skin represents the only chemically active part of the photoelectrode.

Likewise, recently, it has been reported the HER-activity of InSe flakes increases when the thickness is reduced into atomically thin layers ^[76]. Explicitly, the overpotential at a 10 mA cm⁻² cathodic current density (η_{10}) value decreased from 581 mV (540 mV) in the bulk samples to 549 mV (451 mV) in few-layer flakes in an acid (alkaline) environment. This size effect led to the identification of the active sites for HER at the edges of the InSe nanosheets.

Conclusions

In this section it has been shown that oxidation of GaSe (and InSe) into Ga₂O₃ (In₂Se₃), promoted by exfoliation in nanosheets or by the presence of defects in sub-stoichiometric crystals, plays a key role in the recently reported improved performance of electrochemical and photocatalytic reactions upon exfoliation of GaSe in atomically thin layers. Explicitly, both HER and OER are energetically unfavorable in pristine GaSe, due to energy barriers of 1.9 and 5.7–7.4 eV, respectively. Exfoliation in nanosheets even increases the energy barrier for HER up to 2.2 eV. On the contrary, the Heyrovsky step ($H_{ads} + H^+ + e^- \rightarrow H_2$) of HER is energetically favorable in sub-stoichiometric Ga₂O_{2.97} (- 0.3 eV/H⁺). Therefore,

these results elucidate the role of surface oxides in electrocatalysis and photocatalysis based on nanosheets of III-VI layered semiconductors. These findings pave the way for a novel generation of efficient and cost-effective (photo-) electrocatalysts, based on self-assembled heterostructures formed by taking advantage on the natural interaction of sub-stoichiometric van der Waals semiconductors with air.

SnSe₂ a layered semiconductor for sensing

Introduction

Tin diselenide (SnSe₂) is a van der Waals semiconductor. As introduced above all Sn-based chalcogenides are usually affected by rapid surface degradation with the emergence of tin-oxide phases ^[56, 57]. Additionally, the oxidation of starting element Sn during the synthesis can also influence the transport properties of the resulting crystal. Therefore, technological exploitation of Sn-based chalcogenides remains particularly challenging. Especially, stability in ambient atmosphere of SnSe₂-based devices is related to the chemical reactivity of its surface.

Recently, in ^[118] we have shown that, though stoichiometric SnSe₂ shows outstanding chemical stability in ambient conditions, the presence of selenium vacancies drastically affects surface chemical reactivity. The SnSe_{2-x} surface is transformed into SnO₂-skin-terminated SnSe₂, with a thickness of the SnO₂ skin estimated to be sub-nanometric ^[118]. Unexpectedly, the self-assembled heterostructure formed exploiting the natural interaction with air is particularly appropriate for ultrasensitive gas sensing, as demonstrated for NO₂ and H₂ with sensitivities of (1.06 ± 0.03) and (0.43 ± 0.02) [ppm]⁻¹, respectively ^[118]. Remarkably, the oxide skin plays a pivotal role in NO₂ and H₂ sensing, congruently with the abundant literature on SnO₂-based sensors ^[119-128]. The modulation of resistivity upon gas adsorption is strictly connected to charge distribution in the sensing material, ultimately related to the formation of surface dipoles at the SnO₂-SnSe₂ heterojunction arising from local charge redistribution. Thus, to understand the

conduction mechanism ruling chemical sensing, it is crucial to shed light on charge redistribution at the SnO₂/SnSe₂ heterostructure by measuring work-function changes. Furthermore, sensing experiments in Ref. [118] were carried out in dry air, thus stability in humid environment remains unexplored, although real conditions mandatorily require sensors to work in a changing humidity background [129, 130]. Despite the relevance of the influence of the humid environment for practical applications, surprisingly it has been scarcely investigated, although previous reports indicated a decrease of resistance under exposure to humidity atmosphere [129, 130], which represents an unambiguous fingerprint that H₂O behaves as a reducing gas in the interaction with the SnO₂ surface.

In addition, the interaction with water is relevant also to understand the stability of any other SnSe₂-based (opto)electronic device [131] working in ambient humidity, as well as the eventual environmental doping effects in transport properties [132].

Here, in this section it is displayed the surface properties of SnSe₂ single crystals and their modifications in oxidative and humid environments by means of surface-science experiments and density functional theory (DFT).

Methods

Computational methods. See section 2 p.19

Single-crystal growth. The single crystals were grown by Bridgman-Stockbarger method.

XPS. Experiments were carried out at the APE-HE beamline at the Elettra-Trieste synchrotron. Core-level measurements were performed with an Omicron EA125 hemispherical electron energy analyzer, with the sample at room temperature and in normal emission. Linearly polarized light formed an angle of 45° with respect to the perpendicular direction of the surface.

HREELS. Vibrational experiments were carried out at room temperature with a Delta 0.5 spectrometer (Specs GmbH, Germany). The experimental resolution is 3-4 meV. The primary electron beam energy was 3.5 eV. Spectra were acquired in specular conditions.

LEEM. EELS (Figure 3.13) and work-function changes $\Delta\Phi$ (Figure 3.14a)

measurements were carried out at the soft X-ray beamline Nanospectroscopy at Elettra-Trieste synchrotron, using an energy filtered LEEM-PEEM microscopy with spatial resolution of 10 nm. Specifically, measurements of $\Delta\Phi$ were carried out by varying the electron beam energy across the total electron reflectivity threshold. This threshold is commonly termed as MEM-LEEM transition, which is characterized by a step drop of intensity as a function of a bias voltage applied to the sample (start voltage) as a decelerating potential. The $\Delta\Phi$ value is identified by the shifts in the bias potential corresponding to the MEM-LEEM transition.

Results and discussion

Tin diselenide (SnSe_2) is a van der Waals semiconductor with CdI_2 -type crystal structure [23], belonging to the $P-3m1$ space group, with tin (Sn) atoms interweaved between two hexagonally packed atomic layers of selenium (Se) (see Figure 3.12a-b) [24, 25]. To check the purity of the single crystal a XPS survey spectrum is reported in Figure A.7 (Appendix G) that proves the absence of contaminants in the bulk.

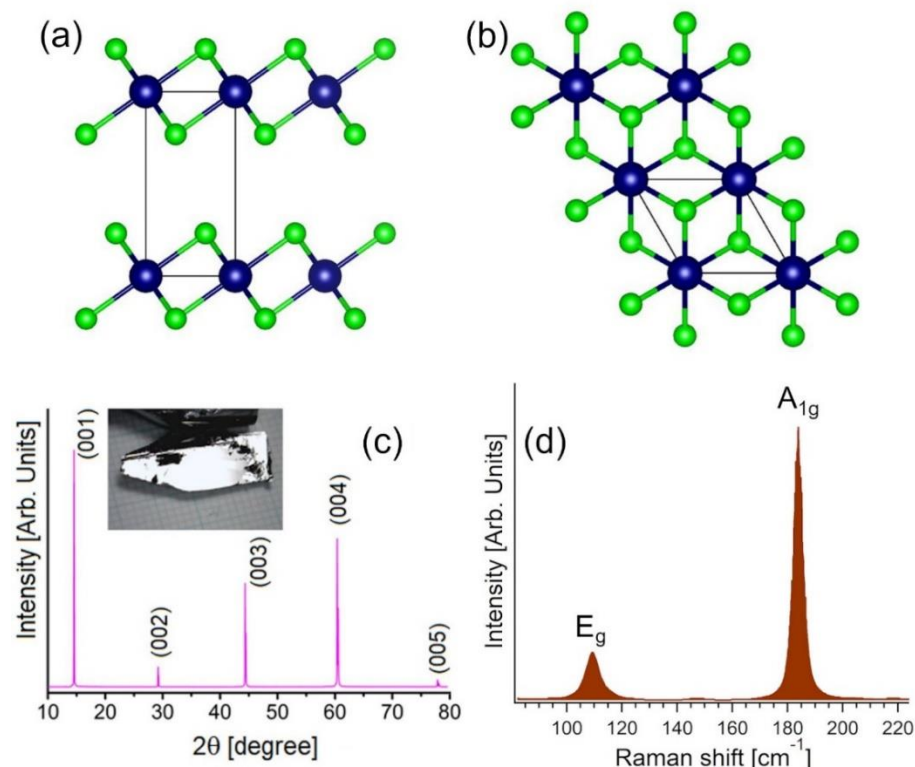


Figure 3.12: (a) Side and (b) top views of the atomic structure of SnSe_2 . Green and blue

balls denote Se and Sn atoms, respectively. Panel (c) reports the single-crystal XRD pattern from the (001) plane of SnSe₂. The inset shows a photograph of an as-grown SnSe₂ single crystal. Panel (d) reports the Raman spectrum of SnSe₂ single crystal acquired at room temperature with a laser with wavelength $\lambda = 632.8$ nm.

The analysis of the variation of the work function $\Delta\Phi$ probed by low-energy electron microscopy (LEEM) could provide important insights into charge redistribution arising from surface oxidation (Figure 3.14a), as the total reflectivity threshold in electron backscattering (the MEM-LEEM transition, with MEM standing for mirror electron microscopy) represents a direct measurement of the variation of the surface potential [133]. Explicitly, we find $\Delta\Phi$ to be +0.23 eV for the SnSe₂ surface modified by 700 L O₂ exposure at room temperature, while air exposure for 15 minutes induces a further shift in the work function, resulting in a total increase by +0.40 eV. The observed value of $\Delta\Phi$ can be explained by considering the activation of surface dipoles, due to charge transfer at the interface from substrate to adsorbed oxygen atoms. The electronegativity of oxygen makes its adsorption generally associated with a charge transfer from the substrate to the adsorbate layer, with a subsequent increase of the work function [134]. Considering that the work function of pristine SnSe₂ single crystal is ~4.6 eV [135], while that of SnO₂ is known to be ~4.9 eV [136] (although its value can be tuned by reduction reactions [137]), both the sign and the magnitude of the experimental value of $\Delta\Phi$ are consistent with surface oxidation, involving the formation of a sub-nanometric SnO₂ skin. We can infer that previous experimental studies reporting a work function of SnSe₂ of (5.0 ± 0.1) eV [138, 139] could be affected by surface oxidation, which generates a self-assembled SnO₂/SnSe₂ heterostructure with increased work function. To verify this statement, we calculated $\Delta\Phi$ for the oxidation process of the pristine SnSe₂ surface, finding a value of +0.52 eV in qualitative agreement with experimental measurements. We also note that, in the air-exposed sample, variations in the I-V curve associated to electron diffraction from a surface with crystalline order [140] are suppressed, due to the formation of a disordered surface oxide phase.

Complementary information on the electronic properties of the SnO₂/SnSe₂ heterostructure was achieved by the surface excitation spectrum probed by electron energy loss spectroscopy (EELS) (Figure 3.13). Especially, EELS

extended up to the ultraviolet range of the electromagnetic spectrum (Figure 3.13), enables monitoring the surface status with a technique with probing depth as low as (0.9 ± 0.1) nm in our experimental conditions ^[141], which is lower by more than 10^2 with respect to optical techniques. Specifically, the excitation spectrum of the as-cleaved SnSe₂ surface shows a main feature at 15.9 eV with a shoulder at 12.0 eV, ascribed to interband transitions from Se-4s core levels and, moreover, two weak losses at 7.5 and 26.8 eV. The excitation spectrum of the air-exposed SnSe₂ sample is dominated by an emerging broad mode centered around ~ 18 eV, with two weak peaks at 7.5 and 26.8 eV, evidently insensitive to surface modification. Notably, polycrystalline SnO₂ films display the feature at 18.0 eV. Precisely, this feature was previously attributed to sub-oxide SnO_{2-x} phases ^[142]. However, that the mode at 18.0 eV is related to a single-particle transition starting from O-2s band in SnO₂.

For the sake of completeness, we mention that the weak peaks at 7.5 and 26.8 eV are ascribed to interband transitions originated by Sn-5s and Se-3s levels, respectively.

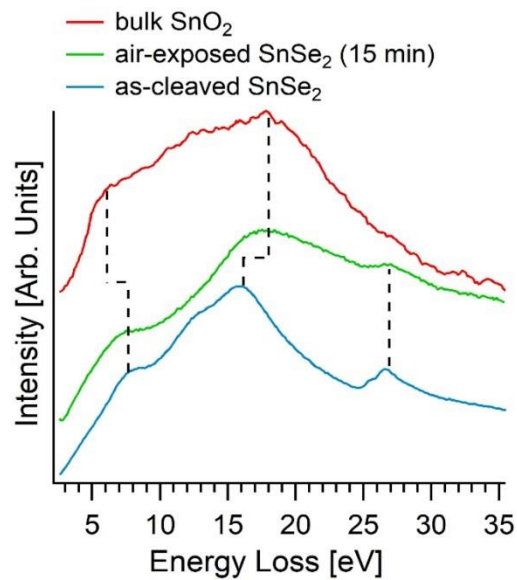


Figure 3.13: Excitation spectrum, probed for a primary electron beam energy of 300 eV, for as-cleaved SnSe₂ and the same surface exposed to air for 15 minutes. For the sake of comparison, we also report data for bulk SnO₂.

To estimate the amount of the charge transfer between the SnSe₂ substrate and the SnO₂ skin, we calculated the charge density distribution of: (i) one SnO₂ layer over two layers of SnSe₂ (to model the SnO₂/SnSe₂ heterostructure); (ii) a free-standing SnO₂ single unit; and (ii) a bilayer of SnSe₂. Then, we calculated the difference between the charge densities of the whole SnO₂/SnSe₂ interface and those one of its components (single SnO₂ unit and bilayer SnSe₂). The obtained charge density difference (Figure 3.14b) illustrates charge redistribution following the formation of SnO₂/SnSe₂ interface. The

integration of the charge density difference along the c axis provides information regarding the charge transfer between the SnSe_2 substrate and the SnO_2 skin. Note that the formation of the $\text{SnO}_2/\text{SnSe}_2$ interface provides changes in charge density difference not the only in the outermost SnSe_2 layer, but also in the subsurface area, namely the second SnSe_2 layer. Definitely, the charge transfer is estimated to be $0.56 e^-$ per SnO_2 unit.

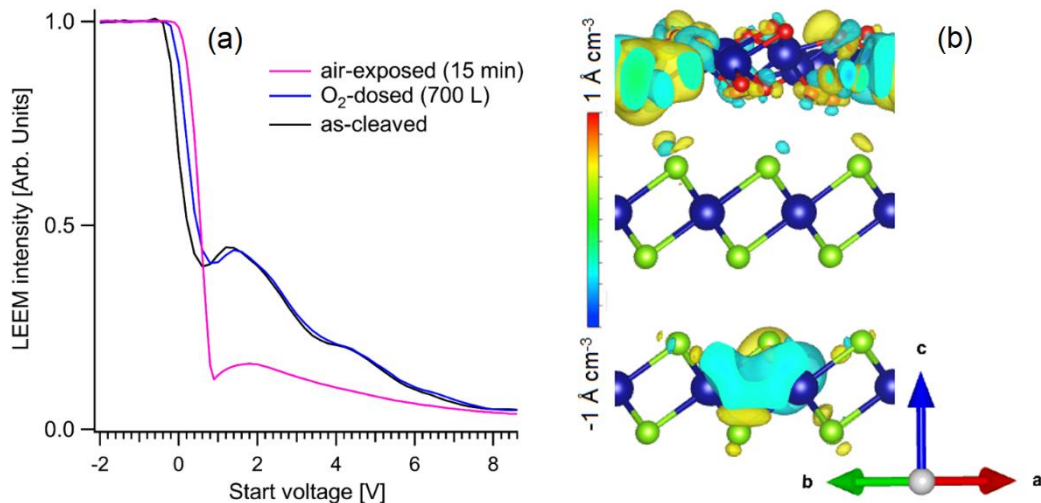


Figure 3.14: (a) LEEM-IV curves at the MEM-LEEM transition for the as-cleaved sample (black curve), after a dosage of 700 L of O_2 (blue curve) and after air exposure for 15 minutes (pink curve). The shift of the MEM-LEEM transition, characterized by the sharp decrease in intensity, indicates an oxidation-induced modification of the surface potential. (b) Changes of the charge density after the formation of the interface between SnSe_2 substrate and SnO_2 -skin. Sn, Se and O atoms are represented by dark blue, light green and red balls, respectively.

While the adsorption of O_2 with further decomposition is energetically favorable on SnSe_2 (negative values of ΔG and ΔH_{dec}), as well as on $\text{SnSe}_{1.88}$ and SnSe (Table VI), our theoretical model indicates that water does not adsorb on SnSe_2 . The energy cost of water adsorption is lowered in the presence of Se vacancies ($\text{SnSe}_{1.88}$) up to ~ 3 kJ/mol, although water adsorption (as well as decomposition) remains energetically unfavorable. Similarly, also SnSe shows outstanding chemical inertness toward water.

On the other hand, the $\text{SnO}_2/\text{SnSe}_2$ heterostructure shows superior chemical reactivity towards ambient species with respect to SnSe_2 . On the pristine SnSe_2

surface, the local rearrangement of chemical bonds around each adsorbed water molecule originates a redistribution of the charge density in the surface layer of SnSe₂ with a charge transfer of 0.17 e⁻ per water molecule (Figure 3.15a). Hence, we conclude that pristine SnSe₂ is stable in humid environment and, consequently, it is unsuitable for humidity sensing, contrarily to conclusions in Refs. [143-145]. On the other hand, adsorption of H₂O on SnO₂/SnSe₂ (Figure 3.15b) is energetically favorable even above room temperature. The values of transferred charge from H₂O to the SnO₂ skin are 0.43 and 0.30 e⁻ for one and two H₂O molecules per supercell, respectively. Correspondingly, DOS (Figure 3.15c) is modified with a direct correlation with the coverage of the adsorbate, hence proving the appropriateness for humidity sensing also at low concentrations of H₂O.

Note that decomposition of water molecule on the SnO₂-skin-terminated SnSe₂ is an exothermic process (see Table VI), although the energy gain from this process is moderate (-121.31 kJ/mol) and further water splitting is unfavorable, supporting the possible reversibility of the process.

Table VI: Differential enthalpy ΔH_{ads} , differential Gibbs free energy of physisorption ΔG and differential enthalpy of decomposition ΔH_{dec} for molecular oxygen and water on pristine SnSe₂, SnSe_{1.88} and SnSe surfaces. For oxygen decomposition, the table also displays the differential enthalpy of the oxidation of whole surface with formation of SnO and SnO₂-like layers (in parenthesis).

Surface	Adsorbant	Physisorption		Decomposition
		ΔH_{ads} [kJ/mol]	ΔG [kJ/mol]	ΔH_{dec} [kJ/mol]
SnSe ₂	O ₂	-17.46	-3.16	-42.28 (-161.58 / ~ -40.2)
	H ₂ O	-13.27	+18.03	+220.91

SnSe _{1.88}	O ₂	-37.58	-26.28	-135.67 (-99.05 / -406.65)
	H ₂ O	-27.93	+3.37	+175.61
SnSe	O ₂	-11.53	-0.23	-236.03 (-323.10/ +95.4)
	H ₂ O	-8.12	+23.18	+82.22
SnO ₂ -skin	H ₂ O	-119.70	-106.67	-121.31

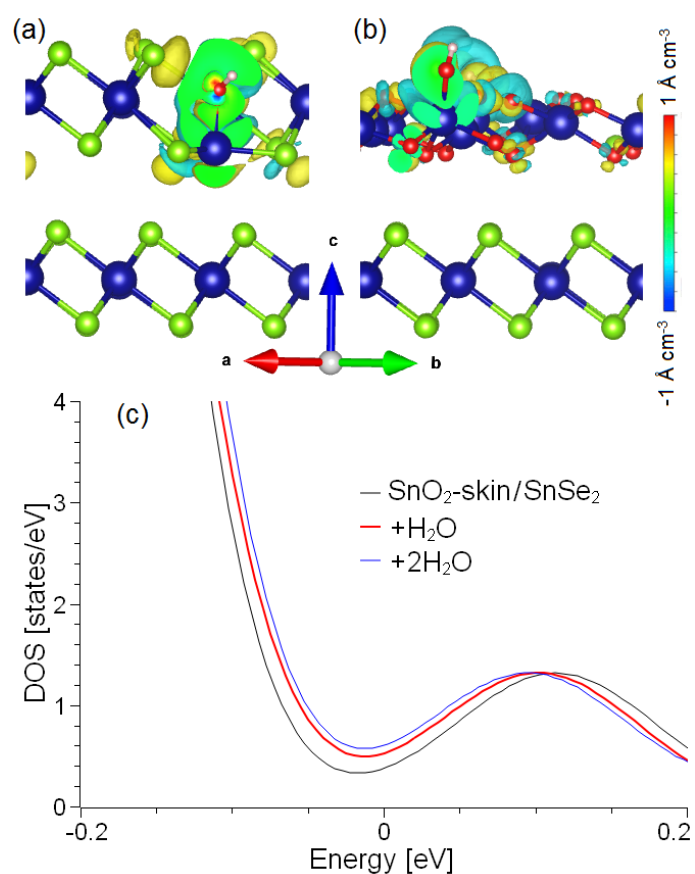


Figure 3.15: Changes of the charge density after adsorption of one water molecule on (a) SnSe₂ and (b) SnO₂-skin-terminated SnSe₂. Panel (c) represents the DOS of SnO₂-skin-terminated SnSe₂ (black curve) and of the same system modified by the adsorption of one (red curve) and two (blue curve) water molecules. The Fermi level is set at 0.

Recently, different authors ^[143-145] have reported the outstanding performances of SnSe₂ in humidity sensing devices. Our findings elucidate the key role of the surface oxide skin in the interaction with humid environment. On the other hand, in Refs. ^[143-145] surface oxidation was not assessed, thus the mechanism ruling humidity sensing discussed therein should be re-interpreted.

Theoretical results were validated by surface-science techniques. In particular, high-resolution electron energy loss spectroscopy (HREELS) experiments on water-dosed Sn-based selenides (SnSe, SnSe_{1.4}, SnSe_{1.7}, SnSe₂) indicate the absence of chemisorbed water-derived species, as indicated by the lack of O-H stretching at 408-425 meV (molecular water) and 445-460 meV (hydroxyl groups) in spectra in Figure 3.16 (see Ref. ^[146] for more details). These findings are consistent with the positive differential Gibbs free energy of adsorption (corresponding to energetically unfavorable water adsorption) in Table VI. For the sake of comparison, we report in Figure 3.16 also vibrational data obtained after having exposed to the same dose of H₂O (10⁵ L) at room temperature the surface of other metal chalcogenides, which instead enable the stable adsorption of water molecules (PtTe_{1.6}) and hydroxyl groups (InSe). The absence of reactivity toward water of Sn-based chalcogenides makes them suitable for catalysis (especially, photocatalytic water splitting ^[43] and hydrogen evolution reaction ^[147]) and drug delivery ^[148] (also considering that neither Sn nor Se are toxic). Congruently, SnSe₂ was used as a co-catalyst in combination with TiO₂ for hydrogen evolution reaction ^[54].

Further information on the surface chemical bonds is gained by the inspection of core levels via X-ray photoelectron spectroscopy (XPS) experiments. Figure 3.17 shows the Sn-3d and Se-3d core levels of the SnSe₂ single-crystal surface cleaved in ultra-high vacuum and for the same surface modified by O₂ and H₂O dosage with a total dose of 10⁵ L. The as-cleaved surface shows the Sn-3d_{5/2} core level at a binding energy (BE) of 486.8 eV (Figure 3.17b). Congruently, the Se-3d_{5/2} core level had a single component at BE=54.1 eV, in agreement with previous results for SnSe₂ ^[149] and with a shift by +0.4 eV compared to the case of SnSe. Surface treatments, i.e. 10⁵ L of O₂ and H₂O exposure, only induce slight changes in Se-3d core levels. A novel doublet appeared in Se-3d (BE=53.7 eV for 3d_{5/2}), whose total spectral area is 5.4% (for O₂ dosage) and 2.6% (for air exposure), arising from Se(0) segregation ^[150]. Especially, from the analysis of Se-3d core-

level spectra (Figure 3.17c), we can infer the absence of O-Se-O bonds, which would have a BE of ~59-60 eV [109, 110, 151]. Congruently, the intensity of the O-1s peak is especially small in SnSe₂ exposed to both oxidative and humid environment (Figure 3.17a).

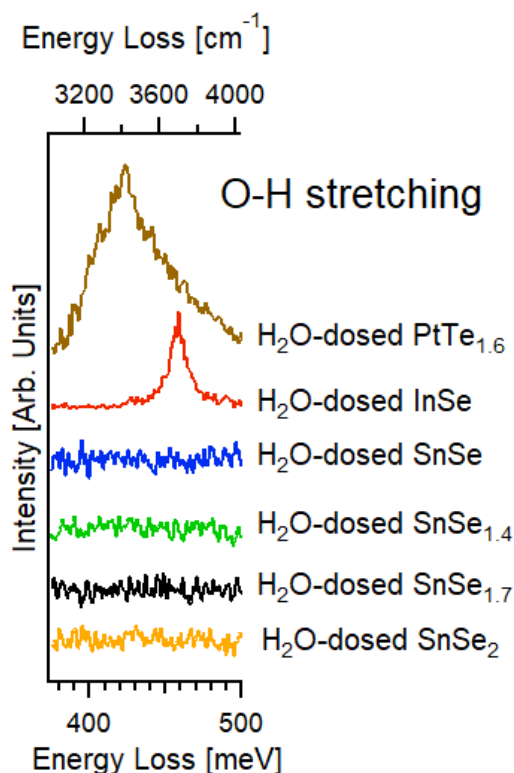


Figure 3.16: HREELS spectra in the region of the O-H band acquired after having exposed to 10^5 L of H₂O at room temperature the surfaces of different Sn-based chalcogenides: SnSe₂ (orange curve), SnSe_{1.7} (black curve), SnSe_{1.4} (green curve), and SnSe (blue curve). To provide a straightforward comparison, the figure also displays data for H₂O-dosed InSe (red curve) and PtTe_{1.6} (brown curve) surfaces (10^5 L at room temperature). The impinging energy is 4 eV.

Contrariwise, we observed well-distinct peaks in SnO₂/SnSe_{2-x} exposed to humid environment (outermost spectra in the various panels of Figure 3.17). Specifically, a Sn-3d doublet with J = 5/2 component is present at BE = 487.8 eV, due to SnO₂ (relative amplitude of 54%), consistently with previous reports for this system [152, 153]. Remarkably, no trace of O-Se-O bonds is present, as suggested by the lack of Se-3d components at 59-60 eV [151]. This result confirms theoretical expectations that Se is only involved in a metastable oxide phase, which represents a precursor for SnO₂ formation.

The analysis of O-1s core-level spectra (Figure 3.17a) for SnSe₂ exposed to humid environment shows new components arising from -OH groups and H₂O at a BE of 531.6 and 533.6 eV, respectively [154-156]. We also exposed the SnO₂/SnSe₂ heterostructure to the humid environment, with the corresponding O-1s spectrum displaying the SnO₂ component at a BE of 531.5 eV [157, 158], overlapped with the -OH component.

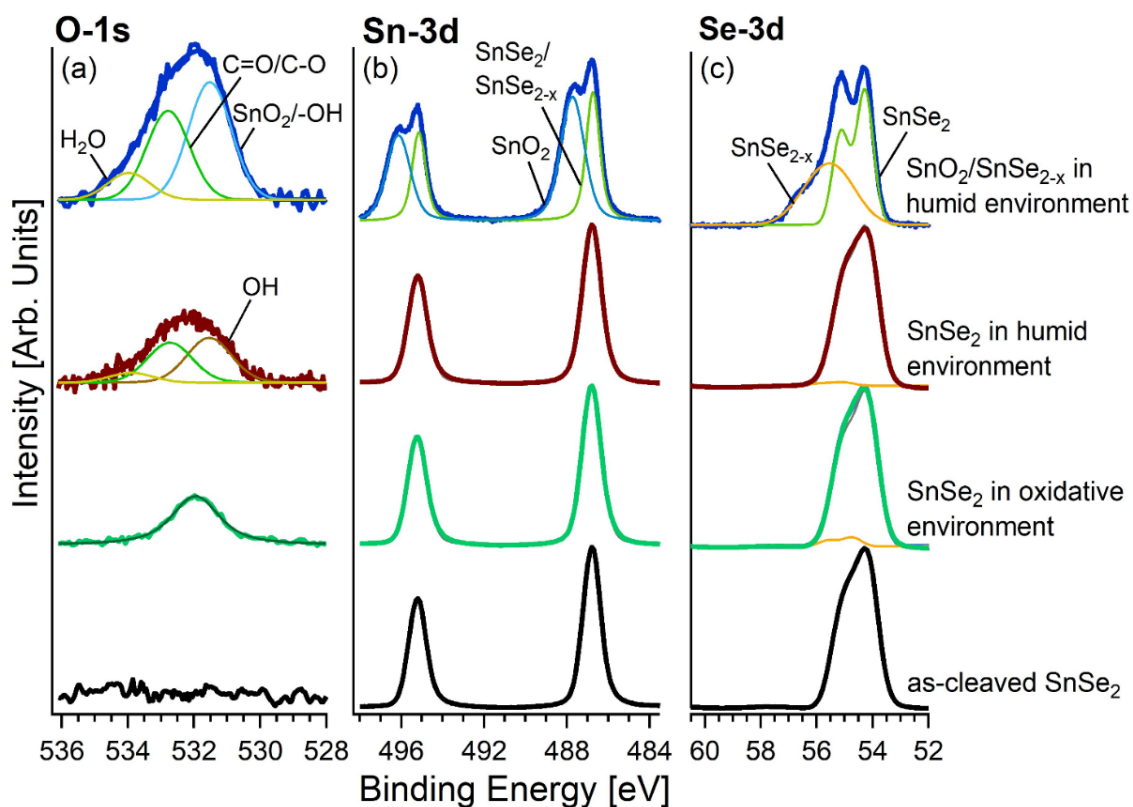


Figure 3.17: (a) O-1s, (b) Sn-3d and (c) Se-3d core levels for the pristine surface of SnSe₂ cleaved in situ in ultrahigh vacuum conditions and its alteration after exposure to O₂ (10⁵ L) and to H₂O (10⁵ L). The photon energy is 800 eV. We also report in each panel the corresponding spectrum for SnO₂/SnSe_{2-x} exposed to humid environment.

Conclusions

In conclusion, in this section the modifications of surface properties whenever pristine SnSe₂ assumes a sub-nanometric SnO₂ skin upon interaction with oxidative environments and the subsequent implications for chemical sensors are investigated. Definitely, the oxidation process has a direct effect on the work function, which is increased by +0.4 eV, owing to the charge transfer between the substrate and the SnO₂ skin of 0.56 e⁻ per SnO₂ unit. Though the SnSe₂ surface is inert to water at room temperature, upon surface oxidation the SnO₂/SnSe₂ interface shows a remarkable sensitivity to humidity. Definitely, these results prove the significant influence of humid environments on the electrical response of the SnO₂/SnSe₂ heterostructure.

References

1. Hu J, et al. Kinetic-Oriented Construction of MoS₂ Synergistic Interface to Boost pH-Universal Hydrogen Evolution. *Adv Funct Mater.* 2020; **30** (6), 1908520.
2. Lihter M, Graf M, Iveković D, Radenovic A. Nanoscale Selective Passivation of Electrodes Contacting a 2D Semiconductor. *Adv Funct Mater.* 2020; **30** (6), 1907860.
3. Xu X, Zhang C, Hota MK, Liu Z, Zhang X, Alshareef HN. Enhanced Quality of Wafer-Scale MoS₂ Films by a Capping Layer Annealing Process. *Adv Funct Mater.* 2020; **30** (11), 1908040.
4. Zhao Y, Cai Y, Zhang L, Li B, Zhang G, Thong JTL. Thermal Transport in 2D Semiconductors—Considerations for Device Applications. *Adv Funct Mater.* 2020; **30** (8), 1903929.
5. Zhou C, et al. Cu Intercalation and Br Doping to Thermoelectric SnSe₂ Lead to Ultrahigh Electron Mobility and Temperature-Independent Power Factor. *Adv Funct Mater.* 2020; **30** (6), 1908405.
6. Ng S, Iffelsberger C, Sofer Z, Pumera M. Tunable Room-Temperature Synthesis of ReS₂ Bicatalyst on 3D- and 2D-Printed Electrodes for Photo- and Electrochemical Energy Applications. *Adv Funct Mater.* 2020; **30** (19), 1910193.
7. Novoselov K. Graphene: Mind the gap. *Nature Materials.* 2007; **6** (10), 720-1.
8. Wang Z, et al. A Noble Metal Dichalcogenide for High-Performance Field-Effect Transistors and Broadband Photodetectors. *Adv Funct Mater.* 2020; **30** (5), 1907945.
9. Sun B, Wang Z, Liu Z, Tan X, Liu X, Shi T, Zhou J, Liao G. Tailoring of Silver Nanocubes with Optimized Localized Surface Plasmon in a Gap Mode for a Flexible MoS₂ Photodetector. *Adv Funct Mater.* 2019; **29** (26), 1900541.
10. Vitiello MS. Nanodevices at terahertz frequency based on 2D materials. *J Phys: Mater.* 2019; **3** (1), 014008.
11. Zhang Y, Zhang F, Xu Y, Huang W, Wu L, Zhang Y, Zhang X, Zhang H. Self-Healable Black Phosphorus Photodetectors. *Adv Funct Mater.* 2019; **29** (49), 1906610.
12. Guo S, et al. Development of a Cloud-Based Epidermal MoSe₂ Device for Hazardous Gas Sensing. *Adv Funct Mater.* 2019; **29** (18).
13. Zheng W, Xu Y, Zheng L, Yang C, Pinna N, Liu X, Zhang J. MoS₂ Van der Waals p-n Junctions Enabling Highly Selective Room-Temperature NO₂ Sensor. *Adv Funct Mater.* 2020.
14. Guo S, et al. Development of a Cloud-Based Epidermal MoSe₂ Device for Hazardous Gas Sensing. *Adv Funct Mater.* 2019; **29** (18), 1900138.
15. Zheng W, Xu Y, Zheng L, Yang C, Pinna N, Liu X, Zhang J. MoS₂ Van der Waals p-n Junctions Enabling Highly Selective Room-Temperature NO₂ Sensor. *Adv Funct Mater.* 2020; **30** (19), 2000435.
16. Wang W, et al. Edge-Enriched Ultrathin MoS₂ Embedded Yolk-Shell TiO₂ with Boosted Charge Transfer for Superior Photocatalytic H₂ Evolution. *Adv Funct Mater.* 2019; **29** (36), 1901958.
17. Zhang Q, et al. Ice-Assisted Synthesis of Black Phosphorus Nanosheets as a Metal-Free Photocatalyst: 2D/2D Heterostructure for Broadband H₂ Evolution. *Adv Funct Mater.* 2019; **29** (28), 1902486.
18. Castellanos-Gomez A. Why all the fuss about 2D semiconductors? *Nat Photon.* 2016; **10** (4), 202-4.
19. Jin Z, Li X, Mullen JT, Kim KW. Intrinsic transport properties of electrons and holes in monolayer transition-metal dichalcogenides. *Phys Rev B.* 2014; **90** (4), 045422.
20. Edmonds MT, et al. Creating a Stable Oxide at the Surface of Black Phosphorus. *ACS Appl Mater Interfaces.* 2015; **7** (27), 14557–62.
21. Kumar A, et al. STM study of exfoliated few layer black phosphorus annealed in ultrahigh vacuum. *2D Materials.* 2019; **6** (1), 015005.
22. Fu M, et al. Defects in Highly Anisotropic Transition-Metal Dichalcogenide PdSe₂. *J Phys Chem Lett.* 2020; **11** (3), 740-6.

23. Li X, Luo N, Chen Y, Zou X, Zhu H. Real-Time Observing Ultrafast Carrier and Phonon Dynamics in Colloidal Tin Chalcogenide van der Waals Nanosheets. *J Phys Chem Lett.* 2019; **10** (13), 3750-5.
24. Wei Z, Wang L, Zhuo M, Ni W, Wang H, Ma J. Layered tin sulfide and selenide anode materials for Li- and Na-ion batteries. *J Mater Chem A.* 2018; **6** (26), 12185-214.
25. Huang Y, Ling C, Liu H, Wang S. Tuning electronic and magnetic properties of SnSe₂ armchair nanoribbons via edge hydrogenation. *Journal of Materials Chemistry C.* 2014; **2** (47), 10175-83.
26. Zappia MI, et al. Solution-Processed GaSe Nanoflake-Based Films for Photoelectrochemical Water Splitting and Photoelectrochemical-Type Photodetectors. *Adv Funct Mater.* 2020; **30** (10), 1909572.
27. Zhao Q, et al. Toward Air Stability of Thin GaSe Devices: Avoiding Environmental and Laser-Induced Degradation by Encapsulation. *Adv Funct Mater.* 2018; **28** (47), 1805304.
28. Zhou X, et al. Strong Second-Harmonic Generation in Atomic Layered GaSe. *J Am Chem Soc.* 2015; **137** (25), 7994-7.
29. Li X, Dong J, Idrobo JC, Puzos AA, Rouleau CM, Geoghegan DB, Ding F, Xiao K. Edge-controlled growth and Etching of two-dimensional GaSe monolayers. *J Am Chem Soc.* 2017; **139** (1), 482-91.
30. Hopkinson DG, et al. Formation and Healing of Defects in Atomically Thin GaSe and InSe. *ACS Nano.* 2019; **13** (5), 5112-23.
31. Hu P, Wen Z, Wang L, Tan P, Xiao K. Synthesis of few-layer GaSe nanosheets for high performance photodetectors. *ACS Nano.* 2012; **6** (7), 5988-94.
32. Kim W, et al. Tunable Graphene-GaSe Dual Heterojunction Device. *Adv Mater.* 2016; **28** (9), 1845-52.
33. Late DJ, Liu B, Luo J, Yan A, Matte HSSR, Grayson M, Rao CNR, Dravid VP. GaS and GaSe ultrathin layer transistors. *Adv Mater.* 2012; **24** (26), 3549-54.
34. Lv Q, et al. Interlayer Band-to-Band Tunneling and Negative Differential Resistance in van der Waals BP/InSe Field-Effect Transistors. *Adv Funct Mater.* 2020; **30** (15), 1910713.
35. Li M, et al. Low-Voltage Operational, Low-Power Consuming, and High Sensitive Tactile Switch Based on 2D Layered InSe Tribotronics. *Adv Funct Mater.* 2019; **29** (19), 1809119.
36. Gao A, et al. Observation of ballistic avalanche phenomena in nanoscale vertical InSe/BP heterostructures. *Nat Nanotechnol.* 2019; **14** (3), 217-22.
37. Curreli N, et al. Liquid Phase Exfoliated Indium Selenide Based Highly Sensitive Photodetectors. *Adv Funct Mater.* 2020; **30** (13), 1908427.
38. Shen T, Ren JC, Liu X, Li S, Liu W. Van der Waals Stacking Induced Transition from Schottky to Ohmic Contacts: 2D Metals on Multilayer InSe. *J Am Chem Soc.* 2019; **141** (7), 3110-5.
39. Bandurin DA, et al. High electron mobility, quantum Hall effect and anomalous optical response in atomically thin InSe. *Nat Nanotechnol.* 2017; **12** (3), 223-7.
40. Yang Y, Jeon J, Park J-H, Jeong MS, Lee BH, Hwang E, Lee S. Plasmonic Transition Metal Carbide Electrodes for High-Performance InSe Photodetectors. *ACS Nano.* 2019; **13** (8), 8804-10.
41. Shafique A, Samad A, Shin Y-H. Ultra low lattice thermal conductivity and high carrier mobility of monolayer SnS₂ and SnSe₂: a first principles study. *Phys Chem Chem Phys.* 2017; **19** (31), 20677-83.
42. Tan P, Chen X, Wu L, Shang YY, Liu W, Pan J, Xiong X. Hierarchical flower-like SnSe₂ supported Ag₃PO₄ nanoparticles: towards visible light driven photocatalyst with enhanced performance. *Appl Catal, B: Environ.* 2017; **202**, 326-34.
43. Fan Y, Wang J, Zhao M. Spontaneous full photocatalytic water splitting on 2D MoSe₂/SnSe₂ and WSe₂/SnSe₂ vdW heterostructures. *Nanoscale.* 2019; **11** (31), 14836-43.
44. Zeng J, et al. Gate-Induced Interfacial Superconductivity in 1T-SnSe₂. *Nano Letters.* 2018; **18** (2), 1410-5.

45. Shao Z, et al. Strongly Compressed Few-Layered SnSe₂ Films Grown on a SrTiO₃ Substrate: The Coexistence of Charge Ordering and Enhanced Interfacial Superconductivity. *Nano Lett.* 2019; **19** (8), 5304-12.
46. Kim S, Yao Z, Lim J-M, Hersam MC, Wolverton C, Dravid VP, He K. Lithium-Ion Batteries: Atomic-Scale Observation of Electrochemically Reversible Phase Transformations in SnSe₂ Single Crystals. *Adv Mater.* 2018; **30** (51), 1870393.
47. Bai J, Wu H, Wang S, Zhang G, Feng C, Liu H. Synthesis of CoSe₂-SnSe₂ nanocube-coated nitrogen-doped carbon (NC) as anode for lithium and sodium ion batteries. *Appl Surf Sci.* 2019; **488**, 512-21.
48. Zhang F, Xia C, Zhu J, Ahmed B, Liang H, Velusamy DB, Schwingenschlöggl U, Alshareef HN. SnSe 2 2D Anodes for Advanced Sodium Ion Batteries. *Adv Energy Mater.* 2016; **6** (22), 1601188.
49. Zhou X, et al. Vertical heterostructures based on SnSe₂/MoS₂ for high performance photodetectors. *2D Materials.* 2017; **4** (2), 025048.
50. Wang M, Wang Z, Xu X, Duan S, Du C. Tin diselenide-based saturable absorbers for eye-safe pulse lasers. *Nanotechnology.* 2019; **30** (26), 265703.
51. Zhang Y, et al. Tin Diselenide Molecular Precursor for Solution-Processable Thermoelectric Materials. *Angew Chem.* 2018; **57** (52), 17063-8.
52. Luo Y, et al. n-Type SnSe₂ Oriented-Nanoplate-Based Pellets for High Thermoelectric Performance. *Adv Energy Mater.* 2018; **8** (8), 1702167.
53. Sun J, Liu S, Wang C, Bai Y, Chen G, Luo Q, Ma F. Interface tuning charge transport and enhanced thermoelectric properties in flower-like SnSe₂ hierarchical nanostructures. *Appl Surf Sci.* 2020; **510**, 145478.
54. Nasir MS, Yang G, Ayub I, Wang X, Wang S, Nasir A, Yan W. Tin diselenide nanoflakes decorated hierarchical 1D TiO₂ fiber: A robust and highly efficient co-catalyst for hydrogen evolution reaction. *Appl Surf Sci.* 2020; **521**, 146333.
55. Tonndorf P, et al. Single-photon emitters in GaSe. *2D Materials.* 2017; **4** (2), 021010.
56. Lee YK, Luo Z, Cho SP, Kanatzidis MG, Chung I. Surface Oxide Removal for Polycrystalline SnSe Reveals Near-Single-Crystal Thermoelectric Performance. *Joule.* 2019; **3** (3), 719-31.
57. Lamuta C, Campi D, Pagnotta L, Dasadia A, Cupolillo A, Politano A. Determination of the mechanical properties of SnSe, a novel layered semiconductor. *J Phys Chem Solids.* 2018; **116**, 306-12.
58. Balitskii OA, Savchyn VP, Yukhymchuk VO. Raman investigation of InSe and GaSe single-crystals oxidation. *Semicond Sci Technol.* 2002; **17** (2), L1-L4.
59. Beechem TE, et al. Oxidation of ultrathin GaSe. *Appl Phys Lett.* 2015; **107** (17).
60. Bergeron A, Ibrahim J, Leonelli R, Francoeur S. Oxidation dynamics of ultrathin GaSe probed through Raman spectroscopy. *Appl Phys Lett.* 2017; **110** (24), 241901.
61. Filippo E, Siciliano M, Genga A, Micocci G, Tepore A, Siciliano T. Single crystalline β-Ga₂O₃ nanowires synthesized by thermal oxidation of GaSe layer. *Mater Res Bull.* 2013; **48** (5), 1741-4.
62. Iwakuro H, Tatsuyama C, Ichimura S. XPS and AES studies on the oxidation of layered semiconductor GaSe. *Japanese Journal of Applied Physics.* 1982; **21** (1R), 94.
63. Kowalski BM, Manz N, Bethke D, Shaner EA, Serov A, Kalugin NG. Role of humidity in oxidation of ultrathin GaSe. *Mater Res Express.* 2019; **6** (8).
64. Rahaman M, Rodriguez RD, Monecke M, Lopez-Rivera SA, Zahn DRT. GaSe oxidation in air: From bulk to monolayers. *Semicond Sci Technol.* 2017; **32** (10).
65. Siciliano T, Tepore M, Genga A, Micocci G, Siciliano M, Tepore A. Thermal oxidation of amorphous GaSe thin films. *Vacuum.* 2013; **92**, 65-9.
66. Tovstyuk NK. Thermodynamics of GaSe oxidation in the gas lattice model. *Journal of*

Physical Studies. 2004; **8** (1), 47-54.

67. Tan SM, Chua CK, Sedmidubský D, Sofer ZB, Pumera M. Electrochemistry of layered GaSe and GeS: Applications to ORR, OER and HER. *Physical Chemistry Chemical Physics*. 2016; **18** (3), 1699-711.

68. Ho C, Wu C, Cheng Z. Crystal structure and electronic structure of GaSe_{1-x}S_x series layered solids. *J Cryst Growth*. 2005; **279** (3-4), 321-8.

69. Lee P. *Physics and Chemistry of Materials with Layered Structures, Vol. 4: Optical and Electrical Properties* Reidel. Boston; 1976.

70. Yoshida H, Nakashima S, Mitsuishi A. Phonon Raman spectra of layer compound GaSe. *Phys Status Solidi B*. 1973; **59** (2), 655-66.

71. Popović S, Tonejc A, Gržeta-Plenković B, Čelustka B, Trojko R. Revised and new crystal data for indium selenides. *J Appl Crystallogr*. 1979; **12** (4), 416-20.

72. Pozo-Zamudio D, et al. Photoluminescence and Raman investigation of stability of InSe and GaSe thin films. *arXiv:150605619*. 2015.

73. Andres-Penares D, Cros A, Martínez-Pastor JP, Sánchez-Royo JF. Quantum size confinement in gallium selenide nanosheets: band gap tunability versus stability limitation. *Nanotechnology*. 2017; **28** (17), 175701.

74. Susoma J, Lahtinen J, Kim M, Riikonen J, Lipsanen H. Crystal quality of two-dimensional gallium telluride and gallium selenide using Raman fingerprint. *AIP Advances*. 2017; **7** (1), 015014.

75. Ho P-H, et al. High-Mobility InSe Transistors: The Role of Surface Oxides. *ACS Nano*. 2017; **11** (7), 7362-70.

76. Petroni E, et al. Liquid-Phase Exfoliated Indium–Selenide Flakes and Their Application in Hydrogen Evolution Reaction. *Small*. 2018; **14** (26), 1800749.

77. Kim J, Han SM, Yoo WS. Multiwavelength Raman characterization of silicon stress near through-silicon vias and its inline monitoring applications. *Journal of Micro/ Nanolithography, MEMS, and MOEMS*. 2014; **13**, 011205.

78. Borowicz P. Depth-sensitive Raman investigation of metal-oxide-semiconductor structures: absorption as a tool for variation of exciting light penetration depth. *Journal of Spectroscopy*. 2016; **2016**.

79. Merzlikin SV, Tolkahev NN, Strunskus T, Witte G, Glogowski T, Wöll C, Grünert W. Resolving the depth coordinate in photoelectron spectroscopy—Comparison of excitation energy variation vs. angular-resolved XPS for the analysis of a self-assembled monolayer model system. *Surface science*. 2008; **602** (3), 755-67.

80. Shi L, Zhou Q, Zhao Y, Ouyang Y, Ling C, Li Q, Wang J. Oxidation mechanism and protection strategy of ultrathin Indium Selenide: Insight from Theory. *J Phys Chem Lett*. 2017; **8** (18), 4368-73.

81. Ni Y, Wu H, Huang C, Mao M, Wang Z, Cheng X. Growth and quality of gallium selenide (GaSe) crystals. *Journal of Crystal Growth*. 2013; **381**, 10-4.

82. Zangrando M, Finazzi M, Paolucci G, Comelli G, Diviacco B, Walker R, Cocco D, Parmigiani F. BACH, the beamline for advanced dichroic and scattering experiments at ELETTRA. *Review of Scientific Instruments*. 2001; **72** (2), 1313-9.

83. Ibach H, Mills DL. *Electron Energy Loss Spectroscopy and Surface Vibrations*. San Francisco: Academic Press; 1982.

84. Baer D, Henrich V, Gassman P, Franchy R, Ibach H, Margaritondo G. Introduction to Surface Spectra of Oxides II. *Surf Sci Spectra*. 1998; **5** (3), 159-64.

85. Dhanasingh S, Nallasamy D, Padmanapan S, Padaki V. Cetyltrimethylammonium bromide- and ethylene glycol-assisted preparation of mono-dispersed indium oxide nanoparticles using hydrothermal method. *Chem Pap*. 2014; **68** (8), 1079.

86. Skinner J, Pieniazek P, Gruenbaum S. Vibrational spectroscopy of water at interfaces. *Acc Chem Res*. 2012; **45** (1), 93-100.

87. Márquez F, Segura A, Muñoz V, González G. Surface passivation of gallium selenide by nitrogen implantation. *Surface and Interface Analysis*. 2002; **34** (1), 460-3.
88. Ben Aziza Z, et al. Van der Waals Epitaxy of GaSe/Graphene Heterostructure: Electronic and Interfacial Properties. *ACS Nano*. 2016; **10** (10), 9679-86.
89. Chegwiddden S, Dai Z, Olmstead M, Ohuchi F. Molecular beam epitaxy and interface reactions of layered GaSe growth on sapphire (0001). *J Vac Sci Technol A*. 1998; **16** (4), 2376-80.
90. Huang C, Wang Z, Ni Y, Wu H, Chen S. Experimental and theoretical investigations on the defect and optical properties of S- and Al-doped GaSe crystals. *RSC Adv*. 2017; **7** (38), 23486-93.
91. Epp JM, Dillard J. Effect of ion bombardment on the chemical reactivity of gallium arsenide (100). *Chem Mater*. 1989; **1** (3), 325-30.
92. Ganesan K, Ghosh S, Krishna NG, Ilango S, Kamruddin M, Tyagi A. A comparative study on defect estimation using XPS and Raman spectroscopy in few layer nanographitic structures. *Phys Chem Chem Phys*. 2016; **18** (32), 22160-7.
93. Zatsepin AF, Zatsepin DA, Boukhvalov DW, Kuznetsova YA, Gavrilov NV, Shur VY, Esin AA. Local atomic configurations, energy structure, and optical properties of implantation defects in Gd-doped silica glass: An XPS, PL, and DFT study. *J Alloys Compd*. 2019; **796**, 77-85.
94. Märkl A, von der Emde M, Nowak C, Richter W, Zahn DRT. Investigation of Se capping of epitaxial Ga₂Se₃ layers. *Surface Science*. 1995; **331-333**, 631-5.
95. Navarro-Quezada A, Alamé S, Esser N, Furthmüller J, Bechstedt F, Galazka Z, Skuridina D, Vogt P. Near valence-band electronic properties of semiconducting β -Ga₂O₃(100) single crystals. *Phys Rev B*. 2015; **92** (19), 195306.
96. Wang Y, Li N, Duan P, Sun X, Chu B, He Q. Properties and Photocatalytic Activity of β -Ga₂O₃ Nanorods under Simulated Solar Irradiation. *Journal of Nanomaterials*. 2015; **2015**, 1-5.
97. Huang L, et al. Comparison Study of β -Ga₂O₃ Photodetectors Grown on Sapphire at Different Oxygen Pressures. *IEEE Photonics Journal*. 2017; **9** (4), 1-8.
98. Kong L, Ma J, Luan C, Mi W, Lv Y. Structural and optical properties of heteroepitaxial beta Ga₂O₃ films grown on MgO(100) substrates. *Thin Solid Films*. 2012; **520** (13), 4270-4.
99. Grosvenor AP, Kobe BA, McIntyre NS. Studies of the oxidation of iron by water vapour using X-ray photoelectron spectroscopy and QUASES™. *Surface Science*. 2004; **572** (2), 217-27.
100. Schiros T, et al. Structure and Bonding of the Water-Hydroxyl Mixed Phase on Pt(111). *The Journal of Physical Chemistry C*. 2007; **111** (41), 15003-12.
101. Würz R, et al. In situ X-ray photoelectron spectroscopy study of the oxidation of CuGaSe₂. *Surface Science*. 2005; **580** (1), 80-94.
102. Geller S. Crystal Structure of β -Ga₂O₃. *J Chem Phys*. 1960; **33** (3), 676-84.
103. Surdu-Bob C, Saied S, Sullivan J. An X-ray photoelectron spectroscopy study of the oxides of GaAs. *Appl Surf Sci*. 2001; **183** (1-2), 126-36.
104. Adams IV WT, Vinueza NR, Romanyuk O, Gordeev I, Paskova T, Ivanisevic A. Nanostructured GaOOH modified with reactive yellow, red and blue water-soluble dyes. *AIP Advances*. 2019; **9** (2), 025005.
105. Pearce BL, Berg NG, Rahn MS, Ivanisevic A. In situ and ex situ functionalization of nanostructured gallium oxy-hydroxide with a porphyrin dye. *Scanning*. 2016; **38** (6), 671-83.
106. Tong Y, et al. Case studies on the formation of chalcogenide self-assembled monolayers on surfaces and dissociative processes. *Beilstein J Nanotechnol*. 2016; **7** (1), 263-77.
107. Tong Y, Jiang T, Bendounan A, Nicolas F, Kubsky S, Esaulov VA. Selenium, Benzeneselenol, and Selenophene Interaction with Cu(100). *J Phys Chem C*. 2016; **120** (38), 21486-95.
108. Sun F, Li Y, Wu Z, Liu Y, Tang H, Li X, Yue Z, Zhou L. In situ reactive coating of metallic and selenophilic Ag₂Se on Se/C cathode materials for high performance Li-Se batteries. *RSC Adv*. 2018; **8** (57), 32808-13.

109. Dimitriev Y, Lakov L. The structure of oxide glasses containing SeO₂. *Journal of non-crystalline solids*. 2001; **293**, 410-5.
110. Fan Y, Zhuo Y, Li L. SeO₂ adsorption on CaO surface: DFT and experimental study on the adsorption of multiple SeO₂ molecules. *Appl Surf Sci*. 2017; **420**, 465-71.
111. Zheng Q, Cheng X, Li H. Microwave Synthesis of High Activity FeSe₂/C Catalyst toward Oxygen Reduction Reaction. *Catalysts*. 2015; **5** (3), 1079-91.
112. Li R, Luo Z, Papadimitrakopoulos F. Redox-assisted asymmetric Ostwald ripening of CdSe dots to rods. *Journal of the American Chemical Society*. 2006; **128** (19), 6280-1.
113. Reddy IN, Reddy CV, Cho M, Shim J, Kim D. Structural, optical and XPS study of thermal evaporated In₂O₃ thin films. *Mater Res Express*. 2017; **4** (8), 086406.
114. Greeley J, Jaramillo TF, Bonde J, Chorkendorff I, Nørskov JK. Computational high-throughput screening of electrocatalytic materials for hydrogen evolution. *Nature Materials*. 2006; **5** (11), 909-13.
115. Liu T, Feng Z, Li Q, Yang J, Li C, Dupuis M. Role of Oxygen Vacancies on Oxygen Evolution Reaction Activity: β -Ga₂O₃ as a Case Study. *Chemistry of Materials*. 2018; **30** (21), 7714-26.
116. Jochum W, Penner S, Kramer R, Föttinger K, Ruppel G, Klötzer B. Defect formation and the water-gas shift reaction on β -Ga₂O₃. *J Catal*. 2008; **256** (2), 278-86.
117. Tan SM, Chua CK, Sedmidubský D, Sofer Z, Pumera M. Electrochemistry of layered GaSe and GeS: applications to ORR, OER and HER. *Physical Chemistry Chemical Physics*. 2016; **18** (3), 1699-711.
118. Paolucci V, D'Olimpio G, Kuo C-N, Lue CS, Boukhvalov DW, Cantalini C, Politano A. Self-Assembled SnO₂/SnSe₂ Heterostructures: A Suitable Platform for Ultrasensitive NO₂ and H₂ Sensing. *ACS Appl Mater Interfaces*. 2020; **12** (30), 34362-9.
119. Zhong Y, et al. High-Response Room-Temperature NO₂ Sensor and Ultrafast Humidity Sensor Based on SnO₂ with Rich Oxygen Vacancy. *ACS Appl Mater Interfaces*. 2019; **11** (14), 13441-9.
120. Vorokhta M, et al. Investigation of gas sensing mechanism of SnO₂ based chemiresistor using near ambient pressure XPS. *Surface Science*. 2018; **677**, 284-90.
121. Das S, Jayaraman V. SnO₂: A comprehensive review on structures and gas sensors. *Prog Mater Sci*. 2014; **66**, 112-255.
122. Li G-J, Kawi S. High-surface-area SnO₂: a novel semiconductor-oxide gas sensor. *Mater Lett*. 1998; **34** (1-2), 99-102.
123. Di Giulio M, Micocci G, Serra A, Tepore A, Rella R, Siciliano P. SnO₂ thin films for gas sensor prepared by rf reactive sputtering. *Sensors and Actuators B: Chemical*. 1995; **25** (1-3), 465-8.
124. Li W, et al. Biomimetic synthesis of 3D mesoporous SnO₂ with substantially increased gas-sensing performance at room temperature using a simple one-pot hydrothermal method. *Appl Surf Sci*. 2020; **512**, 145657.
125. Li W, Ding C, Li J, Ren Q, Bai G, Xu J. Sensing mechanism of Sb, S doped SnO₂(110) surface for CO. *Appl Surf Sci*. 2020; **502**, 144140.
126. Ko WC, Kim KM, Kwon YJ, Choi H, Park JK, Jeong YK. ALD-assisted synthesis of V₂O₅ nanoislands on SnO₂ nanowires for improving NO₂ sensing performance. *Appl Surf Sci*. 2020; **509**, 144821.
127. Tombak A, Ocak YS, Bayansal F. Cu/SnO₂ gas sensor fabricated by ultrasonic spray pyrolysis for effective detection of carbon monoxide. *Appl Surf Sci*. 2019; **493**, 1075-82.
128. Han Y, et al. Construction of MoS₂/SnO₂ heterostructures for sensitive NO₂ detection at room temperature. *Appl Surf Sci*. 2019; **493**, 613-9.
129. Barsan N, Weimar U. Understanding the fundamental principles of metal oxide based gas sensors; the example of CO sensing with SnO₂ sensors in the presence of humidity. *Journal of Physics: Condensed Matter*. 2003; **15** (20), R813.

130. Choi K-I, Hübner M, Haensch A, Kim H-J, Weimar U, Barsan N, Lee J-H. Ambivalent effect of Ni loading on gas sensing performance in SnO₂ based gas sensor. *Sensors and Actuators B: Chemical*. 2013; **183**, 401-10.
131. Theillet P-O, Pierron O. Quantifying adsorbed water monolayers on silicon MEMS resonators exposed to humid environments. *Sensors and Actuators A: Physical*. 2011; **171** (2), 375-80.
132. Panchal V, Giusca CE, Lartsev A, Martin NA, Cassidy N, Myers-Ward RL, Gaskill DK, Kazakova O. Atmospheric doping effects in epitaxial graphene: correlation of local and global electrical studies. *2D Materials*. 2016; **3** (1), 015006.
133. Nataf GF, Gryan P, Guennou M, Kreisel J, Martinotti D, Rountree CL, Mathieu C, Barrett N. Low energy electron imaging of domains and domain walls in magnesium-doped lithium niobate. *Sci Rep*. 2016; **6** (1), 33098.
134. Leung T, Kao C, Su W, Feng Y, Chan C. Relationship between surface dipole, work function and charge transfer: Some exceptions to an established rule. *Phys Rev B*. 2003; **68** (19), 195408.
135. Roy T, Tosun M, Hettick M, Ahn GH, Hu C, Javey A. 2D-2D tunneling field-effect transistors using WSe₂/SnSe₂ heterostructures. *Appl Phys Lett*. 2016; **108** (8), 083111.
136. Li F, Gao X, Wang R, Zhang T, Lu G. Study on TiO₂-SnO₂ core-shell heterostructure nanofibers with different work function and its application in gas sensor. *Sensors and Actuators B: Chemical*. 2017; **248**, 812-9.
137. Batzill M, Katsiev K, Burst JM, Losovyj Y, Bergermayer W, Tanaka I, Diebold U. Tuning surface properties of SnO₂(101) by reduction. *J Phys Chem Solids*. 2006; **67** (9), 1923-9.
138. Serna MI, et al. Low-Temperature Deposition of Layered SnSe₂ for Heterojunction Diodes. *Adv Mater Interf*. 2018; **5** (16), 1800128.
139. Zhang Q, et al. Band offset and electron affinity of MBE-grown SnSe₂. *Appl Phys Lett*. 2018; **112** (4), 042108.
140. Bauer E. Surface microscopy with low energy electrons: Springer; 2014.
141. Tanuma S, Powell CJ, Penn DR. Calculations of electron inelastic mean free paths (IMFPS). IV. Evaluation of calculated IMFPS and of the predictive IMFP formula TPP-2 for electron energies between 50 and 2000 eV. *Surface and interface analysis*. 1993; **20** (1), 77-89.
142. Cox DF, Hoflund GB. An electronic and structural interpretation of tin oxide ELS spectra. *Surface Science*. 1985; **151** (1), 202-20.
143. Tannarana M, et al. Humidity Sensor Based on Two-dimensional SnSe₂/MWCNTs Nanohybrid for the Online Monitoring of Human Respiration and Touchless Positioning Interface. *ACS Sustain Chem Eng*. 2020; **8** (33), 12595–602.
144. Pawar M, Kadam S, Late DJ. High-Performance Sensing Behavior Using Electronic Ink of 2D SnSe₂ Nanosheets. *ChemistrySelect*. 2017; **2** (14), 4068-75.
145. Pawbake AS, Date A, Jadhkar SR, Late DJ. Temperature Dependent Raman Spectroscopy and Sensing Behavior of Few Layer SnSe₂ Nanosheets. *ChemistrySelect*. 2016; **1** (16), 5380-7.
146. Henderson MA. The interaction of water with solid surfaces: fundamental aspects revisited. *Surf Sci Rep*. 2002; **46** (1-8), 1-308.
147. Inamdar AN, Som NN, Pratap A, Jha PK. Hydrogen evolution and oxygen evolution reactions of pristine and alkali metal doped SnSe₂ monolayer. *Int J Hydrogen Energy*. 2020; **45** (37), 18657-65.
148. Deng J, Mo Y, Liu J, Guo R, Zhang Y, Xue W, Zhang Y. In vitro study of SnS₂, BiOCl and SnS₂-incorporated BiOCl inorganic nanoparticles used as doxorubicin carrier. *J Nanosci Nanotechnol*. 2016; **16** (6), 5740-5.
149. Wu S, et al. Realizing tremendous electrical transport properties of polycrystalline SnSe₂ by Cl-doped and anisotropy. *Ceram Int*. 2019; **45** (1), 82-9.
150. Nagaraju G, Cha SM, Sekhar SC, Yu JS. Metallic layered polyester fabric enabled nickel

- selenide nanostructures as highly conductive and binderless electrode with superior energy storage performance. *Adv Energy Mater.* 2017; **7** (4), 1601362.
151. Bachvarova-Nedelcheva A, Iordanova R, Kostov KL, Yordanov S, Ganev V. Structure and properties of a non-traditional glass containing TeO₂, SeO₂ and MoO₃. *Optical Materials.* 2012; **34** (11), 1781-7.
152. Al-Hada NM, Kamari HM, Baqer AA, Shaari AH, Saion E. Thermal Calcination-Based Production of SnO₂ Nanopowder: An Analysis of SnO₂ Nanoparticle Characteristics and Antibacterial Activities. *Nanomaterials.* 2018; **8** (4), 250.
153. Zhang W, Li M, Xiao X, Huang X, Jiang Y, Fan X, Chen L. In situ synthesis of ultrasmall SnO₂ quantum dots on nitrogen-doped reduced graphene oxide composite as high performance anode material for lithium-ion batteries. *J Alloys Compd.* 2017; **727**, 1-7.
154. Hoch LB, Wood TE, O'Brien PG, Liao K, Reyes LM, Mims CA, Ozin GA. The Rational Design of a Single-Component Photocatalyst for Gas-Phase CO₂ Reduction Using Both UV and Visible Light. *Advanced Science.* 2014; **1** (1), 1400013.
155. Detweiler ZM, Wulfsberg SM, Frith MG, Bocarsly AB, Bernasek SL. The oxidation and surface speciation of indium and indium oxides exposed to atmospheric oxidants. *Surface Science.* 2016; **648**, 188-95.
156. Nappini S, Matruggio A, Naumenko D, Dal Zilio S, Bondino F, Lazzarino M, Magnano E. Graphene nanobubbles on TiO₂ for in-operando electron spectroscopy of liquid-phase chemistry. *Nanoscale.* 2017; **9** (13), 4456-66.
157. Hong X, Li S, Wang R, Fu J. Hierarchical SnO₂ nanoclusters wrapped functionalized carbonized cotton cloth for symmetrical supercapacitor. *J Alloys Compd.* 2019; **775**, 15-21.
158. Xu H, Ju J, Li W, Zhang J, Wang J, Cao B. Superior triethylamine-sensing properties based on TiO₂/SnO₂ n-n heterojunction nanosheets directly grown on ceramic tubes. *Sens Actuators B Chem.* 2016; **228**, 634-42.

Conclusion

In conclusion, in this thesis issues related to technology transfer of 2D materials beyond graphene were addressed.

Specifically, a solution for the reduction of costs in the state-of-the-art production of GO was identified. Additionally, we demonstrate that Polarclean represents a unique green candidate solvent for large-scale and scalable production of functional inks based on 2D materials, which naturally enables expanding the use of 2D materials in several application fields, such as agri-food and desalination industries, which are expected to take advantage of the unusual properties of 2D materials in terms of both efficiency and selectivity.

Furthermore, newly discovered 2D materials belonging to the class of metal chalcogenides (PdTe_2 , NiTe_2 , GaSe , SnSe_2) were introduced in the industrial world, by engineering prototypes of catalytic devices, gas sensors and IR/THz imaging systems based on these innovative materials, with competitive performances with the state-of-the-art systems since their first implementation.

Specifically, for bulk NiTe_2 and PdTe_2 we demonstrate that they are ambient-stable materials with diverse applications. These materials are also stable in air, except the formation of a sub-nanometric TeO_2 skin in surfaces exposed to air. Their surfaces are inert toward H_2O and CO , enabling the possibility to fabricate CO -tolerant electrodes for electrocatalysis that would be stable in an aqueous environment. Therefore, the growth of high-quality single crystals with minimized Te vacancies is crucial to favor the technological exploitation of this novel class of transition-metal dichalcogenide hosting type-II Dirac fermions. It has also been shown that undefected PdTe_2 is thermally stable in the temperature range usually employed for most applications (even above 500 K). Conversely, surface TeO_2 phases are thermally unstable, due to temperature-induced reduction, which also implies changes in the electronic properties.

As mentioned above, TMDs can also host topologically protected electronic states. As an example, MoTe₂ is a type-II Weyl semimetal, while PtTe₂ and PdTe₂ are type-II Dirac semimetals. Their Ni-based counterpart, NiTe₂, has also been predicted to be a type-II Dirac semimetal. Notably, the abundance on Earth of Ni compared to Pt and Pd makes NiTe₂ more economic and, correspondingly, more suitable than PtTe₂ and PdTe₂ for large-scale technological applications.

For GaSe we determine that the oxidation into Ga₂O₃, promoted by exfoliation in nanosheets or by the presence of defects in sub-stoichiometric crystals, plays a key role in the recently reported improved performance of electrochemical and photocatalytic reactions upon exfoliation of GaSe in atomically thin layers. Therefore, our results elucidate the role of surface oxides in electrocatalysis and photocatalysis based on nanosheets of III-VI layered semiconductors. These findings pave the way for a novel generation of efficient and cost-effective (photo-) electrocatalysts, based on self-assembled heterostructures formed by taking advantage on the natural interaction of sub-stoichiometric van der Waals semiconductors with air. Furthermore, we expect that these concepts could be extended to any other process ruled by surface chemical reactions, such as gas sensing and adsorption-assisted distillation processes.

Finally, for SnSe₂ we studied the modification of surface properties upon exposure to humid environment. The oxidation process has a direct effect on the work function, which is increased by +0.4 eV. Though the SnSe₂ surface is inert to water at room temperature, upon surface oxidation the SnO₂/SnSe₂ interface shows a remarkable sensitivity to humidity. These results prove the significant influence of humid environments on the electrical response of the SnO₂/SnSe₂ heterostructure. The stability over six months of the SnO₂/SnSe₂ heterostructure was addressed, congruently with the formation of a passivated sub nanometric skin of SnO₂, which remains stable in air. Moreover, the self-assembled heterostructure enabling ultra-sensitive gas sensing without the need of encapsulation. Our findings also imply that recent reports on humidity sensing with SnSe₂ should be reinterpreted, considering the pivotal role of the oxide skin in the interaction with water molecules.

Appendix

A. Calculation of the density of defects

Table A.1 report a detailed comparison in terms of I(D)/I(G) ratio and density of defects n_D for graphene obtained with LPE using Polarclean and other solvents: NMP ^[1, 2] and cyrene ^[1]. Precisely, the estimation of the density of defects, according to the method presented in Ref. ^[3], also consider the laser wavelength λ_L used for Raman measurements, following:

$$n_D \text{ (cm}^{-2}\text{)} = \frac{(1.8 \pm 0.5) \times 10^{22}}{\lambda_L^4} \left(\frac{I_D}{I_G} \right)$$

Table A.1: Comparison of I(D)/I(G) ratios and density of defects, calculated from raw data of Raman spectra of Figure 1.8. For I(D)/I(G) of NMP and cyrene, we report the value that we estimate from the analysis of raw data, together with the declared value in the related literature papers.

Solvent used for LPE	Laser Wavelength [nm]	I(D)/I(G) ratio	Density of defects [defects/cm ⁻²]
Polarclean ^[This Work]	633	0.07 ± 0.01	(8 ± 2) · 10 ⁹
NMP ^[2]	633	0.52 ± 0.01 (~ 0.4)	(6 ± 2) · 10 ¹⁰
NMP ^[1]	514	0.22 ± 0.08 (0.29 ± 0.08)	(6 ± 2) · 10 ¹⁰
Cyrene ^[1]	514	0.21 ± 0.06 (0.20 ± 0.06)	(5 ± 2) · 10 ¹⁰

B. X-Ray Diffraction (XRD)

X-ray diffraction is the most widely used powerful technique to identify the crystal structure and the atomic array of materials. It is based on constructive interference of monochromatic X-rays and a crystalline sample. The interaction of the incident X rays with the sample produces constructive interference when conditions satisfy Bragg's Law

$$n\lambda = 2d \sin\theta$$

This law relates the wavelength of electromagnetic radiation to the diffraction angle and the lattice spacing in a crystalline sample.

C. Calculation of phonon modes

Phonon dispersion calculations were performed within the “frozen-phonon” method using the projector augmented wave (PAW) pseudopotentials and a plane basis set as implemented in VASP [4-6]. The cut-off for the plane wave basis is set to 500eV and a Γ -centered 12x12x8 k-grid was used for the Brillouin zone integration [7].

The exchange correlation part of the potential was treated within the local density approximation (LDA) [8]. All the structures were properly relaxed until the force on each atom become vanishingly small.

Below, we have tabulated the phonon frequencies of bulk NiTe₂ in cm⁻¹ at the Γ -point, indicating their infrared or Raman activity based on our DFT calculations. The modes corresponding to ~ 87 cm⁻¹ and ~ 150 cm⁻¹ are Raman active.

Table A 2: Phonon frequencies of bulk NiTe₂ at the Γ -point.

Branch number	Frequency [cm ⁻¹]	Symmetry	Infrared (I) / Raman (R) activity
---------------	-------------------------------	----------	-----------------------------------

1-2	0.00	E_u	-
3	0.00	A_{2u}	-
4-5	87.76	E_g	R
6	150.30	A_{1g}	R
7	211.58	A_{2u}	I
8-9	227.66	E_u	I

Thus, in NiTe₂ there are 9 phonon modes, three acoustic and 6 optical. Only E_g and A_{1g} are Raman active. In Figure A1 we show a sketch of the displacements of the atoms, corresponding to these phonon modes.

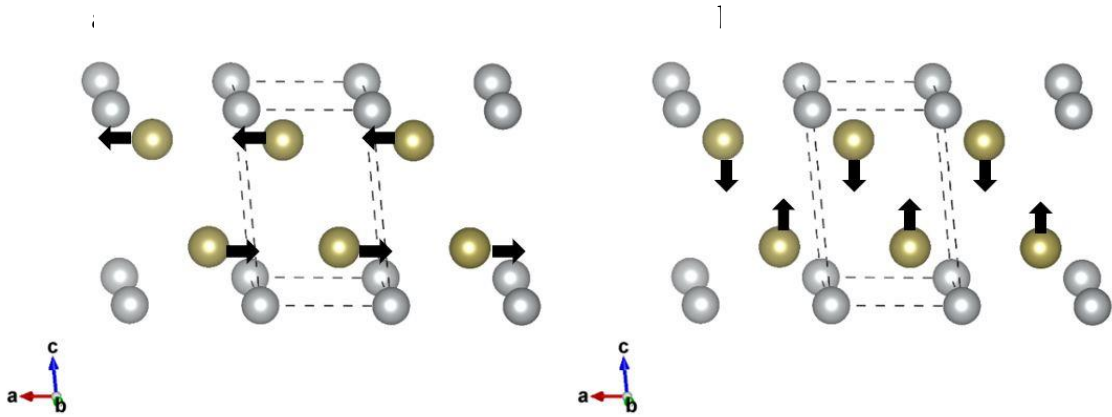


Figure A 1: Schematic representation of the (a) E_g and (b) A_{1g} modes. Grey and golden spheres indicate Ni and Te atoms, respectively.

D. Survey XPS spectrum of the as-cleaved samples of NiTe₂ and PdTe₂

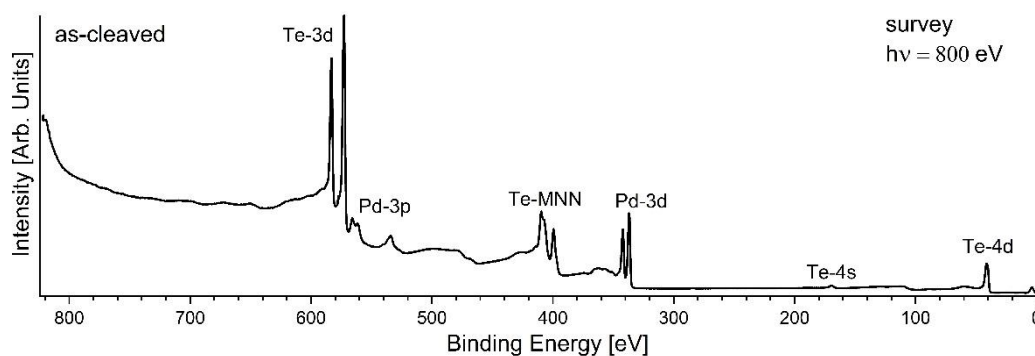


Figure A.2: Survey XPS spectrum of as-cleaved PdTe₂. Photon energy is 800 eV.

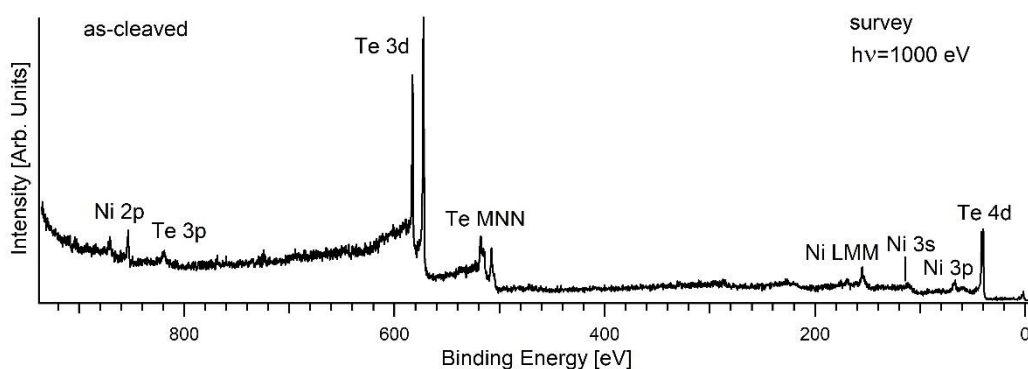


Figure A.3: Survey XPS spectrum of as-cleaved NiTe₂. Photon energy is 1000 eV.

E. Determination of the thickness of the oxide skin

Assuming an ideal situation in which a uniform layer of oxide is formed, we estimated the thickness of the surface oxide phase, d (Å) from the core-level spectrum. The intensity ratio between oxidized species (I_o , area of oxide

component in the core level spectra) and pristine surfaces (I_m , area of the pristine material component), using the following equation ^[9, 10]:

$$d (\text{\AA}) = \lambda_o \sin\theta \ln \left(\frac{N_m \lambda_m I_o}{N_o \lambda_o I_m} + 1 \right)$$

where λ_o and λ_m are the effective attenuation lengths (EALs) of oxide and pristine material, respectively.

The peak intensities, I_o and I_m , were obtained from XPS data analysis of core level, while the EAL values at the experimental electron energy of were calculated with QUASES-IMFP-TPP2M Ver. 3.0, based on the Tanuma, Powell, Penn TPP-2M formula ^[11]. N_m and N_o are the volume densities of material atoms. θ is the angle between the sample surface and the axis of the electron analyzer, as depicted in Figure A.4.

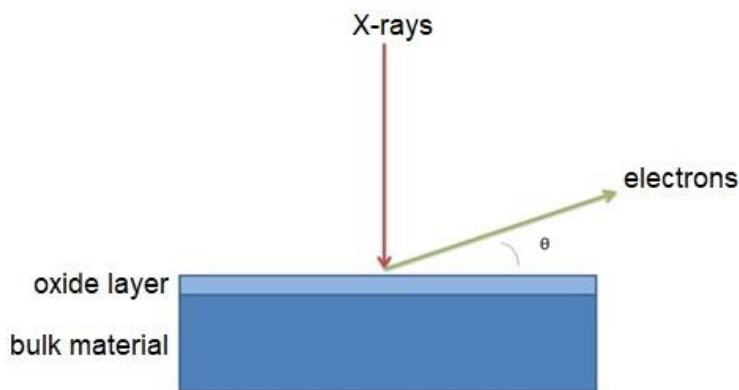


Figure A.4: Geometry used for XPS measurements.

F. Survey XPS spectrum of the as-cleaved samples of GaSe and InSe

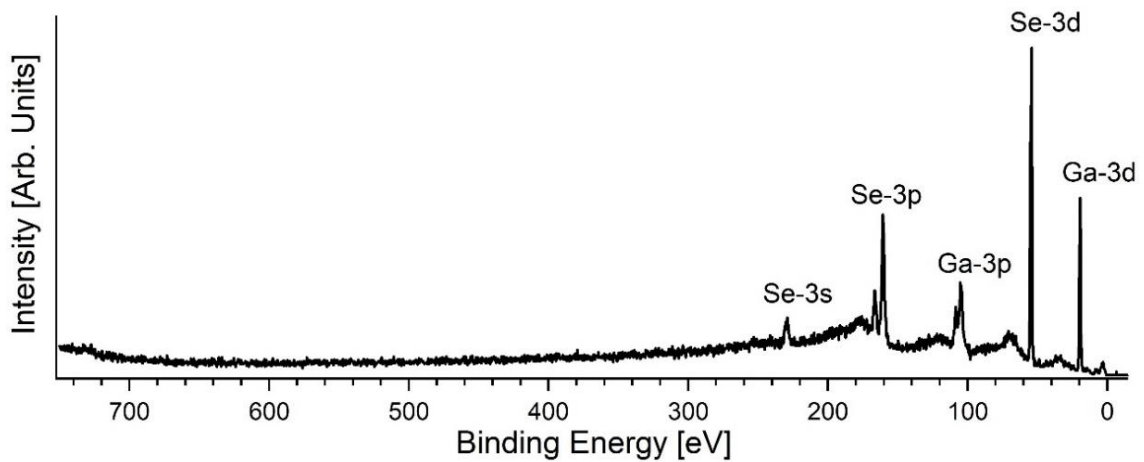


Figure A.5: Survey XPS spectrum of as-cleaved sample of GaSe measured with a photon energy of 830 eV, acquired at BACH beamline Elettra synchrotron.

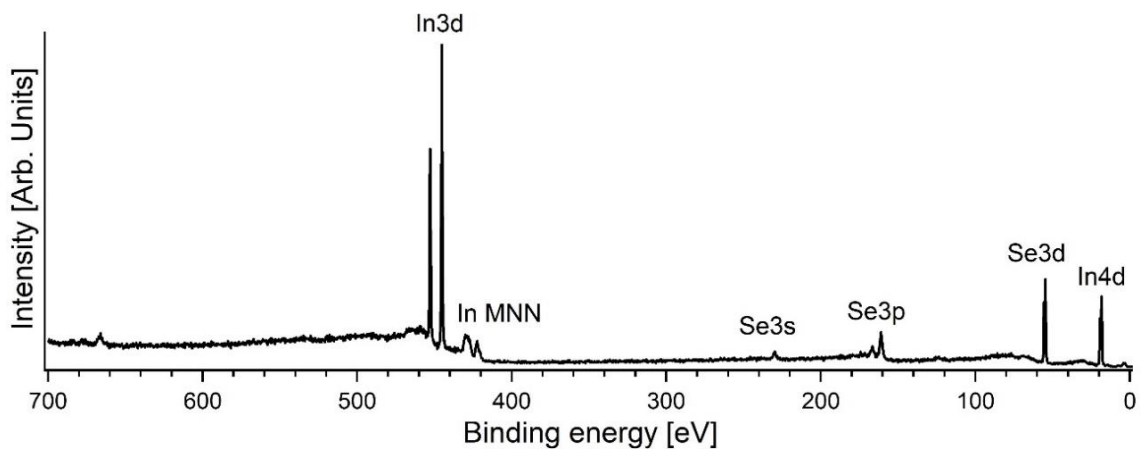


Figure A.6: Survey XPS spectrum of as-cleaved sample of InSe measured with a photon energy of 830 eV, acquired at BACH beamline Elettra synchrotron.

G. Survey XPS spectrum of the as-cleaved sample of SnSe₂

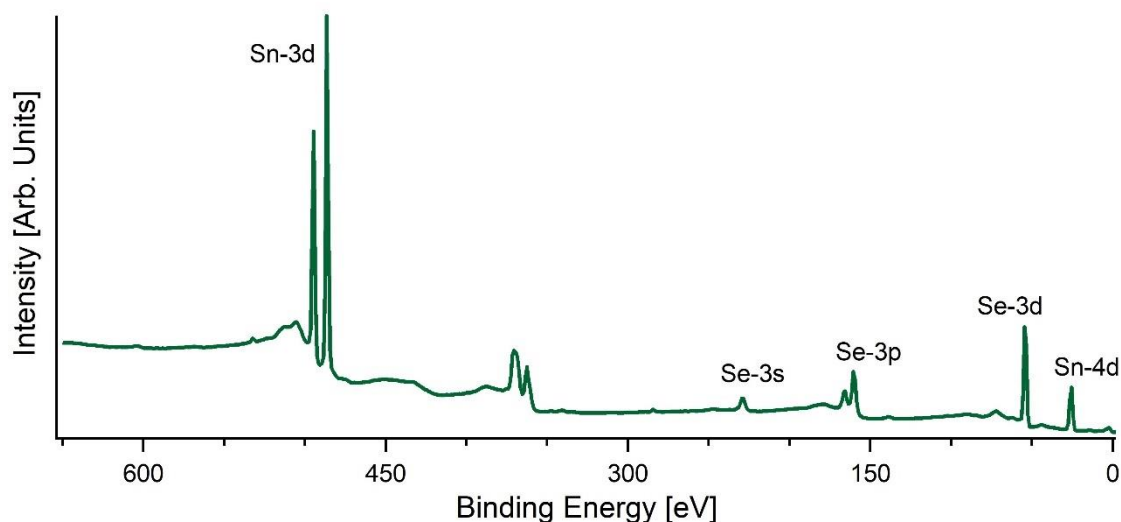


Figure A.7: Survey XPS spectrum of SnSe₂ single crystal with a photon energy of 800 eV, acquired at APE-HE beamline Elettra synchrotron.

References

1. Salavagione HJ, Sherwood J, Budarin V, Ellis G, Clark J, Shuttleworth P. Identification of high performance solvents for the sustainable processing of graphene. *Green Chem.* 2017; **19** (11), 2550-60.
2. Khan U, Porwal H, O'Neill A, Nawaz K, May P, Coleman JN. Solvent-exfoliated graphene at extremely high concentration. *Langmuir.* 2011; **27** (15), 9077-82.
3. Cançado LG, et al. Quantifying Defects in Graphene via Raman Spectroscopy at Different Excitation Energies. *Nano Letters.* 2011; **11** (8), 3190-6.
4. Kresse G, Furthmüller J. Efficient iterative schemes for ab initio total-energy calculations using a plane-wave basis set. *Phys Rev B.* 1996; **54** (16), 11169-86.
5. Kresse G, Joubert D. From ultrasoft pseudopotentials to the projector augmented-wave method. *Phys Rev B.* 1999; **59** (3), 1758.
6. Togo A, Tanaka I. First principles phonon calculations in materials science. *Scr Mater.* 2015; **108**, 1-5.
7. Blöchl PE, Jepsen O, Andersen OK. Improved tetrahedron method for Brillouin-zone integrations. *Phys Rev B.* 1994; **49** (23), 16223-33.
8. Kohn W, Sham LJ. Self-Consistent Equations Including Exchange and Correlation Effects. *Phys Rev.* 1965; **140** (4A), A1133-A8.
9. Alexander MR, Thompson GE, Zhou X, Beamson G, Fairley N. Quantification of oxide film thickness at the surface of aluminium using XPS. *Surface and Interface Analysis.* 2002; **34** (1),

485-9.

10. Sciortino L, Cicero UL, Magnano E, Piš I, Barbera M. Surface investigation and aluminum oxide estimation on test filters for the ATHENA X-IFU and WFI detectors: SPIE; 2016.

11. Tanuma S, Powell CJ, Penn DR. Calculations of electron inelastic mean free paths. V. Data for 14 organic compounds over the 50–2000 eV range. *Surface and interface analysis*. 1994; **21** (3), 165-76.

La borsa di dottorato è stata cofinanziata con risorse del Programma Operativo Nazionale 2014-2020 (CCI2014IT16M2OP005), Fondo Sociale Europeo, Azione I.1 “Dottorati Innovativi con caratterizzazione industriale”



UNIONE EUROPEA
Fondo Sociale Europeo



*Ministero dell'Istruzione,
dell'Università e della Ricerca*

